Sun, Xiao (2024) *Novel photonic integrated circuits devices based on AlGaInAs/InP*. PhD thesis.

https://theses.gla.ac.uk/84180/

# Novel Photonic Integrated Circuits Devices Based on AlGaInAs/InP

**Xiao Sun**

**2023**

A thesis submitted for the degree of

Doctor of Philosophy (Ph.D.)

Electronics and Nanoscale Engineering,

James watt school of engineering

# Declaration of Authorship

I, **Xiao Sun**, declare that this thesis titled **"Novel Photonic Integrated Circuits Devices Based on AlGaInAs/InP"** and the contributions presented in it are my own. I confirm that:

This work was done wholly or mainly while in candidature for a research degree at this University.

Where any part of this thesis has previously been submitted for a degree or any other qualification at this University or any other institution, this has been clearly stated.

Where I have consulted the published work of others, this is always clearly attributed.

Where I have quoted from the work of others, the source is always given. With the exception of such quotations, this thesis is entirely my own work. I have acknowledged all main sources of help.

Where the thesis is based on work done by myself jointly with others, I have made clear exactly what was done by others and what I have contributed myself.

Signed: Xiao Sun

Date: Oct 13, 2023

# Comment

# List of Figures

# Acronyms

| Symbol | Description | Symbol | Description |
|---|---|---|---|
| PIC | Photonic integrated circuit | QWI | Quantum-well intermixing |
| PMC | Polarization mode converter | MMI | Multimode interference |
| PCE | Polarization conversion efficiency | MZM | Mach-Zehnder modulators |
| ICP | Inductively coupled plasma | FP | Fabry-pero |
| DPS | Differential phase shifters | DBR | Distributed Bragg reflector |
| EML | Electroabsorption modulated laser | IEL | Identical epitaxial layer |
| MQW | Multiple quantum well | EBL | Electro-beam lithography |
| LD | Laser diode | HSQ | Hydrogen silsesquioxane |
| DSP | Digital signal processing | PMMA | Polymethyl methacrylate |
| SW | Symmetry waveguide | ACWRC | average current-induced wavelength redshift coefficient |
| AW | Asymmetry waveguide | GPIB | general-purpose interface bus |
| SOP | State of polarization | TEC | thermoelectric cooler |
| SWG | Sidewall grating | SV | Stokes vector |
| DFB | Distributed feedback Bragg | HF | Hydrofluoric |
| FEM | Finite-Element Method | SEM | Scanning electron microscope |
| SMSR | Side mode suppression ratios | RBW | Resolution bandwidth |
| MOVPE | Metalorganic vapor-phase epitaxy | WDM | Wavelength Division Multiplexing |
| ER | Extinction ratio | DWDM | Dense Wavelength Division Multiplexing |
| IPA | Isopropanol | SLM | single longitudinal mode |
| RTA | Rapid Thermal Annealing | OSA | Optical spectrum analyzer |
| PEC | proximity effect correction | E/O | Electrical-to-optical |
| PECVD | Plasma-Enhanced Chemical Vapour Deposition | PL | Photoluminescence |
| TMM | Transfer matrix method | SBG | Sampled Bragg gratings |
| QCSE | Quantum-confined Stark effect | FRL | Far-field reduction layer |
| MIBK | Mixture of methyl isobutyl ketone |  |  |

# Abstract

AlGaInAs/InP material system's unique properties, such as a larger conduction band discontinuity ($\Delta E_c = 0.72\Delta E_g$) and a smaller valance band discontinuity have made it an attractive choice for photonic integrated circuits (PIC) devices. In this thesis, several novel PIC devices have been designed, fabricated, and characterized based on conventional 1550 nm AlGaInAs/InP multiple quantum well (MQW) laser diode (LD) epilayer structure.

The first device is the polarization mode converter (PMC), which is monolithically integrated with a sidewall grating (SWG) distributed feedback Bragg (DFB) laser. The study highlights two kinds of PMC with different waveguide structures: the half-ridge waveguide and the stepped-height ridge waveguide. Based on the simulation results, it was observed that the half-ridge waveguide achieved a polarization conversion efficiency (PCE) of approximately 90% with a half-beat length of 1200 μm. In contrast, the stepped-height ridge waveguide demonstrated a significantly superior PCE of 97.3 % with a half-beat length of 490 μm. Subsequently, the stepped-height ridge waveguide PMCs integrated with the SWG DFB laser were fabricated utilizing E-beam lithography and inductively coupled plasma (ICP) etching techniques. The achieved results indicated a PCE of 98.4% over a broad range of DFB injection currents at 1555 nm wavelength and a PCE > 90% over the wavelength range of 1543 to 1568 nm. The second device is the PMC integrated with SWG DFB laser and differential phase shifter (DPS)(100-μm-long) to achieve active polarization control, and a nearly 60° rotation of the Stokes vector on the Poincaré sphere was obtained with a range of DPS bias voltage from 0 V to –3.0 V, which exhibited excellent agreement with the simulation result. 360° rotation of the Stokes vector on the Poincaré sphere is expected by using a 900- μm-long quantum well intermixed (100 nm blueshift) DPS.

The third device presented is the eight-channel electroabsorption modulated lasers (EMLs) array based on sidewall four phase-shifted sampled Bragg gratings(4PS-SBG), a C-band eight-channel EML array is presented, with a channel spacing of 0.8 nm. The use of 4PS-SBG sidewall DFB lasers can preserve high coupling coefficients (0.9 times of continuous uniform gratings) and maintain precise channel spacing control, significantly simplifying the EML device fabrication process, requiring only one metalorganic vapor-phase epitaxy (MOVPE) step and one III-V material etch. The DFB lasers exhibit side mode suppression ratios (SMSRs) greater than 42 dB, while the integrated EAM achieves a 20 dB extinction ratio (ER), and the 3-dB modulation bandwidth is more than 20 GHz.

By the way, I have designed, optimized, and fabricated two innovative InP-based devices: the 1D and 2D topological photonic crystal lasers. However, further optimization of the fabrication processes is required to ensure the functionality of these two devices.

# Acknowledgements

I am incredibly grateful to have had the opportunity to complete this doctoral thesis, and I would like to express my heartfelt thanks to all those who have supported me throughout this journey.

First and foremost, I extend my deepest appreciation to my advisor, Prof. Lianping Hou, for providing me with his invaluable guidance, encouragement, and support. His unwavering faith in my abilities has been a constant source of motivation and inspiration, and I am grateful for the knowledge, skills, and research opportunities in the device design, fabrication, and measurement he has provided me with. I would like to thank my second supervisor, Prof. John Marsh, for invaluable feedback, insights, and critiques during my research. His expertise and constructive feedback have been instrumental in shaping my research and helping me to produce a thesis of the highest quality.

I would like to thank JWNC for providing me with access to the state-of-the-art research facilities and resources that were necessary for me to conduct my research. I am especially grateful to the staff and technicians for their assistance with experimental setup and troubleshooting.

I would like to acknowledge my colleagues and friends, who have provided me with their unwavering support, encouragement, and camaraderie throughout my graduate studies. I would like to thank Dr. Shengwei Ye for his patience on teaching me familiar with the fabrication process. I would like to thank Huihua Cheng for sharing his experience of Ebeam resist usage. I would like to thank Rachal love who helped me a lot in ICP dry etch recipe optimization.

Finally, I would like to express my sincere gratitude to my family, especially my parents, for their unconditional love, support, and encouragement throughout my PhD life. even if thousands of miles away from them.

# List of Publishment

## Journal paper

[1] **X. Sun,** S. Liang, W. Cheng, S. Ye, Y. Sun, Y. Huang, R. Zhang, J. Xiong, X. Liu, J. H. Marsh, L. Hou, “Regrowth-free AlGaInAs MQW polarization controller integrated with sidewall grating DFB laser,” Photonics Research, vol.11, no.4, pp.622-630, 2023 (Editors’ Pick).

[2] **X. Sun,** W. Cheng, S. Liang, S. Ye, Y. Huang, R. Zhang, B. Qiu, J. Xiong, X. Liu, J. H. Marsh, L. Hou “Stepped-height ridge waveguide MQW polarization mode converter monolithically integrated with sidewall grating DFB laser,” Optics Letters, vol.48, no.2 pp.359-362, 2023.

[3] B. Yuan, Y. Fan, S. Ye, Y. Zhang, Y. Sun, **X. Sun**, W. Cheng, S. Liang, Y. Huang, R. Zhang, J. Wang, J. H. Marsh, L. Hou, “Dual-wavelength DFB Laser Array Based on Sidewall Grating and Lateral Modulation of the Grating Coupling Coefficient,” Journal of Lightwave Technology, vol.41, no.9, pp.2775-2784, 2023.

[4] W. Cheng, **X. Sun**, S. Ye, B. Yuan, Y. Sun, J. H. Marsh, L. Hou, “Sidewall grating slot waveguide microring resonator biochemical sensor,” Optics Letters, vol.48, no.19, pp.5113-5116, 2023.

[5] S. Ye, **X. Sun**, B. Yuan, P. Read, P. Maidment, Y. Huang, R. Zhang, S. Watson, A. Kelly, J. H. Marsh, and L. Hou “1.55-μm Sidewall Grating DFB Lasers Integrated with a Waveguide Crossing for an Optical Beam Forming Network,” IEEE Photon. Technol. Lett., vol.35, no.14, pp.785-788, 2023.

[6] **X. Sun,** W. Cheng, Y. Sun, S. Ye, A. Al-Moathin, Y. Huang, R. Zhang, S. Liang, B. Qiu, J. Xiong, X. Liu, J. H. Marsh, L. Hou, “Simulation of an AlGaInAs/InP electro-absorption modulator monolithically integrated with sidewall grating distributed feedback laser by quantum well intermixing,” Photonics, vol. 9, pp.564,2022.

[7] **X. Sun**, S. Ye, W. Cheng, S. Liang, Y. Huang, B. Qiu, Z. Li, J. Xiong, X. Liu, J. H. Marsh, L. Hou, “Monolithically Integrated AlGaInAs MQW Polarization Mode

Converter using a Stepped Height Ridge Waveguide," IEEE Photonics Journal, vol. 14, no. 3, June 2022.

[8] Y. Sun, B. Yuan, **X. Sun**, S. Liang, Y. Huang, R. Zhang, S. Ye, Y. Fan, W. Cheng, J. H. Marsh, L. Hou, "DFB laser array based on four phase-shifted sampled Bragg grating with precise wavelength control," Opt. Lett., vol.47, no.23 pp.6237-6240, 2022.

[9] **X. Sun,** S. Ye, B. Qiu, J. Xiong, X. Liu, J. Marsh, and L. Hou, "Design and Optimization of 1.55 μm AlGaInAs MQW Polarization Mode Controllers," Photonics, vol. 8, no. 10, pp. 422, 2021.

[10]X. Jin, H. Zhang, B. Ni, W. Liu, L. Hou, J. H. Marsh, S. Ye, **X. Sun**, X. Li, S. Li, L. Dong, J. Hou, M. Sun, B. Xu, J. Xiong, and X. Liu, "Label-free sensing below the sub-diffraction limit of virus-like particles by wide-field photon state parametric imaging of a gold nanodot array", DOI: 10.1039/D1NA00603G, Nanoscale Adv., 2021.

**Conference paper**

[11]**X. Sun**, Y. Sun, W. Cheng, S. Ye, S. Liang, R. Zhang, B. Qiu, J. Xiong, F. Xue, J. H. Marsh and L. Hou," Eight-channel EML array based on four phase-shifted sampled Bragg gratings," in *2023 Conference on Lasers and Electro-Optics (CLEO 2*023).

[12]**X. Sun**, W. Cheng, S. Liang, S. Ye, Y, Huang, Y. Sun, R. Zhang, J. Xiong, F. Xue, J. H. Marsh and L. Hou," Monolithic MQW Polarization Mode Controller Integrated with Sidewall Grating DFB Laser," in *2023 Conference on Lasers and Electro-Optics (CLEO* 2023).

[13]Cheng, W., **Sun, X**., Ye, S., Yuan, B., Liu, X., Marsh, J. H. and Hou, L. " Inner-Wall Grating Double Slot Microring Resonator for High Sensitivity and Large Measurement Range Label-Free Biochemical Sensing". in *2023 Conference on Lasers and Electro-Optics (CLEO 2*023).

[14]**X. Sun**, S. Ye, J. H. Marsh, W. Cheng, Y. Sun, and L. Hou, "AlGaInAs/InP EML with Sidewall Grating Distributed Feedback Laser and Quantum Well Intermixing Technology," in 2022 *IEEE Photonics Conference (IPC)*(IEEE2022), pp. 1-2.

[15] S. Ye, **X. Sun**, P. Read, A. Kelly, L. Hou, and J. H. Marsh, "Asymmetric Twin-Waveguide 1.55-µm DFB Lasers for an Optical Beam Forming Network," in 2022 *IEEE Photonics Conference (IPC)*(IEEE2022), pp. 1-2.

[16] Y. Sun, B. Yuan, J. H. Marsh, **X. Sun**, Y. Fan, and L. Hou, "DFB Laser Array Based on Four Phase-Shifted Sampled Bragg Gratings," in 2022 *IEEE Photonics Conference (IPC)*(IEEE2022), pp. 1-2.

[17] W. Cheng, S. Ye, **X. Sun**, B. Yuan, J. H. Marsh, and L. Hou, "Double Slot Micro Ring Resonators with Inner Wall Angular Gratings as Ultra Highly Sensitive Biochemical Sensors," in 2022 *IEEE Photonics Conference (IPC)*(IEEE2022), pp. 1-2.

[18] **X. Sun**, S. Ye, J. Seddon, C. C. Renaud, L. Hou, and J. H. Marsh, "Modeling and Measurement of a HSQ Passivated UTC-PD with a 68.9 GHz Bandwidth," in 2021 *IEEE Photonics Conference* (*IPC*)(IEEE2021), pp. 1-2.

# Chapter 1 Introduction

## 1.1 InP-based Photonic Integration

The development opportunities for optical communication technology have emerged with the growing demand for communication bandwidth in modern society. While optical communication technology holds an absolute advantage in long-distance communication, the lack of popularity of optical communication devices at the user end makes it crucial to enhance device integration and reduce costs. Optical devices form the foundation and core of optical communication systems, representing a country's level of proficiency and capability in the field of optical communication technology.

Photonics Integrated Circuits (PICs) encompass the technology that seamlessly integrates multiple optical devices. Contrasted with conventional discrete components, PICs deliver notable advantages in size, energy efficiency, cost-effectiveness, and reliability. They signify the prevailing trajectory for advancing optical device technology into the future.

The novel Photonic Integrated Circuits (PICs) of alloys of III-V quaternary material system (AlGaInAs/InP or InGaAsP/InP) currently enable the generation, manipulation, and detection of optical signals. This has dictated the wavelength range of interest to the near-infrared region, where the bandgap of InGaAsP/ AlGaInAs can be adjusted, it can act as a transparent, absorbing, or light-generating material, while maintaining lattice matching with InP [1]. The components in PICs, depending on the different material properties, can be defined into two domains: passive components, in which the material has a much larger bandgap than the propagating photon energy. Such as optical waveguides, multimode interference (MMI) couplers [2, 3], AWG multiplexers [4], Mach-Zehnder modulators (MZMs) [5, 6], as shown in Fig.1.1.1. Active components, using a material with a bandgap that is equal to or smaller than the energy of the propagating photons, such as semiconductor lasers including the Fabry-Perot (FP) laser, distributed feedback (DFB) [7] and distributed Bragg reflector (DBR) [8] semiconductor lasers. To enhance the electro-optical conversion efficiency, the quantum wells (QWs) have been employed in the fabrication of semiconductor lasers [9]. These QWs are created within semiconductors by placing a material layer between two layers of a material with a wider bandgap, i.e., quantum barrier (QB). This arrangement generates a potential well that can only support discrete energy values. Electrons in semiconductors tend to cluster in the lowest energy levels, improving the efficiency of electro-optical energy conversion.

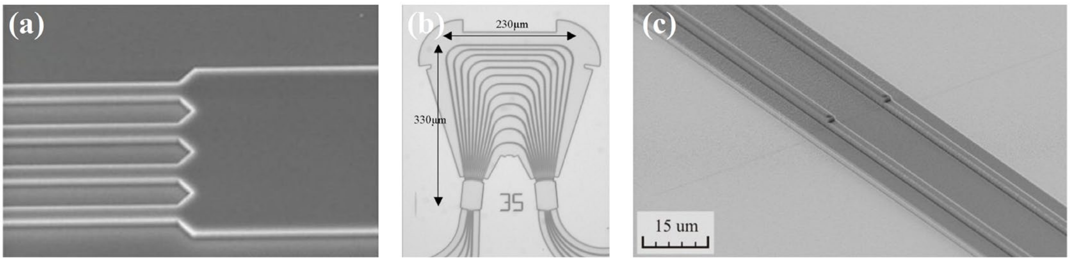

**Figure 1.1.1** Several passive InP-based PIC components. (a) MMI couplers [3], (b) AWG multiplexers [4], (c) MZM [6].

To integrate the passive components with the active source, several active/passive integration scheme techniques have been proposed based on the InP platform shown in Fig 1.1.2: first is the secondary epitaxy regrowth technique such as offset quantum-well waveguides [10], butt-joint regrowth [11], selective area regrowth [12]. As the name suggests, those techniques require multiple rounds of metalorganic vapor-phase epitaxy (MOVPE) growth for the passive material to achieve compatibility with the active area. This approach allows for independent optimization of the performance of passive and active components, without needing to consider the compatibility of different epitaxial layers. However, a significant drawback of this technique is the necessity for a flawless joint interface to minimize scattering loss and enhance coupling efficiency. Additionally, the need for extra epitaxy growth can increase the overall cost of device fabrication. Other techniques without secondary epitaxy regrowth are identical active layer (IEL) and quantum-well intermixing (QWI). IEL means the passive device shares the same epitaxy structure as the active device, which is its greatest advantage and the greatest challenge either. QWI is a technique that selectively tunes the bandgap of the quantum well across a wafer post-growth. After intermixing, the MQW structure has similar characteristics to those of a bulk layer, and its material anisotropy disappears [15]. The QWI involves a growth post-processing method comprising three main steps. Firstly, a large number of point defects are generated on the surface layer above the MQW layer. Secondly, under specific conditions, such as Rapid Thermal Annealing (RTA), the point defects move towards the quantum well region as shown in Fig 1.1.3. Lastly, the point defects cause intermixing of the component atoms of the quantum well/barrier material at the interface, resulting in a change in the material components and band gap wavelength.

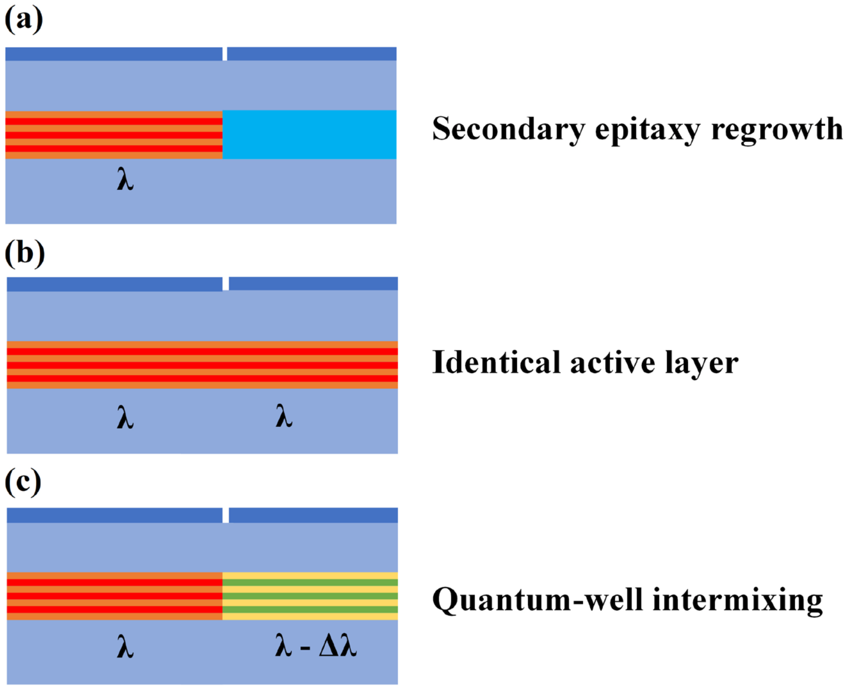

**Figure 1.1.2** Several InP-based active/passive integration approaches (a) secondary epitaxy regrowth, (b) identical active layer, (c) quantum-well intermixing.

There are various approaches to achieve QWI based on different methods for generating point defects. These include impurity-free vacancy diffusion (IFVD) [13], photo-absorption induced intermixing (PAID) [14], ion implantation-induced disordering (IIID) [15], and low-temperature growth induced intermixing in InP [16]. To define different regions of the PIC device, a protective technique is usually employed to create a certain concentration of point defects in the selected region on the epitaxial wafer, while other areas have no point defects. After the RTA process, which promotes point defect diffusion and induces intermixing between QW and QB, bulk-like materials with blueshift bandgap wavelengths are formed in designated regions. The main advantage of QWI technology is that it uses traditional planar epitaxial growth technology and does not require additional growth processes. However, due to the lateral movement of point defects during their generation and diffusion, the composition transition between different materials is not steep, and there is a composition transition region of 2-3 μm, which usually has little effect on the performance of the integrated photonics device.

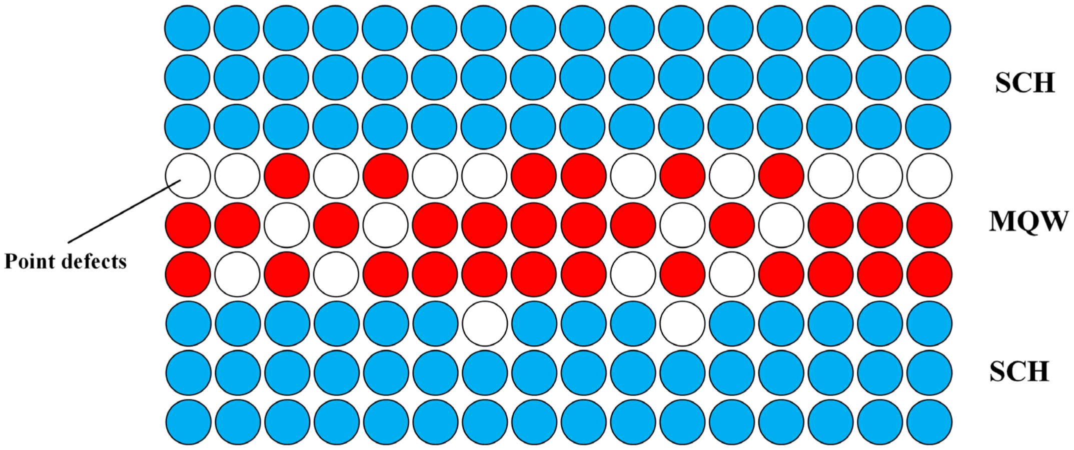

**Figure 1.1.3** Defect diffusions during RTA in a QWI process.

Within the InP platform, a plethora of PIC devices cater to optical communication needs. This section provides an overview of two key photonics devices: semiconductor lasers and polarization controllers.

## 1.1.2 Semiconductor laser source

Figure 1.1.4 illustrates the relationship between bandgap energy and lattice constant in several commonly utilized III-V alloys [17]. This diagram covers a broad range of wavelengths, from red to far infra-red, approximately 0.63-10 μm. It can be found that materials and alloys derived from InP are viable options for use in telecom wavelengths spanning 1.2 to 1.6 μm, which cover the total C-band (1530-1565 nm). Compared with InGaAsP, AlGaInAs AlGaInAs material exhibits a larger conduction band discontinuity( $\Delta E_c = 0.72\Delta E_g$ ) and a smaller valance band discontinuity, significantly improved differential gain performance at both 300 K and 375 K, and maintaining a low-transparency carrier density, enabling uncooled operation [18]. These characteristics make it a highly favorable option as an active material system for the development of low-threshold and high-speed modulation bandwidth devices.

For the laser resonance cavity, as mentioned before, the common structures are the FP laser, DFB laser and DBR laser shown in Figure 1.1.5. The FP laser is the most basic laser diode, where significant reflections of light take place at both ends. Due to its characteristics of emitting coherent light with multiple longitudinal modes and broad spectral width, this type of laser is referred to as a multi-longitudinal mode laser. In order to ensure efficient data transmission within telecom networks and prevent mode dispersion, it is necessary to utilize single-mode lasers. To achieve single longitudinal mode (SLM) operation, the use of weakly-coupled gratings is employed for guidance. The DFB laser consists of a periodic grating structure at the medium of the cavity, and DBR laser contains a Bragg mirror between the gain section and cleaved facet, both which can be designed to realize a SLM operation.

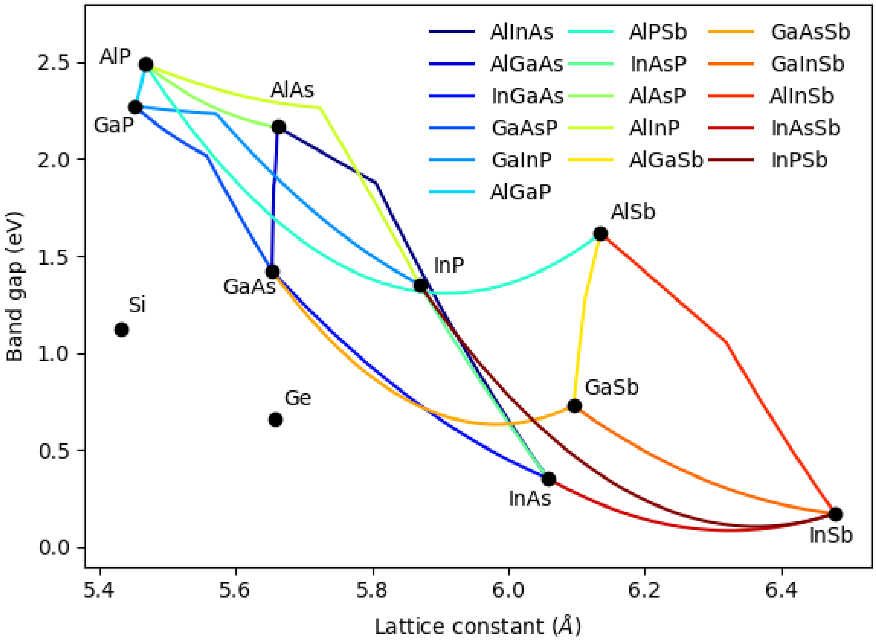

**Figure 1.1.4** Bandgap vs. lattice constant map of III-V group material [17].

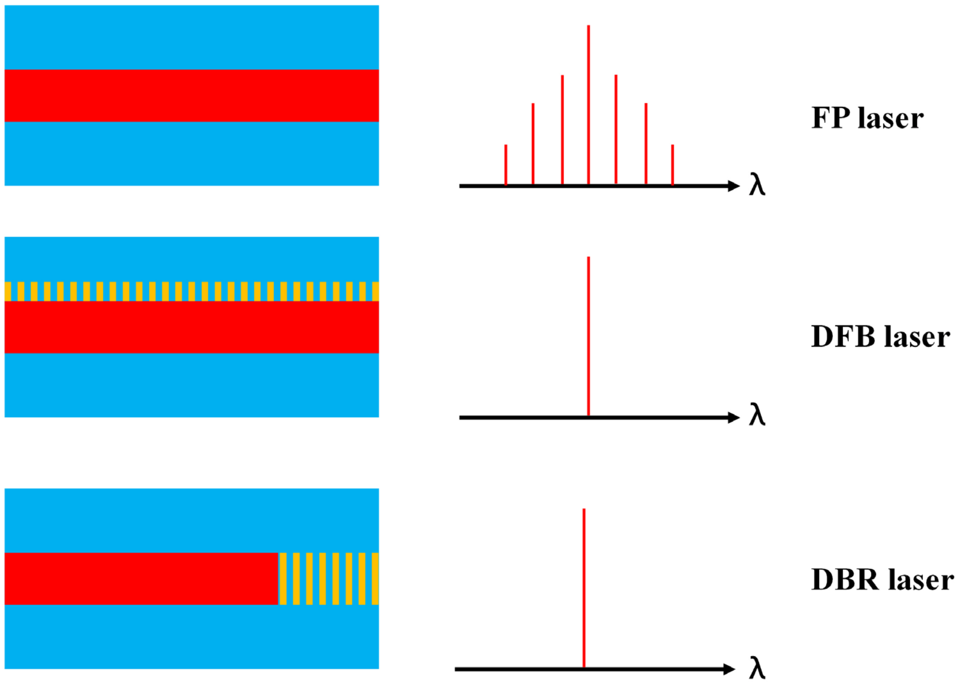

**Figure 1.1.5** Schematic of FP, DFB, and DBR lasers.

### 1.1.3 Review of polarization controller based on PIC

Controlling the polarization state of light is of significant interest in a diverse range of applications including polarimetry [19], metrology [20], and optical communication systems, particularly those utilizing high-speed complex digital signal processing (DSP) to manipulate the TE-TM polarization state of light [21] or Stokes vector modulation and direct detection (SVM-DD) systems [22, 23]. Figure 1.1.6 depicts a schematic of a 4-bit Stokes vector modulation design that facilitates the realization of a straightforward straight-line 16-level stokes vector (SV) modulator on a compact footprint without the need for electric digital-to-analogues converters (DAC) or bias control circuits. The integration of multiple wavelength channels and the application of a 50 Gbaud drive to each modulating section is anticipated to enable the development of a compact InP chip transmitter with a Tb/s capacity (50 Gbaud × 4 bits × 5λ) [2].

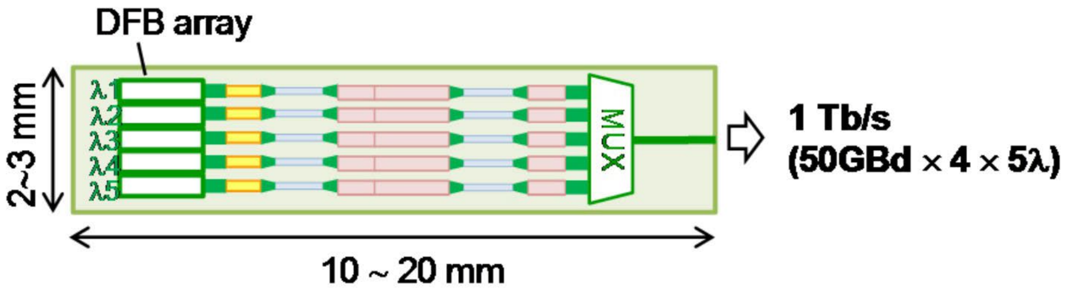

**Figure 1.1.6** Schematics of Tb/s SVM-DD Transmitter [2].

Another application of the PMC is the SV receiver as shown in Figure 1.1.7. The input signal is initially divided into three ports via a multimode interference (MMI) coupler and then transmitted through the SV rotator, which comprises symmetry waveguide (SW) and asymmetry waveguide (AW) sections. The AW section's unique length and position in each port cause the state of polarization (SOP) to be transformed into three distinct states. The differential phase shifter (DPS) subsequently detects the polarization-converted light in each port.

Among these applications, there is a growing demand for integrating a polarization controller with the light source, detectors, and other components in a PIC to cater to the aforementioned applications. As the number of devices utilizing MQW structures as the active region, including laser diodes (LDs) [24] and electro-absorption modulators [25], there is a need to design a polarization controller that is compatible with these structures.

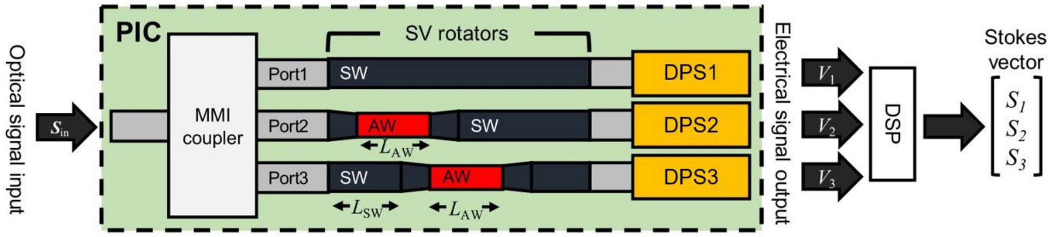

**Figure 1.1.7** Schematics of Tb/s SV receiver [2].

Polarization controllers have been proposed using various material systems and designs, such as the silicon-on-insulator (SOI) platform [26], the InGaAlAs/InP platform [25], and the GaAs/AlGaAs platform [27, 28] as shown in Fig 1.1.8. A standard waveguide polarization converter typically involves a series of PMCs and MQW polarization-dependent phase shifters (PD-PSs) [25, 29] to achieve an arbitrary

SOP. The light source can either be an external LD or a monolithically integrated laser [24, 30]. However, several PMCs that have been reported utilize bulk material as the core layer in the waveguide to achieve a high polarization conversion efficiency (PCE) in a shorter waveguide length. However, this approach necessitates relatively complex regrown butt-joint PIC techniques for integrating a bulk PMC with an MQW-based PD-PS. In [29], a passive bulk PMC was monolithically integrated with an active MQW-based PD-PS by using the butt-joint technique, which served as an efficient polarization controller in the InGaAsP/InP material system. However, the device lacked a monolithic LD. In [3], an MQW-based PMC was integrated monolithically with an MQW-based FP LD utilizing the IEL integration scheme, but the PCE was limited, with values of only 80% in [24, 31] and around 50% to 68% in [9]. To date, there have been no reports of a PMC integrated with an SLM laser, such as DFB laser.

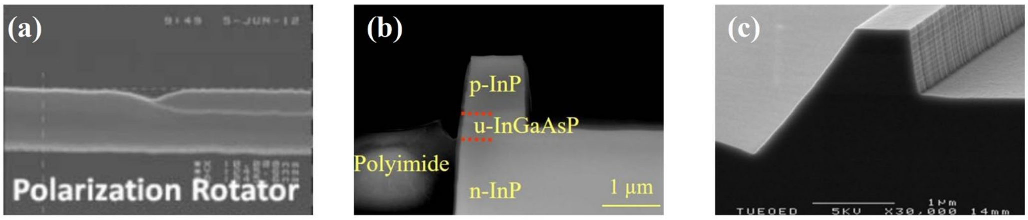

**Figure 1.1.8** Various material platforms for PMCs (a) silicon-on-insulator (SOI) platform [26], (b) InGaAsP/InP platform [25], (c) GaAs/AlGaAs platform [7].

Recently, PMCs based on the reactive ion etching (RIE) lag effect [3], slanted sidewall waveguides [7] and half-ridge structures [25] have been proposed to improve compatibility for monolithic integration as shown in Figure 1.1.9. The RIE lag-based structure features single or multiple shallow etched slots positioned asymmetrically across the width of a ridge waveguide. However, the TE-TM conversion efficiency of this structure is highly sensitive to the slot position, width, and depth, all of which are challenging to fabricate with the required precision. Notably, the depths of the slots are contingent on the RIE lag effect, which is impacted by numerous parameters within the RIE system. The slanted sidewall waveguide contains a single section, thereby eliminating transition losses. However, its fabrication typically requires numerous lithography, dry etch, and wet etch processes, which can be incompatible with the fabrication of the sidewall grating DFB laser. A half-ridge structure reduces fabrication tolerances by integrating a shallow-etched ridge structure on one side and with a deeply etched mesa structure on the other, making it feasible to integrate with a straight DFB grating waveguide. Another structure, the stepped height PMC, has simpler fabrication processes compared to the half-ridge structure and has demonstrated potential in PIC, as illustrated in Figure 1.1.9 (d).

There are two main mechanisms for achieving SOP conversion in waveguides: the mode-coupling method [28], and the mode-evolution method [32] as shown in Figure 1.1.10. The mode-coupling method exploits beating between two eigenmodes to enable polarization rotation along the PMC waveguide. The SV of the fundamental modes (Ω) is fixed inside the mode-coupling PMC, and assuming a TE-polarized input, the SOP rotates around Ω as the light propagates along the waveguide. In contrast, the Ω inside the mode-evolution PMC rotates with the extension of the PMC length, and SOP rotates along Ω. The mode-coupling approach allows for polarization conversion within a much shorter waveguide than the mode-evolution method, making it more suitable for integrating PMCs with MQW-based components such as LDs [33].

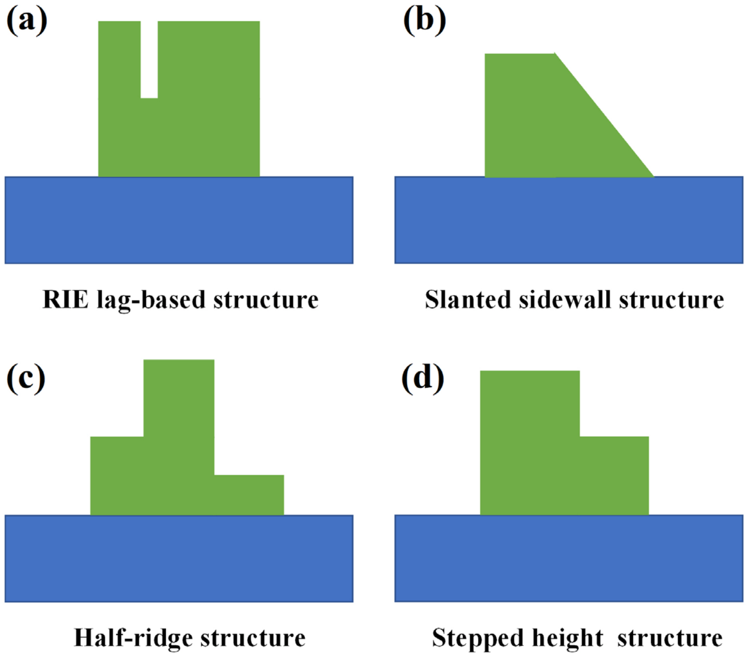

**Figure 1.1.9** Several different structures of PMCs (a) RIE lag-based structure, (b) slanted sidewall structure (c) half-ridge structure (d) stepped height structure.

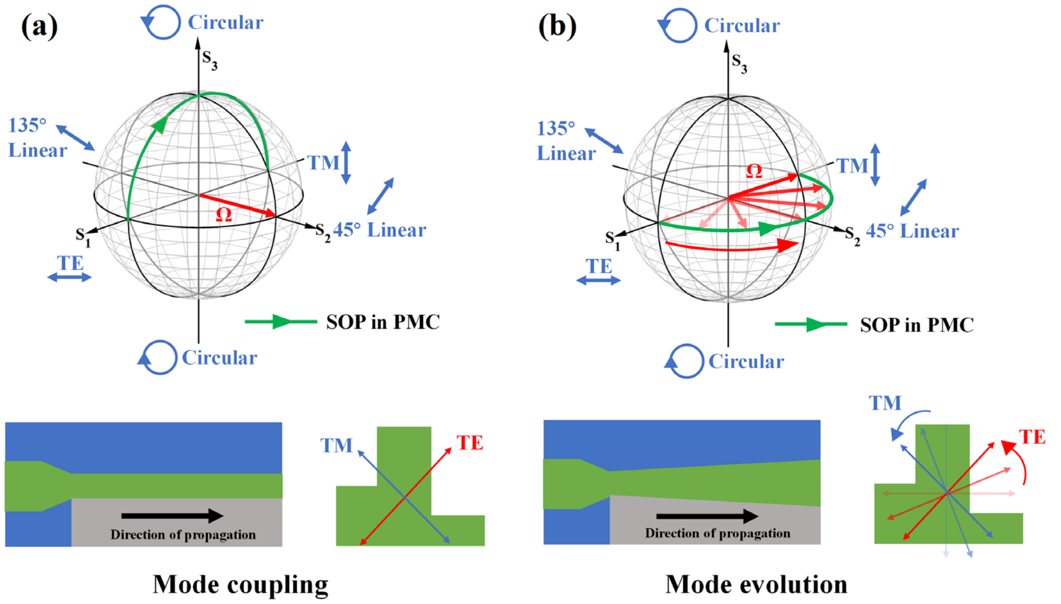

**Figure 1.1.10** Two main mechanisms for achieving SOP conversion(a) The mode beating, (b) The mode coupling.

### 1.1.4 The aim of this PhD research

In this research, we investigated an AlGaInAs multiple-quantum-well photonic integrated circuit device capable of controlling the output light source's SOP with IEL structure. The device consists of a PMC, DPS, and a side wall grating DFB laser. We demonstrate both asymmetrical half-ridge structure and stepped-height ridge waveguide PMC to achieve TE to TM polarization conversion. We employed the Finite-Element Method (FEM) to model the waveguide structure's PCE comprehensively. For the half-ridge PMC, the PCE is influenced by the width of the ridge waveguide and the ridge depths on each side, yielding a PCE of around 90.2% in an AlGaInAs MQW-based waveguide with a length of approximately 1200 μm. However, due to the thin waveguide core used in standard MQW lasers, the PMC's performance is highly sensitive to the waveguide dimensions. For the stepped-height ridge PMC, an optimized epitaxial design was proposed for monolithic integration, with a thin (300 nm thick) InGaAsP passive waveguide layer embedded underneath the MQW layer to increase the difference between the propagation constants of the two fundamental modes of the PMC, thereby reducing the half-beat length ($L_\pi$) and increasing the PCE dramatically. The top of the AlGaInAs waveguide layer acts as a dry etch stop layer, enabling precise control of the critical etch depth of the shallow etched ridge waveguide. The simulated result shows a maximum PCE of approximately 97.3% can be achieved in a 496-µm-long AlGaInAs-based PMC.

Based on simulation results, we fabricated a stepped-height ridge PMC and integrated it with a DFB laser and a symmetrical straight waveguide DPS to enable polarization rotation from approximately counterclockwise circular polarization to linear polarization. All the PMC, DPS, and DFB lasers were monolithically integrated using only a single step of MOVPE and two steps of III-V material dry etching. The resulting DFB-PMC device exhibited a high TE to TM polarization conversion efficiency (98.4%) over a wide range of DFB injection currents at a 1555 nm wavelength. For the DFB-PMC-DPS device, a nearly 60° rotation of the Stokes vector on the Poincaré sphere was obtained at a laser drive current of 170 mA and a range of bias voltage from 0 V to -3.0 V.

### 1.1.5 Thesis Outline

**Chapter 2** explains the basic theory of AlGaInAs/InP material system, conventional Bragg gratings and four phase-shifted sampled Bragg gratings(4PS-SBG) for DFB lasers. An overview of quantum well and strained quantum well materials is presented. The theory of direct and indirect band-gap transitions and the effects of heavy and light hole transitions and the absorption coefficient caused by the Quantum Confined Stark Effect are analyzed. A couple wave function based on the transfer matrix method are presented to analyse the reflection and couple efficiency in Bragg grating.

**Chapter 3** covers the materials and main fabrication steps for my novel PIC devices based on AlGaInAs/InP. A series of optimization of dry etch recipes are proposed in this chapter.

**Chapter 4** proposed the design and simulation result of a half-ridge shape PMC based on a 1550 nm LD epi-layer structure. The eigenmodes of the PMC waveguide are calculated and the optimized structure parameters, polarization converting efficiency and half-beat length are also presented.

**Chapter 5** demonstrates another kind of PMC, i.e., step-height ridge PMC. The simulation of polarization conversion efficiency and half-beat length is made and compared with half-ridge shape PMC. The fabrication process of step-height ridge PMC integrated with DFB laser is presented and the results include transparency current, optical spectrum and polarization mode conversion efficiency.

**Chapter 6** describes the integration of the DFB-PMC-DPS device. The theory of SOP adjustment with the control of the bias voltage applied at DPS is presented. The characterization and measurement of the phase shift angle is presented.

**Chapter 7** presents the theory and design of a novel EML based on 4-phase shift Bragg grating structure. An eight-channel EML array is first fabricated, and the characterization of the laser at each channel is carried out and results are presented. Measurements of novel EML array with precisely controlled wavelengths are presented, including the output optical power, the optical spectra, extinction ratio and 3dB E/O bandwidth.

**Chapter 8** is dedicated to drawing conclusions and outlining future directions. This section revisits and underscores the main points of innovation and accomplishments. It introduces two new groundbreaking InP-based devices: the 1D and 2D topological photonic crystal lasers.

# References of this chapter

[1] J. Van Der Tol, Y. Oei, U. Khalique, R. Nötzel, and M. J. P. i. Q. E. Smit, "InP-based photonic circuits: Comparison of monolithic integration techniques," vol. 34, no. 4, pp. 135-172, 2010.

[2] L. Spiekman, Y. Oei, E. Metaal, F. Green, I. Moerman, and M. J. I. p. t. l. Smit, "Extremely small multimode interference couplers and ultrashort bends on InP by deep etching," vol. 6, no. 8, pp. 1008-1010, 1994.

[3] J. Xu *et al.*, "Fully integrated multi-optoelectronic synthesizer for THz pumping source in wireless communications with rich backup redundancy and wide tuning range," vol. 6, no. 1, pp. 1-7, 2016.

[4] Y. Barbarin, X. Leijtens, E. Bente, C. Louzao, J. Kooiman, and M. J. I. P. T. L. Smit, "Extremely small AWG demultiplexer fabricated on InP by using a

double-etch process," vol. 16, no. 11, pp. 2478-2480, 2004.

[5] R. A. Griffin, S. K. Jones, N. Whitbread, S. C. Heck, and L. N. J. I. J. o. S. T. i. Q. E. Langley, "InP Mach–Zehnder modulator platform for 10/40/100/200-Gb/s operation," vol. 19, no. 6, pp. 158-166, 2013.

[6] S. Ishutkin, V. Arykov, I. Yunusov, M. Stepanenko, P. Troyan, and Y. J. S. Zhidik, "Technological Development of an InP-Based Mach–Zehnder Modulator," vol. 12, no. 12, p. 2015, 2020.

[7] K. Sekartedjo, N. Eda, K. Furuya, Y. Suematsu, F. Koyama, and T. J. E. L. Tanbun-Ek, "1.5 µm phase-shifted DFB lasers for single-mode operation," vol. 2, no. 20, pp. 80-81, 1984.

[8] G. Sarlet, G. Morthier, and R. J. J. o. l. t. Baets, "Control of widely tunable SSG-DBR lasers for dense wavelength division multiplexing," vol. 18, no. 8, p. 1128, 2000.

[9] P. F. Liao and P. Kelley, *Quantum well lasers*. Elsevier, 2012.

[10] M. L. MaSanoviC, E. J. Skogen, J. S. Barton, V. Lal, D. J. Blumenthal, and L. A. Coldren, "Demonstration of monolithically-integrated InP widely-tunable laser and SOA-MZI wavelength converter," in *International Conference onIndium Phosphide and Related Materials, 2003.*, 2003, pp. 289-291: IEEE.

[11] Y. Barbarin *et al.*, "Butt-joint interfaces in InP/InGaAsP waveguides with very low reflectivity and low loss," in *Proc. IEEE/LEOS Symp. Benelux*, 2005, pp. 89-92.

[12] K. Tomioka *et al.*, "Selective-area growth of III-V nanowires and their applications," vol. 26, no. 17, pp. 2127-2141, 2011.

[13] S. K. Si, D. H. Yeo, H. H. Yoon, and S. J. J. I. J. o. s. t. i. q. e. Kim, "Area selectivity of InGaAsP-InP multiquantum-well intermixing by impurity-free vacancy diffusion," vol. 4, no. 4, pp. 619-623, 1998.

[14] C. McLean, A. McKee, G. Lullo, A. Bryce, R. De La Rue, and J. J. E. L. Marsh, "Quantum well intermixing with high spatial selectivity using a pulsed laser technique," vol. 31, no. 15, pp. 1285-1286, 1995.

[15] W. Xia *et al.*, "Ion mixing of III-V compound semiconductor layered structures," vol. 71, no. 6, pp. 2602-2610, 1992.

[16] J. Haysom *et al.*, "Quantum well intermixing caused by nonstoichiometric InP," in *Conference Proceedings. 2000 International Conference on Indium Phosphide and Related Materials (Cat. No. 00CH37107)*, 2000, pp. 56-59: IEEE.

[17] A. Bett, F. Dimroth, G. Stollwerck, and O. J. A. P. A. Sulima, "III-V compounds for solar cell applications," vol. 69, pp. 119-129, 1999.

[18] J. Yong, J. M. Rorison, and I. H. J. I. j. o. q. e. White, "1.3-/spl mu/m quantum-well InGaAsP, AlGaInAs, and InGaAsN laser material gain: a theoretical study," vol. 38, no. 12, pp. 1553-1564, 2002.

[19] T. Yoshizawa, *Handbook of optical metrology: Principles and Applications*. CRC press, 2017.

[20] M.-C. Amann, T. M. Bosch, M. Lescure, R. A. Myllylae, and M. J. O. e. Rioux, "Laser ranging: a critical review of unusual techniques for distance measurement," vol. 40, pp. 10-19, 2001.

[21] P. J. Winzer, D. T. Neilson, and A. R. Chraplyvy, "Fiber-optic transmission and networking: the previous 20 and the next 20 years [Invited]," *Optics Express,* vol. 26, no. 18, pp. 24190-24239, 2018/09/03 2018.

[22] S. Ghosh, Y. Kawabata, T. Tanemura, and Y. Nakano, "Polarization-analyzing circuit on InP for integrated Stokes vector receiver," *Optics express,* vol. 25, no. 11, pp. 12303-12310, 2017.

[23] D. Che and W. Shieh, "Polarization demultiplexing for Stokes vector direct detection," *Journal of Lightwave Technology,* vol. 34, no. 2, pp. 754-760, 2016.

[24] B. Holmes, M. Naeem, D. Hutchings, J. Marsh, and A. Kelly, "A semiconductor laser with monolithically integrated dynamic polarization control," *Optics express,* vol. 20, no. 18, pp. 20545-20550, 2012.

[25] M. Kazi *et al.*, "High-speed carrier-injection-based polarization controller with InGaAlAs/InAlAs multiple-quantum wells," *IEEE Photonics Technology Letters,* vol. 29, no. 22, pp. 1951-1954, 2017.

[26] S. I. H. Azzam, N. F. Areed, M. M. Abd-Elrazzak, H. El-Mikati, and S. S. Obayya, "Compact polarization rotator based on SOI platform," in *2014 31st National Radio Science Conference (NRSC)*, 2014, pp. 288-293: IEEE.

[27] U. Khalique *et al.*, "Ultrashort polarization converter on InP/InGaAsP fabricated by optical lithography," in *Integrated Photonics Research and Applications*, 2005, p. IWA3: Optica Publishing Group.

[28] A. E. Elfiqi, R. Kobayashi, R. Tanomura, T. Tanemura, and Y. Nakano, "Fabrication-tolerant half-ridge InP/InGaAsP polarization rotator with etching-stop layer," *IEEE Photonics Technology Letters,* vol. 32, no. 11, pp. 663-666, 2020.

[29] M. Ito *et al.*, "Efficient InGaAsP MQW-based polarization controller without

active-passive integration," *Optics Express,* vol. 29, no. 7, pp. 10538-10545, 2021.

[30] M. A. Naeem and K. Abid, "A novel full polarisation controller integrated monolithically with a semiconductor laser," in *Asia Communications and Photonics Conference*, 2015, p. AM1A. 2: Optica Publishing Group.

[31] J. Bregenzer, S. McMaster, M. Sorel, B. Holmes, and D. Hutchings, "Polarisation mode converter monolithically integrated within a semiconductor laser," presented at the Conference on Lasers and Electro-Optics, 2008.

[32] A. E. Elfiqi *et al.*, "Robust InP/InGaAsP polarization rotator based on mode evolution," *IEEE Photonics Technology Letters,* vol. 34, no. 2, pp. 109-112, 2022.

[33] X. Sun *et al.*, "Simulation of an AlGaInAs/InP Electro-Absorption Modulator Monolithically Integrated with Sidewall Grating Distributed Feedback Laser by Quantum Well Intermixing," *Photonics,* vol. 9, no. 8, p. 564, 2022.

# Chapter 2 Theory

## 2.1 Theory of MQW energy band

Quantum well devices entail numerous intricate physical mechanisms. Prior to fabricating semiconductor MQW devices, simulating and calculating specific characteristics of semiconductor lasers holds immense practical significance. This endeavour not only enhances comprehension of pertinent physical phenomena but also steers research directions, thereby enhancing efficiency in research and development. This chapter will meticulously outline theoretical aspects including energy band characteristics, Quantum-confined Stark effect(QCSE), chirp factor as a function of the electric field, and gain spectrum of III/V semiconductor MQW lasers.

### 2.1.1 $In_{1-x}Ga_xAs_yP_{1-y}$ and $In_{1-x-y}Ga_xAl_yAs$ material system

For the quaternary lattice compound, the relation between the lattice constant and the component can be defined by Vegard law. This law presents a linear interpolation method for computing various physical parameters, denoted by physical parameters *P*. The formulas for $In_{1-x}Ga_xAs_yP_{1-y}$ and $In_{1-x-y}Ga_xAl_yAs$ are given as [1] The parameter *P* can present several physical parameters, such as the effective mass of electron and hole, lattice constant and etc. Because the material in MQW is based on $In_{1-x-y}Ga_xAl_yAs$, the values of the material parameters can be found in Table 2.1.1

$$\begin{aligned} &P(In_xGa_xAs_yP_{1-y}) \\ &\quad = P(GaAs)xy + P(GaP)x(1-y) + P(InAs)(1-x)y + P(InP)(1-x)(1-y) \end{aligned} \tag{2.1.1}$$

$$\begin{aligned} &P(In_{1-x-y}Ga_xAl_yAs) \\ &\quad = P(GaAs)x + P(InAs)(1-x-y) + P(AlAs)y \end{aligned} \tag{2.1.2}$$

**Table 2.1.1.** The AlGaInAs material parameters [2-5]

| Parameters | Symbol (unit) | $Al_xGa_yIn_{1-x-y}As$ |
|---|---|---|
| Lattice Constant | $a$ (Å) | $5.600x+5.6533y+6.0584(1-x-y)$ |
| Elastic Stiffness Constant | $C_{11}$ ($10^{11}$ dyn/cm$^2$) | $1.25x+1.1879y+0.8329(1-x-y)$ |
|  | $C_{12}$ ($10^{11}$ dyn/cm$^2$) | $0.534x+0.5376y+0.4526(1-x-y)$ |
| Hydrostatic deformation potential for conduction band | $a_c$ (eV) | $-5.64x-7.17y-5.08(1-x-y)$ |
| Hydrostatic deformation potential for valence band | $a_v$ (eV) | $2.47x+1.16y+0.66(1-x-y)$ |
| Shear deformation potential | $b$ (eV) | $-1.5x-1.7y-1.8(1-x-y)$ |
| Electron effective mass | $m_e/m_0$ | $0.15x+0.067y+0.023\ (1-x-y)$ |
| Heavy-hole effective mass | $m_{hh}/m_0$ | $0.7x+0.5y+0.517\ (1-x-y)$ |
| Light-hole effective mass | $m_{lh}/m_0$ | $0.1415x+0.088y+0.024\ (1-x-y)$ |
| Valence band parameter | $\gamma_1$ | $3.45x+6.8y+20.4(1-x-y)$ |
|  | $\gamma_2$ | $0.68x+1.9y+8.3(1-x-y)$ |
|  | $\gamma_3$ | $1.29x+2.73y+9.1(1-x-y)$ |

## 2.1.2 Bulk Bandgap with Strain

By introducing an optimal level of strain in a thin quantum well, it is possible to prevent the formation of dislocations and defects, and also enhancing the performance of the device in numerous ways. These include improvements in the threshold current of the MQW laser, differential gain, polarization characteristics, chirp of the electroabsorption modulator, and other related characteristics. The effects of strain are attributed to the changes in the energy bands of the conduction and valence bands. The impact of strain on the bottom of the conduction band and the top of the valence band will be discussed briefly below.

The unstrained bandgap for $In_{1-x-y}Ga_xAl_yAs$ is:

$$E_g(x,y)=1.35+0.642x-1.101y+0.758x^2+0.101y^2-0.159xy-0.28x^2y+0.109xy^2 eV \quad \textbf{(2.1.3)}$$

The effects of strain are calculated in the following way. First, the strain in the plane of the epitaxial growth is：

$$\varepsilon=\varepsilon_{xx}=\varepsilon_{yy}=\frac{a_0-a}{a} \quad \textbf{(2.1.4)}$$

where $a$ is the lattice constant of the quaternary epitaxial layer and $a_0$ is the lattice constant of the substrate which is assumed to be InP. The conduction band is shifted by the energy:

$$\delta E_c = a_c(\varepsilon_{xx} + \varepsilon_{yy} + \varepsilon_{zz}) = 2a_c(1 - \frac{C_{12}}{C_{11}})\varepsilon \qquad \textbf{(2.1.5)}$$

and the valence bands are shifted by:

$$\delta E_{hh} = -P_\varepsilon - Q_\varepsilon \qquad \textbf{(2.1.6)}$$

$$\delta E_{lh} = -P_\varepsilon + Q_\varepsilon \qquad \textbf{(2.1.7)}$$

$$P_\varepsilon = -a_v(\varepsilon_{xx} + \varepsilon_{yy} + \varepsilon_{zz}) = -2a_v(1 - \frac{C_{12}}{C_{11}})\varepsilon_{\|} \qquad \textbf{(2.1.8)}$$

$$Q_\varepsilon = -\frac{b}{2}(\varepsilon_{xx} + \varepsilon_{yy} - 2\varepsilon_{zz}) = -b(1 + \frac{C_{12}}{C_{11}})\varepsilon_{\|} \qquad \textbf{(2.1.9)}$$

Where $a_c$ and $a_v$ are the conduction-band and valence-band hydrostatic deformation potentials and $b$ is the valence-band shear deformation potential.

The strained bandgaps can then be expressed as:

$$E_{c-hh}(x,y) = E_g(x,y) + \delta E_c(x,y) - \delta E_{hh}(x,y) \quad \text{(Heavy hole)} \qquad \textbf{(2.1.10)}$$

$$E_{c-lh}(x,y) = E_g(x,y) + \delta E_c(x,y) - \delta E_{lh}(x,y) \quad \text{(Light hole)} \qquad \textbf{(2.1.11)}$$

Consequently, the QW has three strain conditions: compressive strain ($\varepsilon < 0$), matched strain ($\varepsilon = 0$) and tensile strain ($\varepsilon > 0$). The effect of strain on the band profile is shown in Fig.2.1.1

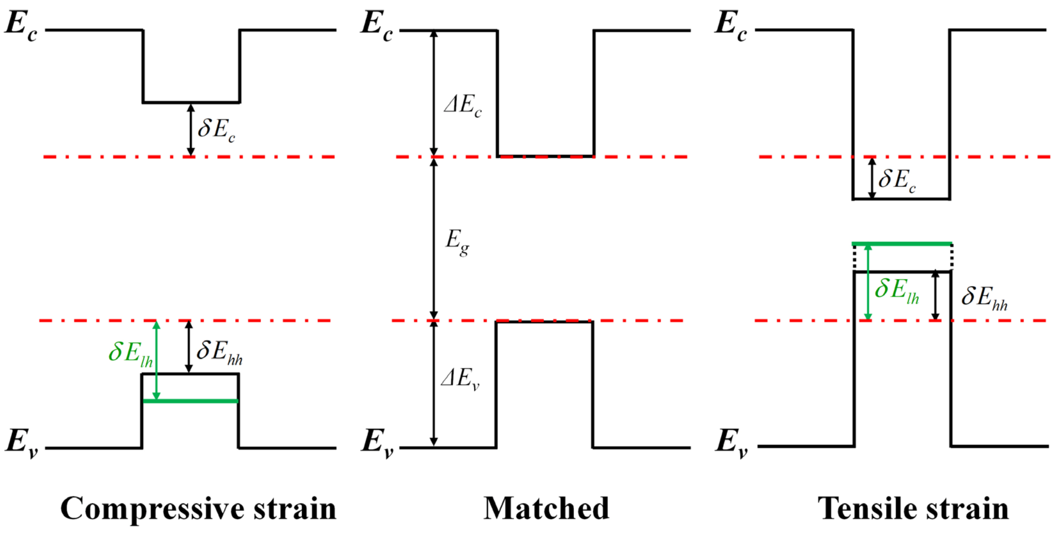

**Figure 2.1.1** Band-edge profile for the compressive strained, un-strained and tensile strained quantum wells.

### 2.1.3 Quantum-confined Stark effect

In quantum well structures, electrons and holes are confined in potential wells, and their vertical energy levels form discrete spectral lines while their horizontal energy levels form sub-bands. The binding energy of excitons between the conduction band electrons and valence band holes in quantum well structures is far greater than that of bulk materials. The photon absorption in this quantum well structure includes two parts: one is the electron on the valence sub-band absorbing photons to be excited to the conduction band sub-level, and another is the exciton absorption peak that is located near the sub-band transition absorption, due to the effects of various broadening mechanisms, both the conduction- valence band transition and the exciton absorption peak are broadened. The total absorption spectrum as shown in Figure 2.1.2.

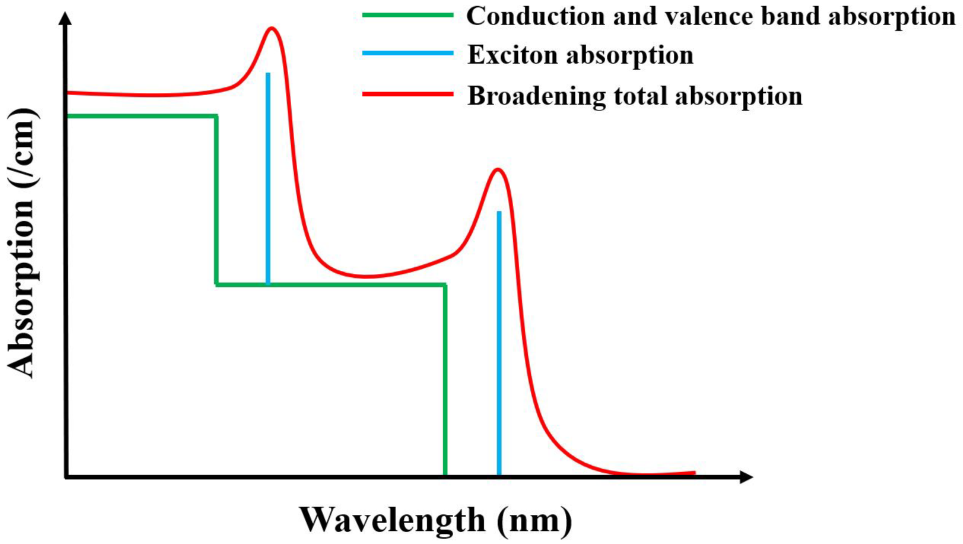

**Figure 2.1.2** Photon absorption in quantum well structure.

The Quantum-Confined Stark Effect (QCSE) is a phenomenon in semiconductor nanostructures, such as quantum wells, quantum wires, and quantum dots, where the electronic and optical properties of these structures are influenced by an externally applied electric field. Under no external electric field, the energy bands of the well and barrier layers are horizontal along the growth direction, and the conduction band electrons and valence band holes are symmetrically distributed in the middle of the well. When an external electric field is applied perpendicular to the quantum well, the energy bands of the quantum well become tilted. The distribution of electrons and holes are respectively shifted towards the two ends of the quantum well. The sub-band levels decrease and the absorption positions between the sub-bands move towards the longer wavelength direction, resulting in the movement of the exciton absorption peak and further broadening of the exciton absorption spectrum. These two effects cause the absorption coefficient near the original absorption edge to increase sharply with the increase of the external electric field.

## 2.1.4 Calculation of sub band energy of quantum well

The subband structure can be determined using the Schrödinger equation with the BenDaniel–Duke model [6] which applies the envelope function approximation. The one-dimensional Schrödinger equation for the quantum wells is:

$$-\frac{\hbar^2}{2}\frac{d}{dz}\left[\frac{1}{m^*(z)}\frac{d\chi(z)}{dz}\right]+(V(z)+qFz)\chi(z)=E_{r1}\chi(z) \tag{2.1.12}$$

where the growth direction z is the confinement axis, $\chi(z)$ is the envelope wave function, $E_{r1}$ is the quantized energy level, m $m^*(z)$ is the carrier effective mass in the z direction, $V(z)$ is the confinement potential of QW, which depends on the band gap of the epitaxial layers, the band discontinuity between the conduction band and the valence band (for AlInGaAs $\Delta E_c / \Delta E_g = 0.72$), and the band shift caused by strain.

By the finite difference method (FDM), the numerical differential form of the one-dimensional Schrödinger equation (7) is [7]:

$$\alpha_i\chi_{i-1}+(\gamma_i+U_i)\chi_i+\beta\chi_{i+1}=E_{r1}\chi_i \tag{2.1.13}$$

$$U_i=V_i+qF_iZ_i \tag{2.1.14}$$

$$\alpha_i=-\frac{\hbar^2}{2}\frac{2}{\Delta z_{i-1}(\Delta z_{i-1}+\Delta z_i)}\frac{2}{m_i^*+m_{i-1}^*} \tag{2.1.15}$$

$$\beta_i=-\frac{\hbar^2}{2}\frac{2}{\Delta z_i(\Delta z_{i-1}+\Delta z_i)}\frac{2}{m_i^*+m_{i+1}^*} \tag{2.1.16}$$

$$\gamma_i=-\alpha_i-\beta_i \tag{2.1.17}$$

Consider the boundary condition as zero boundaries:

$$\chi_0=\chi_{N+1}=0 \tag{2.1.18}$$

Equation (2.1.13) has:

$$(\gamma_1+U_1)\chi_1+\beta_1\chi_2=E_{r1}\chi_1 \tag{2.1.19}$$

$$\alpha_N\chi_{N-1}(\gamma_N+U_N)\chi_N=E_{r1}\chi_N \tag{2.1.20}$$

The matrix form of the equation is:

$$A\{\chi\}=E\{\chi\} \tag{2.1.21}$$

$$A = \left\{ \begin{matrix} \gamma_1 + U_1 & \beta_1 & & & \\ \alpha_2 & \gamma_2 + U_2 & \beta_2 & & \\ & \alpha_i & \gamma_i + U_i & \beta_i & \\ & & \alpha_N & \gamma_N + U_N & \end{matrix} \right\} \qquad \textbf{(2.1.22)}$$

For any bandgap structure, the different number of quantized energy levels and wavefunction $\chi(z)$ can be calculated in MATLAB if matrix $A$ is defined.

Based on a commercially available 1550 nm AlGaInAs/InP LD structure[8], the effect of the electric field on the electron and heavy hole (HH) ground state wave functions are shown in Fig. 2.3.2 The field-induced shift of the electron eigenfunction is to the left and the HH eigenfunction to the right. Thus, in the presence of an electric field, the overlap integral between the electron and HH wave functions is reduced.

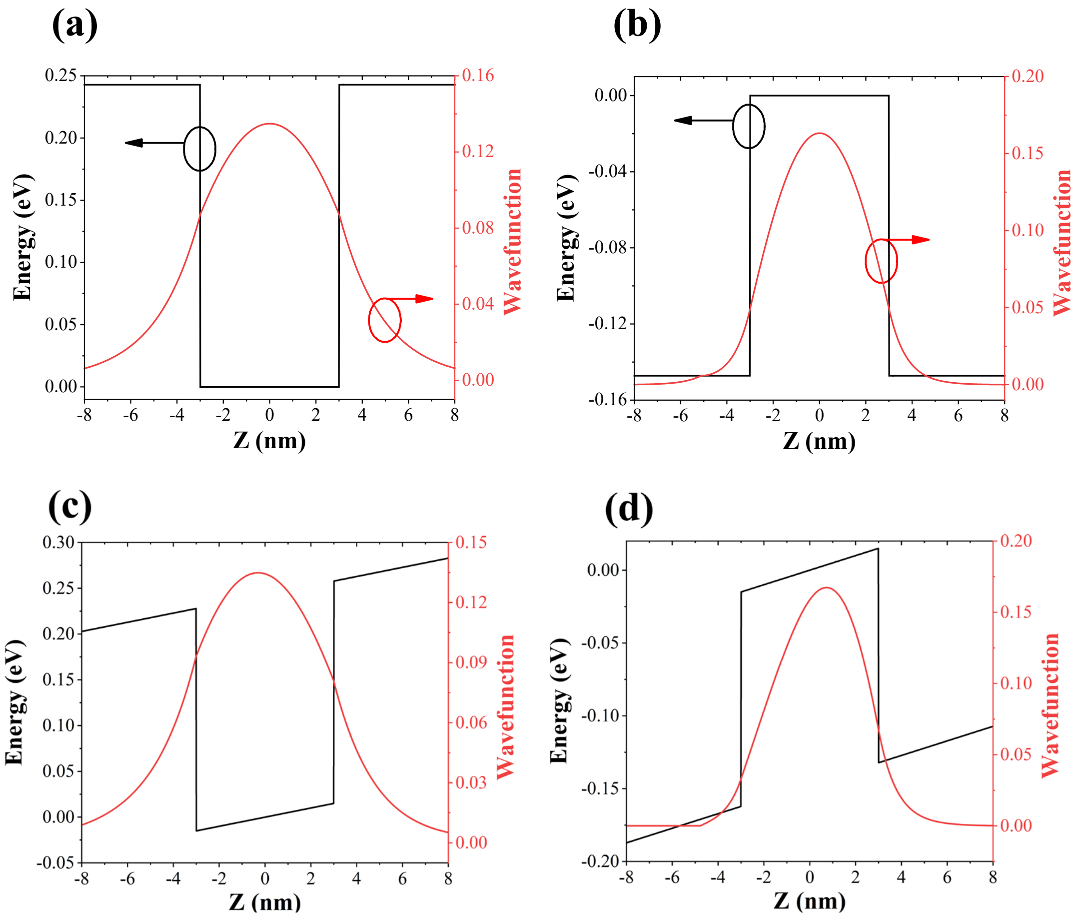

**Figure 2.1.3** Calculated band energy and wavefunction of QW: (a) conduction band at 0 kV/cm electric field, (b) HH valence band at 0 kV/cm electric field, (c) conduction band at 50 kV/cm electric field, (d) HH valence band at 50 kV/cm electric field.

### 2.1.6 Chirp factor

The calculation of absorption coefficient has been calculated for the 1550 nm AlGaInAs/InP LD structure. The chirp factor $\alpha_H$ of the EAM is calculated from:

$$\alpha_H = \frac{\delta n}{\delta k} = \frac{4\pi}{\lambda}\frac{\delta n}{\delta \alpha} \tag{2.1.23}$$

where $\delta\alpha$ is the differentiation of the absorption coefficient to photonics energy. $\delta n$ is the change in refractive index. the change in absorption coefficient ($\delta\alpha$) using the Kramers−Krönig relationship [4].

$$\delta n(E) = \frac{c\hbar}{\pi}\int_0^{\infty}\frac{\delta\alpha(E')}{E'^2 - E^2}dE' \tag{2.1.24}$$

where $E$ is the photon energy, $\hbar$ is Planck's constant divided by $2\pi$, and the total absorption coefficient, $\alpha$, is the sum of the absorption coefficient of the exciton resonance in the quantum well ($\alpha_{ex}$) and the absorption coefficient between the conduction and valence band transition ($\alpha_{con}$). They are expressed as [5]:

$$\alpha_{ex} = \sum_{i,j}\frac{4e^2\hbar\ |p_{cv}|^2}{\varepsilon_0 c n m_0^2 E_{\mathrm{ex}(i,j)}\lambda_{\mathrm{ex}(i,j)}^2 L_z}\left|\langle \chi_{ci} \mid \chi_{vi}\rangle\right|^2 B(\hbar\omega - E_{ex(i,j)}) \tag{2.1.25}$$

$$\alpha_{con} = \frac{\mu e^2\ |p_{cv}|^2}{\varepsilon_0 c n m_0^2 \hbar^2 \omega L_z}\sum_{i,j}\left|\langle \chi_{ci} \mid \chi_{vi}\rangle\right|^2 \left|\int_{E_{cv(i,j)}}^{\infty} S(E, E_{cv(i,j)})L(E,\hbar\omega)dE\right. \tag{2.1.26}$$

$$\alpha = \alpha_{ex} + \alpha_{con} \tag{2.1.27}$$

where $\chi_{ci}$ and $\chi_{vi}$ represent the envelope wave functions of the conduction and valence bands, respectively, the parameters $n$, $c$ and $\varepsilon_0$ correspond to the refractive index, the velocity of light in vacuum, and the permittivity of free space, The width of the as-grown QW is represented by $L_z$. $B$ is gaussian convolution of broadening functions. $S$ is the Sommerfeld enhancement factor and $L$ is the Lorentzian broadening factor, $p_{cv}$ is the optical matrix element at the band edge.

Figure 2.1.4 presents the calculated chirp factor ($\alpha_H$) for as-grown QW. For the as-grown QW, $\alpha_H$ tends to negative infinity at 1.531 μm and then moves in a positive direction with increasing wavelength for 0 kV/cm electric field, and the zero point of $\alpha_H$ moves to longer wavelengths as the electric field increases as shown in Fig. 2.3.3(a). In Fig. 2.1.4(b), the dependence of $\alpha_H$ with electric field at 1.55 μm and 1.56 μm wavelength is indicated, and $\alpha_H$ reduces to 0 at 60 kV/cm.

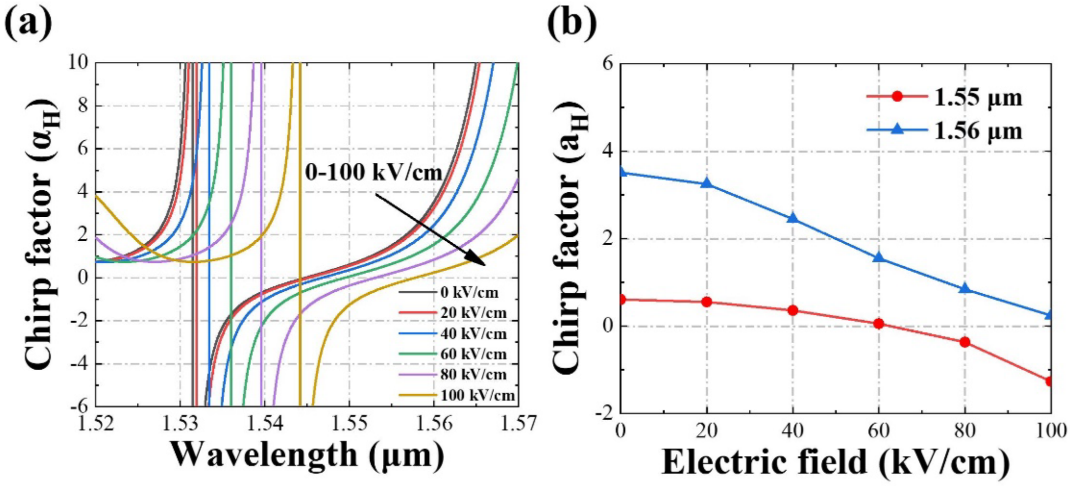

**Figure 2.1.4** (a) Simulated chirp factor of as-grown QW as a function of wavelength, and (b) chirp factor for as-grown QW as a function of the electric field at operating wavelengths of 1.55 μm and 1.56 μm.

## 2.1.6 Calculation of the gain spectrum in QW

The local gain spectrum corresponding to the transition of electrons from the i$^{th}$ sub-level of the conduction band to the j$^{th}$ level of the valence band can be expressed as [5]:

$$g_{ij}(\omega)=\frac{\pi e^2}{m_0^2\varepsilon_0 c n_{eff}\omega}\left|p_{cv}\right|^2\left|\langle\chi_{ci}\mid\chi_{vi}\rangle\right|^2\rho_{cv,ij}(f_{c,i}-f_{v,j}) \tag{2.1.28}$$

Where $p_{cv}$ is the optical matrix element at the band edge, $\rho_{cv,ij}$ is the joint density of states of the conduction and valence bands, $f_{c,i}$ and $f_{v,j}$ are the Fermi distribution functions of the conduction and valence bands, respectively. For the $p_{cv}$, we have:

$$\left|p_{cv}\right|^2=M_{cv}\left|M_0\right|^2 \tag{2.1.29}$$

$$\left|M_0\right|^2=\frac{m_0^2}{m_c^*}\frac{E_g(E_g+\Delta_0)}{12(E_g+\frac{3}{2}\Delta_0)} \tag{2.1.30}$$

Where $\Delta_0$ is the spin-orbit splitting, $m_0$ and $m^*_c$ represent the free electron mass and the effective mass of conduction band electrons, $M_{cv}$ is the polarization factor which is different for TE and TM:

$$\begin{aligned}
&TE : M_{cv,hh} = \frac{3}{4} + \frac{3}{4}\cos(\theta) \\
&TM : M_{cv,hh} = \frac{3}{2} - \frac{3}{2}\cos(\theta) \\
&TE : M_{cv,lh} = \frac{5}{4} - \frac{3}{4}\cos(\theta) \\
&TM : M_{cv,lh} = \frac{1}{2} + \frac{3}{2}\cos(\theta) \\
&\cos(\theta) = \begin{cases} E_{i,j}^{0} / E & (E > E_{i,j}^{0}) \\ 1 & (E < E_{i,j}^{0}) \end{cases}
\end{aligned} \tag{2.1.31}$$

The joint density of states $\rho_{cv,ij}$ is given as:

$$\rho_{cv,ij} = \frac{m_{c,v}}{\pi \hbar^2 L_z} h(\hbar\omega - E_{ij}^{0}) \tag{2.1.32}$$

Where

$$h(\hbar\omega - E_{ij}^{0}) = \begin{cases} 0 & (\hbar\omega > E_{ij}^{0}) \\ 1 & (\hbar\omega < E_{ij}^{0}) \end{cases} \tag{2.1.33}$$

$$\frac{1}{m_{c,v}} = \frac{1}{m_{c//}} + \frac{1}{m_{v//}} \tag{2.1.34}$$

$m_{c//}$ and $m_{v//}$ are the effective mass in the plane, the Fermi distribution functions $f_{c,i}$ and $f_{v,j}$ are:

$$f_{c,j} = 1 + e^{\frac{E_i^0 + \frac{m_{c,v}}{m_c}(E - E_{i,j}^0) - E_{fn}}{KT}} \tag{2.1.35}$$

$$f_{v,j} = 1 + e^{\frac{E_j^0 + \frac{m_{c,v}}{m_v}(E - E_{i,j}^0) - E_{fp}}{KT}} \tag{2.1.36}$$

$E_{fn}$ and $E_{fp}$ represent the quasi-Fermi levels of the conduction and valence bands, which can be obtained through the electron and hole densities:

$$n = \sum_i \rho_i kT \ln(1 + e^{\frac{E_{fn} - E_j}{kT}}) \tag{2.1.37}$$

$$p = \sum_j \rho_j kT \ln(1 + e^{\frac{E_{fn} - E_j}{kT}}) \tag{2.1.38}$$

$n$ and $p$ are the diffusion of electron and valence. $\rho_i$ and $\rho_j$ is the i$^{th}$ and j$^{th}$ electron and valence density of states. Figure 2.1.5 shows the material gain of the 5-QW structure in chapter 4.

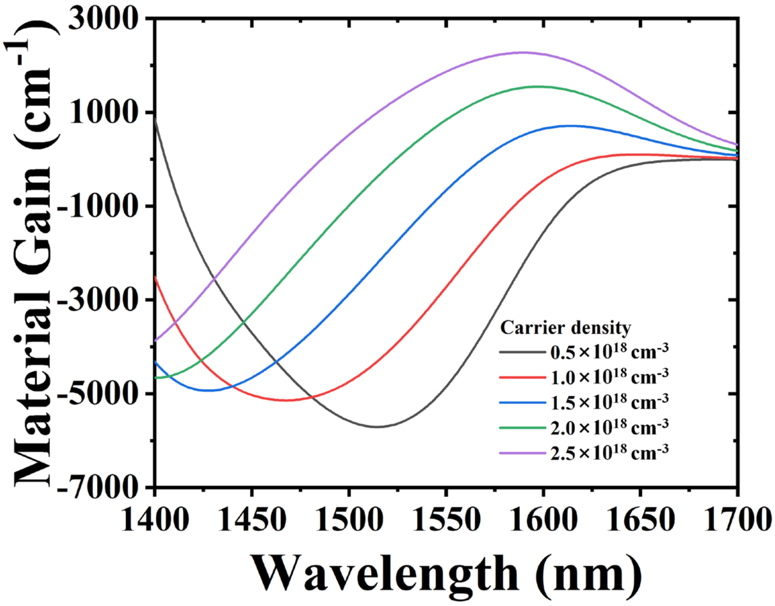

**Figure 2.1.5** Material gain of the 5-QW structure.

# 2.2 Theory of Bragg Grating Reflection

The calculated MQW material gain, as discussed in Section 2.1, plays a crucial role in determining the lasing wavelength, which is influenced by the period and structure of the Bragg grating. This section introduces the pertinent theory of Bragg gratings.

## 2.2.1 Coupling mode theory and transfer matrix method

The initial focus of this discussion will be on the fundamental principles of Bragg gratings. When an optical waveguide is subject to a perturbation in refractive index, it induces an optical coupling between propagating modes. This perturbation is usually achieved using two materials, each with a distinct refractive index of $n_1$ and $n_2$, where $n_2$ is greater than $n_1$ and the difference between them is significantly smaller than $n_1$ (shown in Figure 2.2.1). The Fresnel equations indicate that light reflection occurs at the interface of these two materials. When light is incident at normal angles, the reflection coefficient, $r$, can be expressed as:

$$r = \frac{n_2 - n_1}{n_2 + n_1} \tag{2.2.1}$$

$$t = \frac{2n_1}{n_2 + n_1} \tag{2.2.2}$$

The condition of the Bragg grating condition is:

$$m\lambda_B = 2n_{eff}\Lambda \quad (m \in N+) \tag{2.2.3}$$

$$\beta_B = \frac{2\pi n_{eff}}{\lambda_B} \tag{2.2.4}$$

$\Lambda$ is the period of Bragg grating, and $m$ represents the grating's order. $\lambda_B$ is the free space wavelength satisfying the Bragg propagating mode, $n_{eff}$ is the effective refractive index of the corresponding waveguide mode. The Bragg propagation constant is $\beta_B$

Although diffracted light is changed with different grating orders, there are always unique forward transmitted waves and feedback waves along the grating face. Interaction occurs between the diffracted waves and incident waves. Considering this interaction is weak, a coupled wave model can model this phenomenon[9].

The One-dimensional Helmholtz equation of parallel grating is [ 1]:

$$\frac{\partial^2 \vec{E}(z)}{\partial z^2} + k(z)^2 \vec{E}(z) = 0 \tag{2.2.5}$$

where $\vec{E}(z)$ is the forward and backward propagating electric fields. For reflection index $\overline{n}(z)$ and amplitude gain factor $\overline{g}(z)$, One-dimensional spatial distribution can be fitted as simple harmonic:

$$\overline{n}(z) = \overline{n} \ + \overline{n}_1 \cos(2\beta_B z + \varphi_{\overline{n}}) \tag{2.2.6}$$

$$\overline{g}(z) = \overline{g} \ + \overline{g}_1 \cos(2\beta_B z + \varphi_{\overline{g}}) \tag{2.2.7}$$

$\overline{n}_1$ , $\overline{g}_1$, $\varphi_{\overline{n}}$, $\varphi_{\overline{g}}$ are the amplitude and phase of medium perturbation respectively. The medium spatial distribution coefficient $k(z)$ can be described as:

$$k(z) = \frac{2\pi}{\lambda}\overline{n} \ (z) + i\overline{g} \ (z) \tag{2.2.8}$$

Where $\lambda$ is the free space wavelength. Under perturbation theory, $k(z)^2$ can be given as:

$$k(z)^2 \approx \beta_B{}^2 + 4\kappa\beta\cos(2\beta_B z) + 2i\bar{g}\beta_B \tag{2.2.9}$$

$\kappa$ is the coupling coefficient:

$$\kappa = \sqrt{\left(\frac{\pi\bar{n}_1}{\lambda_B}\right)^2 + \left(\frac{\bar{g}_1}{2}\right)^2} e^{\frac{\bar{g}_1\lambda_B}{2\pi\bar{n}_1}} \tag{2.2.10}$$

For the rectangular-shape gratings, the $\kappa$ is given as[10]:

$$\kappa = \frac{n_1^2 - n_2^2}{2n_{eff}^2\lambda_B}\Gamma \tag{2.2.11}$$

Where $\Gamma$ is the optical confinement factor of the grating area.

In principle, a medium subjected to periodic spatial perturbations is expected to produce an infinite number of diffraction orders. However, the maximum amplitude is predominantly observed in proximity to the Bragg frequency, where phase synchronism is achieved. Consequently, in the context of DFB lasers, the coupling between the transmitted wave and the feedback wave is of paramount importance. It is postulated that the wave propagating along the grating interface is constituted by the transmitted wave *R*(z) and the feedback wave *S*(z). The total wave transmission in the medium is:

$$\vec{E}(z) = R(z)e^{-i\beta_B z} + S(z)e^{i\beta_B z} \tag{2.2.12}$$

The coupled mode equation can be given as:

$$-\frac{\delta R(z)}{\delta z} + i\Delta\beta R(z) = i\kappa S(z) \tag{2.2.13}$$

$$\frac{\delta S(z)}{\delta z} + i\Delta\beta S(z) = i\kappa R(z) \tag{2.2.14}$$

where $\Delta\beta$ is the detuning around $\beta_B$, with $\Delta\beta << \beta_B$. The general solutions of the coupled mode equation:

$$R(z) = \frac{1}{a_2 - a_1}[a_2 C_1 e^{(i\Delta\beta + a_1 i\kappa)z} - a_1 C_2 e^{(i\Delta\beta + a_2 i\kappa)z}] \tag{2.2.15}$$

$$S(z)=\frac{1}{a_2-a_1}[C_1e^{(-i\Delta\beta+a_1i\kappa)z}-C_2e^{(-i\Delta\beta+a_2i\kappa)z}] \tag{2.2.16}$$

$a_1$ and $a_2$ are the solutions of the equation:

$$-2i\Delta\beta a+i\kappa a^2+ia=0 \tag{2.2.17}$$

Consider the strong coupling condition The solution of the $R(z)$ and $S(z)$ are:

$$R(z)=\left[\cosh(\gamma z)-\frac{i\Delta\beta}{\gamma}\sinh(\gamma z)\right]R(0)-\frac{i\kappa}{\gamma}\sinh(\gamma z)S(0) \tag{2.2.18}$$

$$S(z)=\left[\cosh(\gamma z)+\frac{i\Delta\beta}{\gamma}\sinh(\gamma z)\right]R(0)+\frac{i\kappa}{\gamma}\sinh(\gamma z)R(0) \tag{2.2.19}$$

Where $\gamma^2=\kappa^2-\Delta\beta^2$. These equations can be written into a matrix form:

$$\frac{R(z)}{S(z)}=\begin{bmatrix}\cosh(\gamma z)-\frac{i\Delta\beta}{\gamma}\sinh(\gamma z) & \frac{i\kappa}{\gamma}\sinh(\gamma z)\\ \frac{i\kappa}{\gamma}\sinh(\gamma z) & \cosh(\gamma z)+\frac{i\Delta\beta}{\gamma}\sinh(\gamma z)\end{bmatrix}\frac{R(0)}{S(0)}=T\frac{R(0)}{S(0)} \tag{2.2.20}$$

*T* is called the transfer matrix. For phase-shifted gratings, the Bragg gratings are not continuous and there is a phase shift $\varphi$, the phase-shift matrix is:

$$T_\varphi=\begin{bmatrix}\exp\left(\frac{-i\varphi}{2}\right) & 0\\ 0 & \exp\left(\frac{i\varphi}{2}\right)\end{bmatrix} \tag{2.2.21}$$

For the Bragg grating with *N* period sections, the total transmission can be calculated my transfer matrix method (TMM):

$$\frac{R(z)}{S(z)}=\prod_{i=1}^{N}T_i\frac{R(0)}{S(0)} \tag{2.2.22}$$

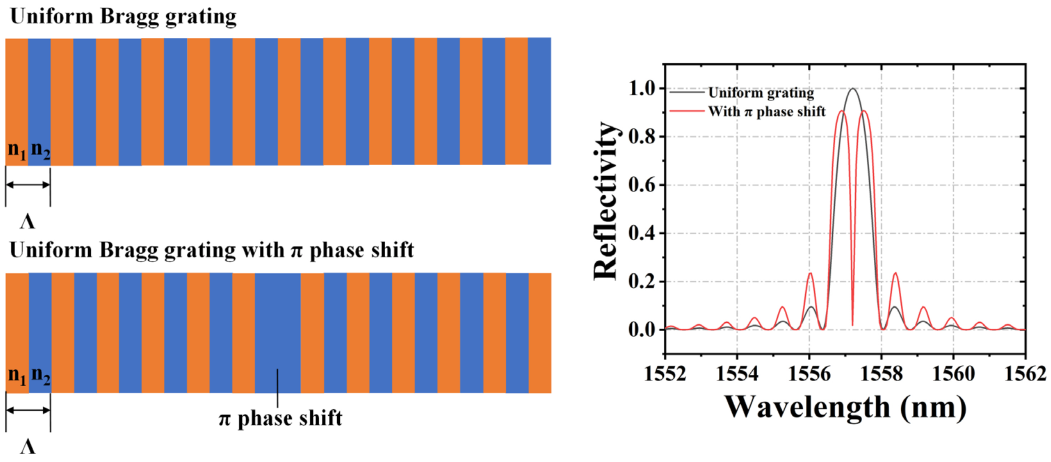

**Figure 2.2.**1 Schematic of uniform Bragg grating(upper left) and uniform Bragg grating with π phase shift in middle of the cavity(lower left), and calculated reflectivity of the uniform Bragg grating and π phase shift Bragg grating(right).

## 2.2.2 Four phase-shifted sampled Bragg gratings

Fig. 2.2.2(a) and (b) show schematics of the C-SBG and the 4PS-SBG, respectively. For the C-SBG, half of the sampling period (*P*) has no grating, resulting in the coupling efficiency $\kappa$ in ±1st channel decreasing to only 1/π times that of a uniform grating. For the 4PS-SBG, the grating in each sampling period is evenly divided into four sections with each adjacent grating section subjected to a π/2 phase shift. This structure simultaneously enhances the effective κ of the +1st channels to 0.90 times that of a uniform Bragg grating and eliminates the 0th channel reflection [11].

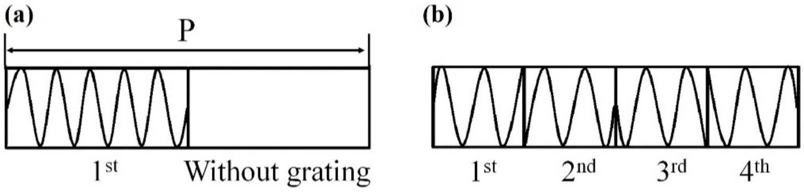

**Figure 2.2.2** Grating structures of (a) C-SBG, (b) 4PS-SBG. *P* is the sampling period.

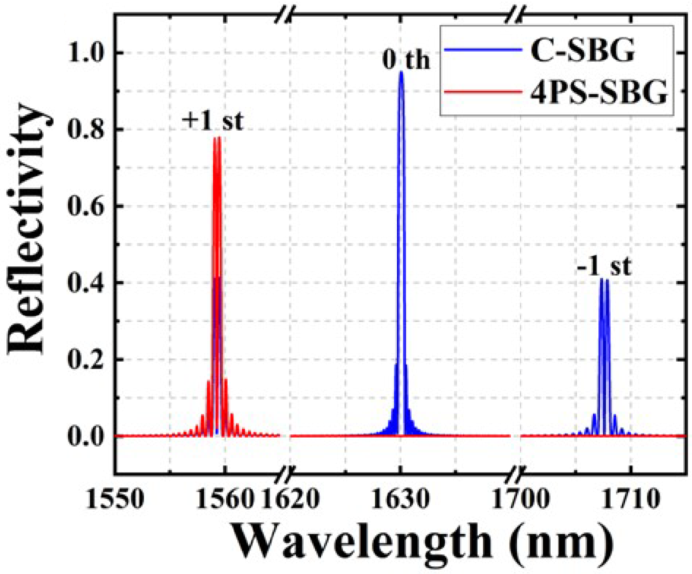

**Figure 2.2.3** Calculated reflection spectra of 4PS-SBG with a π phase-shift in the centre of the cavity (red curve) and compared with that of the C-SBG (blue curve).

Using the TMM, we calculated the reflection and time-delay spectra of the 4PS-SBG structure, which are shown in Fig. 2.2.3. Compared with the C-SBG structure, in the 4PS-SBG structure, the $0^{th}$ channel disappears and the $+1^{st}$ channel is significantly enhanced as shown in Fig. 2.2.3. When a π phase-shift of the seed grating period $\Lambda_0$is inserted into the middle of the cavity, a resonance peak that represents the lasing mode appears in the center of the stopband of the $+1^{st}$ channel. The wavelength of the $+1^{st}$ channel can be expressed as

$$\lambda_{+1} = 2n_{eff} \cdot \frac{P\Lambda_0}{P+\Lambda_0} \tag{2.2.23}$$

where $n_{eff}$ is the effective refractive index of the ridge waveguide, $P$ is the sampling period and $\Lambda_0$ is the seed grating period as described above. For the designed and calculated values, $\Lambda_0$ is 257 nm, which locates the $0^{th}$ channel at 1630 nm; the $+1^{st}$ channel, used as the output channel, is located at the gain peak of the MQW material, which is around 1550 nm; $n_{eff}$ is 3.19 and the dispersion coefficient is −0.00021/nm. Based on the above data and considering the electro-beam lithography (EBL) resolution limit to be 0.5 nm, we designed an 8 single longitudinal mode (SLM) laser array (CH1 to CH8). The $P$ for CH1 to CH8 was changed from 4.418 μm to 4.759 μm. The detailed designed values of the $P$ and the corresponding lasing wavelengths are shown in Table 2.2.1. a difference in sampling period of 48.7 nm results in lasing wavelengths being separated by 0.8 nm. This sampling period difference is much larger than that of the EBL's typical resolution of 0.5 nm and so is straightforward to fabricate.

**Table 2.2.1** The sampling period *P* values for different lasing wavelength

| **Channel No.** | **Sampling period *P*** | **Wavelength** |
|---|---|---|
| CH1 | 4.418μm | 1548.4 nm |
| CH2 | 4.467 μm | 1549.2 nm |
| CH3 | 4.515 μm | 1550.0 nm |
| CH4 | 4.564 μm | 1550.8 nm |
| CH5 | 4.613 μm | 1551.6 nm |
| CH6 | 4.662 μm | 1552.4 nm |
| CH7 | 4.710 μm | 1553.2 nm |
| CH8 | 4.759 μm | 1554.0 nm |

# References of this chapter

[1] J. Minch, S. Park, T. Keating, and S. Chuang, "Theory and experiment of In Ga As P and In Ga Al As long-wavelength strained quantum-well lasers," *IEEE J. Quantum Electron,* vol. 35, no. 5, pp. 771-782, 1999.

[2] E. H. Li, "Material parameters of InGaAsP and InAlGaAs systems for use in quantum well structures at low and room temperatures," *Physica E: Low-dimensional systems and Nanostructures,* vol. 5, no. 4, pp. 215-273, 2000.

[3] C. Pryor, "Eight-band calculations of strained InAs/GaAs quantum dots compared with one-, four-, and six-band approximations," *Physical Review B,* vol. 57, no. 12, p. 7190, 1998.

[4] I. Vurgaftman, J. á. Meyer, and L. á. Ram-Mohan, "Band parameters for III–V compound semiconductors and their alloys," *Journal of applied physics,* vol. 89, no. 11, pp. 5815-5875, 2001.

[5] S. Adachi, "GaAs, AlAs, and Al x Ga1− x As: Material parameters for use in research and device applications," *Journal of Applied Physics,* vol. 58, no. 3, pp. R1-R29, 1985.

[6] D. BenDaniel and C. Duke, "Space-charge effects on electron tunneling," *Physical review,* vol. 152, no. 2, p. 683, 1966.

[7] K. Kawano and T. Kitoh, *Introduction to Optical Waveguide Analysis: Solving Maxwell's Equation and the Schrödinger Equation*. John Wiley & Sons, 2004.

[8] L. Hou *et al.*, "Subpicosecond Pulse Generation at Quasi-40-GHz Using a Passively Mode-Locked AlGaInAs–InP 1.55-μm Strained Quantum-Well Laser," *IEEE Photonics Technology Letters,* vol. 21, no. 23, pp. 1731-1733, 2009.

[9] T. J. J. o. l. t. Erdogan, "Fiber grating spectra," vol. 15, no. 8, pp. 1277-1294, 1997.

[10] H. Ghafouri-Shiraz, *Distributed feedback laser diodes and optical tunable filters*. John Wiley & Sons, 2003.

[11] L. Jingsi *et al.*, "A Multiexposure Technology for Sampled Bragg Gratings and its Applications in Dual-Wavelength Lasing Generation and OCDMA En/Decoding," *IEEE Photonics Technology Letters,* vol. 21, no. 21, pp. 1639-1641, 2009.

# Chapter 3 Fabrication

This section presents a summary of the main fabrication steps for photonic integrated circuits (PICs). The fabrication process flow for all PIC devices can be broadly categorized into eight sequential steps, encompassing marker definition, waveguide isolation, waveguide dry etching, opening contact windows, P-contact metallization, and thinning and cleaving.

## 3.1 Marker definition

Initially, alignment markers were established to ensuring accurate alignment between successive lithography steps. For EBL, well-defined markers with high contrast are crucial due to the automatic alignment process. While etched markers and metallized markers can both serve as alignment markers for EBL, this study used metallized markers to attain superior contrast.

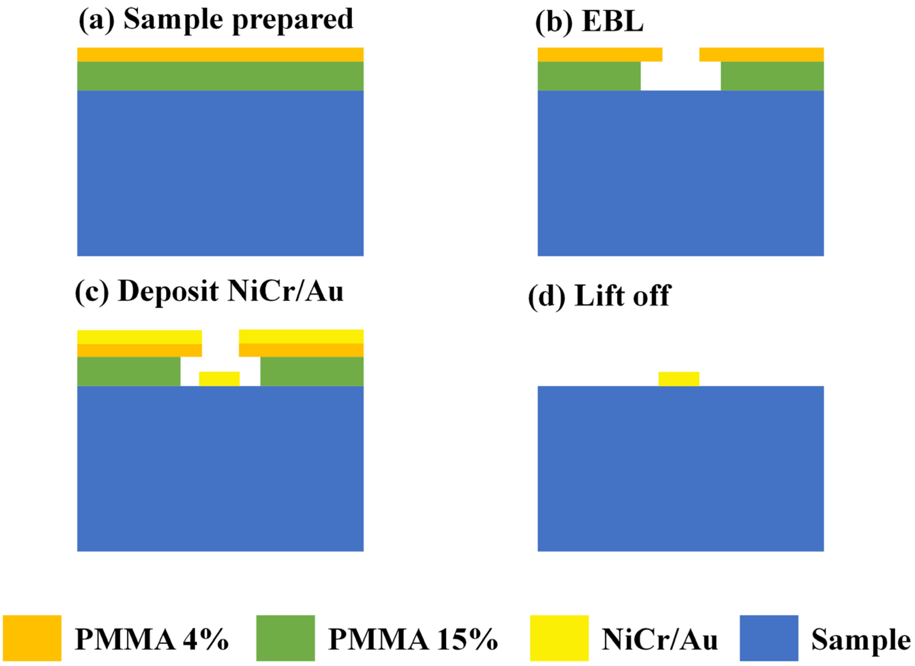

**Figure 3.1.1** The process flow of lift-off technique.

Figure 3.1.1 illustrates the sequence of steps involved in the marker definition. The process involved the spinning of two distinct layers of Polymethyl methacrylate (PMMA) on the sample, where the first layer is 15% of 2010 PMMA at 4000 rpm for 60s, the thickness is 1.2 μm. The second layer is 4% of 2041 PMMA at 4000 rpm for 60s with thickness at 110 nm. The first PMMA layer was subjected to baking at 180°C for 30 minutes before the second PMMA layer was spun, followed by an additional 90 minutes of baking at 180°C to eliminate the solvents in the resists. The second PMMA layer had lower sensitivity to electron beams compared to the first layer due to its higher molecular weight, resulting in an undercut profile of the resist after development (shown in Fig.3.1.1(b)). Following the exposure of the sample to electron beams, a mixture of methyl isobutyl ketone (MIBK) and isopropyl alcohol (IPA) was used for development, with a ratio of 2:1 of MIBK: IPA. The sample was immersed in MIBK: IPA (2:1) for 30 seconds at 23°C, then rinsed in IPA at room temperature for 15 seconds before being blown dry and sent for metal deposition.

The metal deposition was utilized which comprised of two distinct layers: the initial layer consisted of Nichrome (NiCr) and the subsequent layer was composed of Gold (Au). These layers were deposited with thicknesses of 30 nm and 100 nm respectively, and the method employed for deposition was electron-beam evaporation within the JWNC facility. The process entailed heating metal targets using electron beams, resulting in the generation of metal vapour. Upon reaching the sample surface, this metal vapour facilitated the deposition process, as shown in Fig.3.1.1(c). Then the sample was dipped into Acetone (water bath at 50 °C) for about 15 minutes to remove the PMMA and the overlaying metal layer, then the metal marker was deposited at the sample surface in Fig.3.1.1(d). Figure 3.1.2 shows the micrograph of the markers, there was an Au bar arranged in a parallel orientation to the left edge of the sample. This was intended to ensure that the cleaving lines, as part of the final step, were also parallel to the crystallographic axis. During electron beam lithography (EBL), the coarse alignment was achieved automatically with the aid of the cross which had a branch width of 50 μm. There are two rolls of small markers at the top and the bottom of the sample to facilitate fine alignment, for accurate management of rotational and translational alignment, a set of four markers were employed. The left half markers

(No.1-6) were uniformly positioned at a 500 μm scale. To further enhance the precision of the marker alignment, the right half markers (No.7-12) were unevenly distributed, with varying scales between adjacent markers ranging from 500 μm to 900 μm.

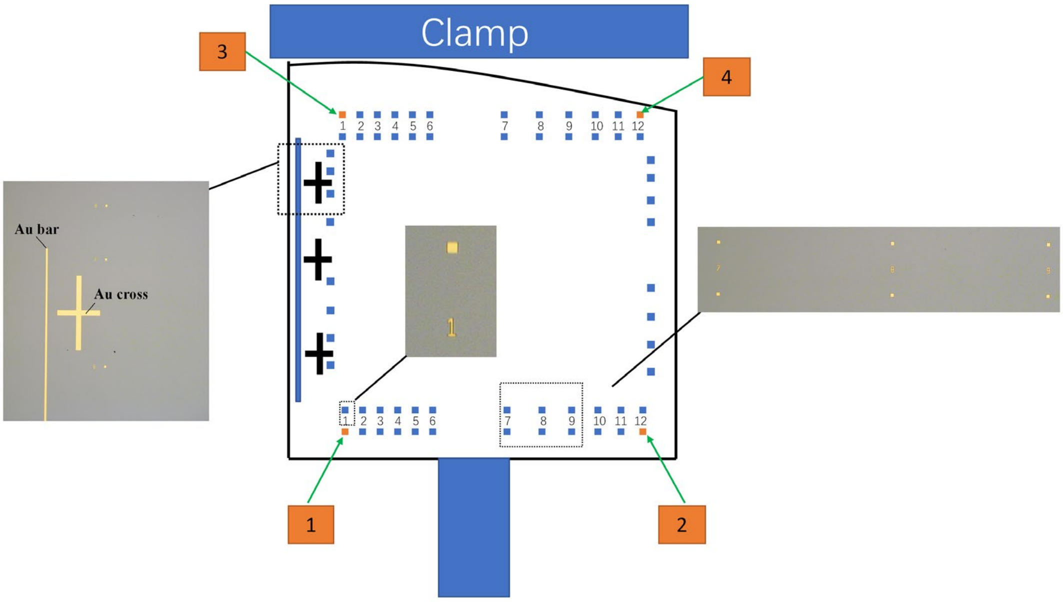

**Figure 3.1.2** Schematic of Markers for the Sample.

# 3.2 Waveguide isolation

## 3.2.1 ICP dry etch

Inductively Coupled Plasma (ICP) dry etch is a type of dry etching process used in the microelectronics industry to fabricate microelectronic devices, particularly for creating high-aspect-ratio features with high precision and accuracy. It involves the use of a high-density plasma generated by applying radio frequency (RF) energy to a gas mixture and generating plasma. The ICP dry etch system consists of a vacuum chamber, a gas delivery system, an ICP power source, and a wafer holder as shown in Fig.3.2.1. The wafer holder is typically made of a conductive material and serves as the anode in the etching process. The sample is put on a silicon carrier wafer placed on the wafer holder, metal, $SiO_2$, $SiN_x$ and resist are common masks in ICP dry etch. ICP is created by applying a high frequency alternating current to a coil of wire, which generates a strong magnetic field. The magnetic field induces an electric current in the plasma, which heats and ionizes the gas molecules. The resulting plasma is typically made up of ions and electrons. Neutral atoms such as hydrogen atom also can be generated during the dry-etch process, the interferometer is used to monitor the dry-etch thickness. The interferometer includes a 670 nm laser source. It works by splitting a beam of light into two or more separate beams, when the beams reflect from the sample surface their phase will change, which are then recombined to produce interference patterns that can be used to make precise measurements. Figure 3.2.2 reflectivity trace from the interferometer for the 5-QW DFB laser wafer. From the change of trace curve, the range of ohm-contact layer, InP cladding, SCH, MQW and InP substrate can be approximately defined.

In this research, the machine used for InP dry etch is an Oxford Instruments PlasmaPro System 100 ICP Cobra. The etch recipes is based on the gas mixture of Chlorine ($Cl_2$) [1-3]. and Methane Hydrogen ($CH_4/H_2$)[4]. $Cl_2$ based chemistries can improve the etch rate and methane hydrogen was chosen to reduce the etch temperature (set at 60 °C in this work).

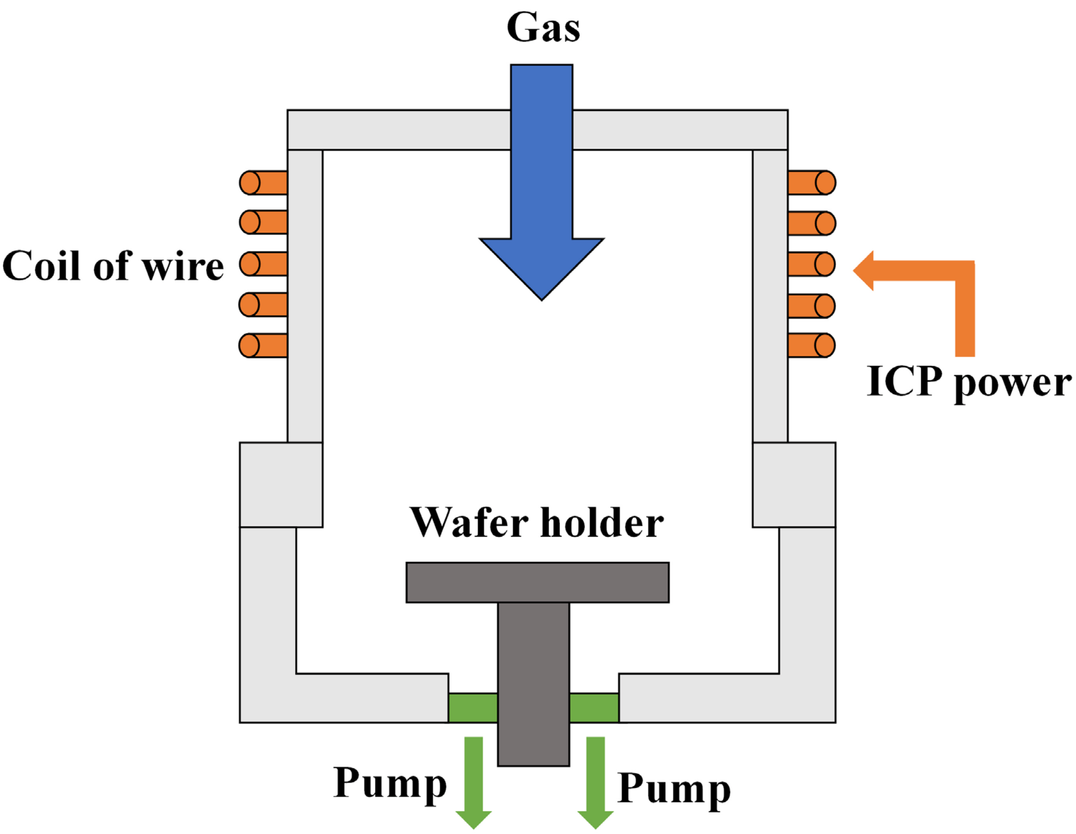

**Figure 3.2.1** A diagram of a common ICP set-up.

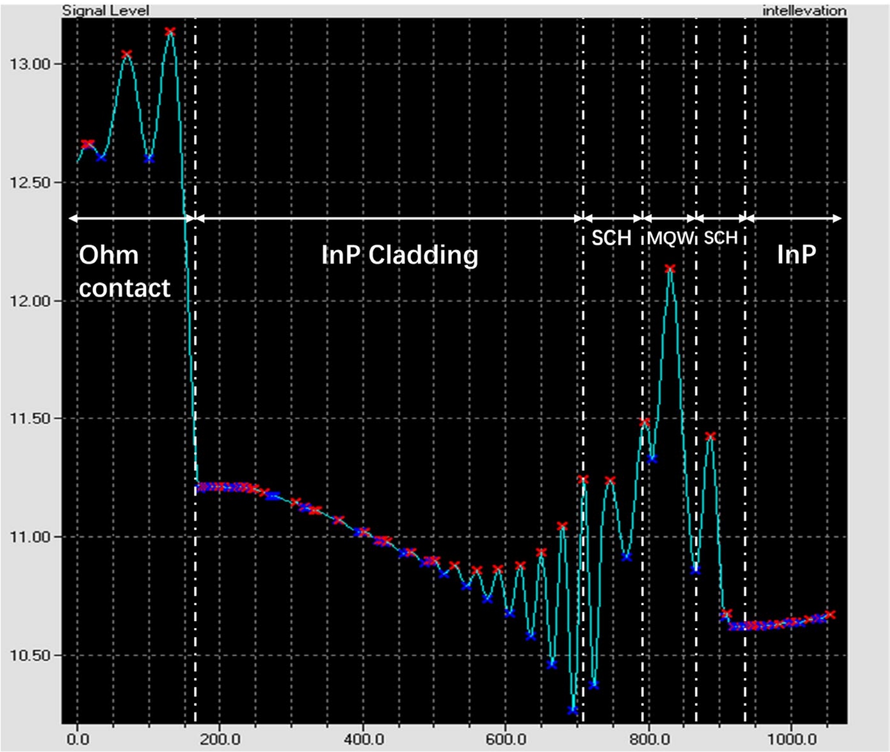

**Figure 3.2.2** A reflectivity trace from the interferometer for the 5-QW DFB laser wafer (recipe: $Cl_2/CH_4/H_2/Ar$:8/10/15/10).

### 3.2.2 Waveguide isolation steps

In semiconductor laser designs that feature multiple electrodes, electrical isolation is a crucial aspect to enable the independent operation of different electrodes. For the DFB laser integrated with either the PMC or EAM, their ohm contact should be isolated. A standard solution was employed, which involved the removal of the highly doped contact layers located on top of the wafer structure, the process steps are depicted in Fig.3.2.3. The first step is spinning two layers (2.4 µm thick) of 15% of 2010 PMMA, baking on 180-degree oven bake for 90 min for the first layer PMMA and 5 min 180-degree hotplate baking for the second layer resist. After the EBL and development, the 250 nm ohm contact layer was removed by the ICP dry etch, the chosen recipe is $Cl_2/CH_4/H_2/Ar$: 8/10/15/10, The ICP power and RF platen power of the machine were 750 and 150 W respectively, and the gas pressure in the chamber was 5 mTorr. The reflectivity trace can be referred to Fig. 3.2.2. For a total 250 nm etched thickness, an average etch rate of 94 nm/min was calculated. The isolation resistance for the isolation width of around 20-50 um which realize a 2000-ohm isolation resistance.

**(a) Resist spinning** **(b) EBL**

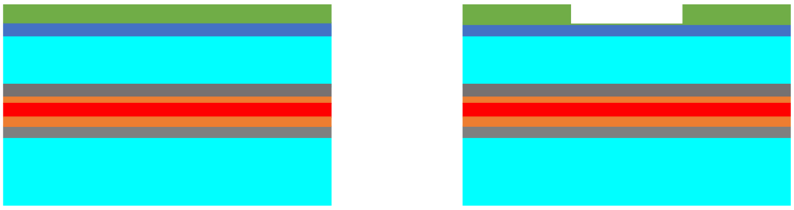

**(c) ICP dry etch** **(d) Clean resist**

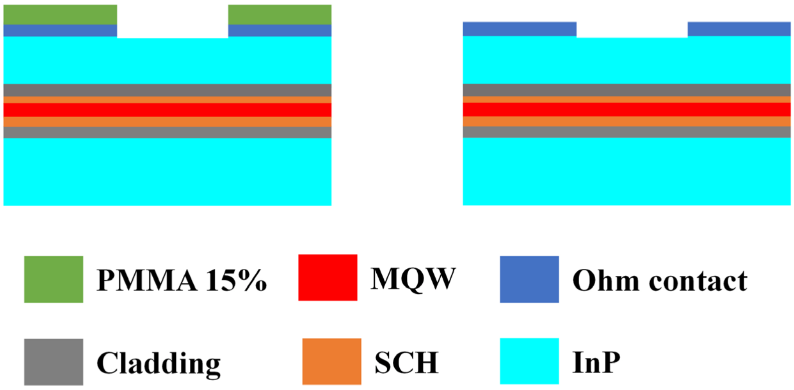

**Figure 3.2.3** The process flow of waveguide isolation.

# 3.3 Waveguide define and dry etch

The fabrication of side-wall DFB lasers for active functionality requires multiple lithographic and etch/deposition processes for high precision and accuracy of the realized devices. The e-beam lithography technique was used due to the nano-scale patterns required in the design which need high resolution and rapid prototyping capabilities. Besides, the machine used for the dry etch of the InP/AlGaInAs semiconductors was Oxford Instruments Plasma Pro System 300 Cobra (Cluster), the recipes used for sidewall grating fabrication requires optimization by series of dry etch test. This section describes the e-beam method and dry etch optimization steps.

## 3.3.1 Electron-beam lithography

The sub-micrometer and nanometer-scale features of the devices fabricated in this study required the use of EBL for patterning the design onto the substrate. To achieve this, an

EBPG5200 e-beam tool, considered as a state-of-the-art EBL machine, available at the James Watt Nano Fabrication Center (JWNC), University of Glasgow, was employed. The design patterns for EBL were created in a computer-aided design (CAD) package called L-Edit©, which has its own internal format. The patterns were then saved in the GDSII format, which is compatible with the e-beam writer. A Cjob file was generated from the GDSII file and submitted to the EBPG tool using the Belle software. The beam current, spot size, and exposure dose settings were defined in Belle to ensure the necessary charge per unit area ($\mu C/cm^2$) to expose the resist.

EBL relies on the use of radiation-sensitive compounds called EBL resists, which can be classified as either positive or negative depending on their response to electron exposure. Poly-Methyl Methacrylate (PMMA) is a commonly used positive e-beam resist, while Hydrogen Silsesquioxane (HSQ) is a commonly used negative e-beam resist. The sensitivity and contrast of the EBL resist structure are important parameters that define its performance. Sensitivity is the energy required to retain the complete thickness of the exposed region after development, while contrast is the selectivity between exposed and unexposed regions. Ideally, EBL resists should have high sensitivity to allow for faster exposure processes and high contrast to achieve vertical profiles after development.

During the EBL process, the resist is patterned by exposing it to a focused electron beam. The primary electrons of the beam are scattered in both the resist layer and the substrate material beneath; this scattering generates secondary electrons as they traverse the resist, and both contribute to the total exposure dose at all substrate regions. Consequently, regions adjacent to those initially addressed by the electron beam receive a higher total electron dose than intended, resulting in an imprecise implementation of a designed pattern on a sample with respect to size and shape. This effect is well-known as the proximity effect.

To reduce the proximity effect and improve the precision of the pattern. The dose should be reallocated for different pattern depending on their size and shape. In addition, if large and small structures are placed close to each other, the variation in pattern density leads to a variation in the total electron dose at each point of the design. This procedure is known as proximity effect correction (PEC). In this research, Monte Carlo simulation is used to calculate the dose distribution for small patterns such as grating. Figure 3.3.1 shows the PEC simulation result for a 600 nm HSQ resist on 370 μm InP substrate.

In this work, the grating structures were defined onto the substrate using the negative tone e-beam resist, HSQ. The advantage of using this resist is that it forms a $SiO_2$ pattern after development, which can be used as a hard mask for subsequent etching, eliminating the need for an additional etch mask and extra fabrication steps. However, HSQ is sensitive to baking temperature, and overheating or underheating can affect the lithography development process. Spin coats the first e-beam resist layer with lower molecular weight HSQ at 2000 rpm for 60 seconds. This produces a 1.2 μm thick resist layer.

1. Clean the backside of the sample with acetone-soaked cotton bud and place it on the hot plate at 90 ºC for 10 minutes.
2. Expose the ridge waveguide structure with EBPG e-beam writer. EBPG control parameters are: resolution: 0.5 nm, proximity correction file: GaAs700-100_z650.xrz, dose: 1000 μC/cm$^2$, spot size: 36 nm, beam current 8.43 nA.
3. Develop the exposed patterns using 25 % TMAH at 23 ºC for 30 seconds. Rinse in reverse osmosis (RO) water for 60 seconds in two separate beakers and then in isopropanol (IPA) solution for 15 seconds. Then blows dry with gaseous nitrogen.

For the dry-etch test, the DFB laser mask is designed as uniform grating structure. The SEM picture of mask after EBL and development is shown in Fig.3.3.2.

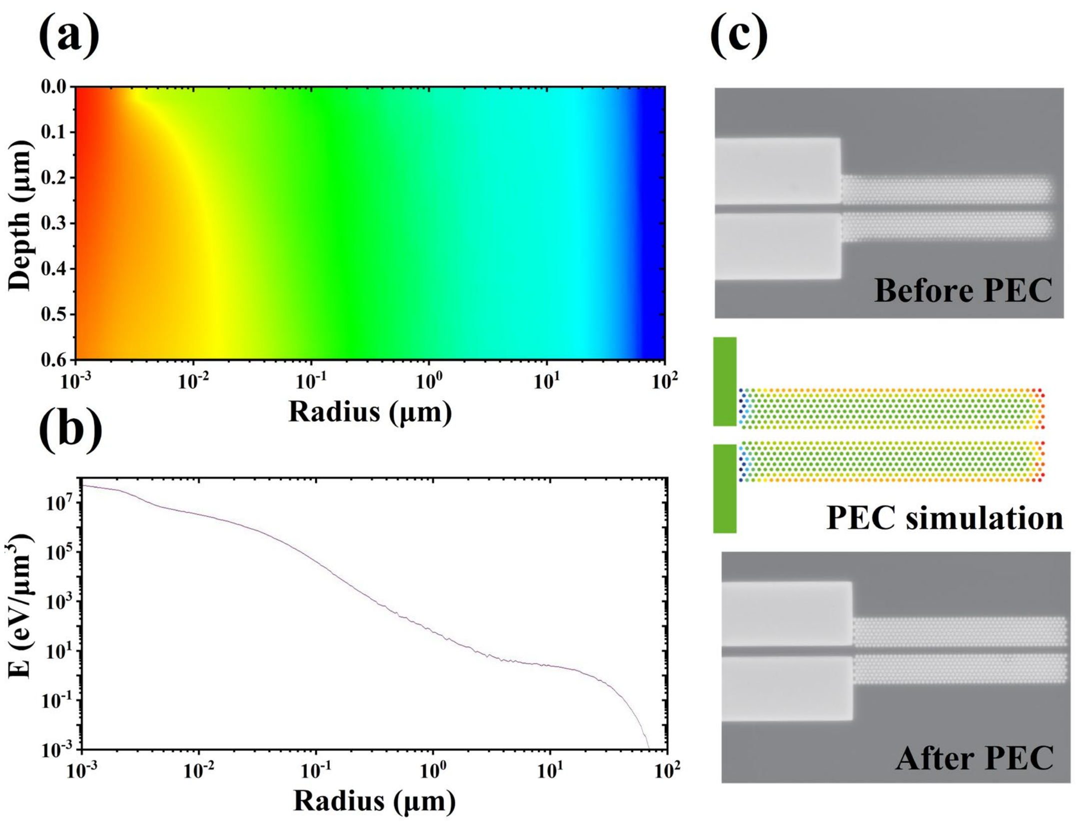

**Figure 3.3.1** (a) Calculated dose as the function of pattern size (defined as radius of exposure pattern) and HSQ resist layer depth. (b) Calculated Ebeam accelerating voltage as the function of pattern size. (c) Waveguide profile before (top right) and after (bottom right) PEC optimization, along with the corresponding PEC simulation (middle right).

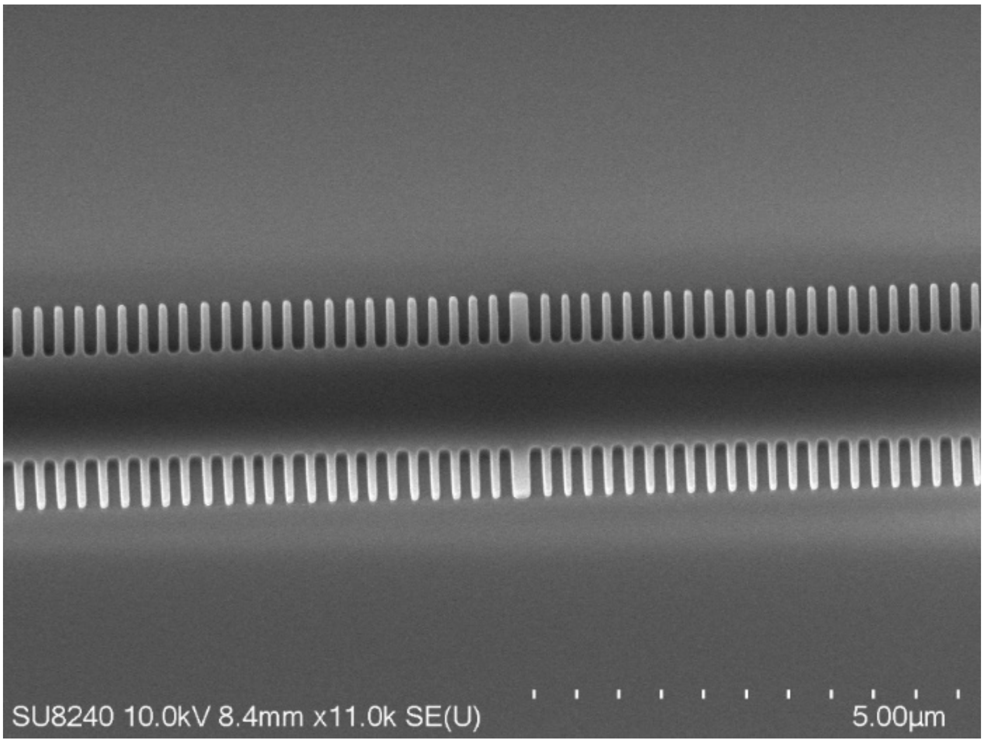

**Figure 3.3.2**SEM picture of the DFB grating HSQ mask.

### 3.3.2 Dry-etch fabrication optimization

The RIE-lag effect, which causes smaller trench openings to be etched slower than wider ones, is shown in Fig. 3.3.3(a). In the fabrication of sidewall DFB lasers, this effect directly impacts the etch depth inside the grating, leading to poor coupling efficiency. As shown in Fig. 3.3.3(b), the incomplete etching of the grating to the substrate can be observed in the cross-sectional view.

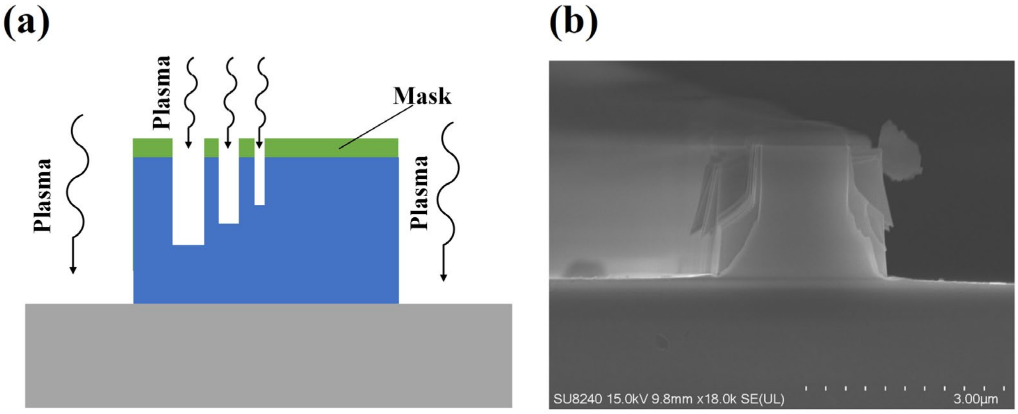

**Figure 3.3.3**(a) RIE-lag effect in dry etch, (b) cross-sectional view of SW grating with RIE-lag effect.

The etching process for InP/AlInGaAs utilized $Cl_2/CH_4/H_2$ gas in the Cobra (Cluster) system, with Ar added to optimize the sidewall grating's vertical profile. Six different etching recipes were tested, and the parameters and corresponding results are presented in Table 3.3.1 and Figure 3.3.4. Test 1 is the recipe with 10 sccm chlorine, resulting in a highly vertical etch profile but also a serious RIE-lag effect. This occurred due to the high plasma density, which was nonuniform inside and outside the grating recess, leading to a lower vertical etching rate inside the recess compared to the ridge waveguide. In Test 2, reducing the chlorine flow to 8 sccm decreased the vertical etching rate, allowing gas to enter the grating recess more fully and releasing the RIE-lag effect. However, increasing the etching time to 600 s caused ions to diffuse from the recess to the grating, resulting in a horizontally etched and warped sidewall.

Test 4 was conducted at a higher temperature of 80°C, but it did not improve verticality or reduce the RIE-lag effect compared to Test 3. In Test 5, increasing the argon flow rate to 20 sccm resulted in a dramatically vertical sidewall, but the recess was insufficiently etched. Therefore, Test 5 was divided into two steps, with the first step using 20 sccm of argon to maintain good etching verticality, followed by removing the argon and reducing the chlorine flow to 6 sccm to reduce the RIE-lag effect. This approach improved both the RIE-lag effect and verticality.

**Table 3.3.1** The recipes of dry etch test.

| Sample | Recipe | Etch time | Result |
|---|---|---|---|
| 1 | $Cl_2/CH_4/H_2/Ar$ = 10/10/15/10 sccm, ICP/Platen = 750/100 W, 5 mTorr, 60°C, Backside He = 0 Torr | 500 s | Figure. 3.3.4 (a) |
| 2 | $Cl_2/CH_4/H_2/Ar$ = 8/10/15/10 sccm, ICP/Platen = 750/100 W, 5 mTorr, 60°C, Backside He = 0 Torr | 600 s | Figure. 3.3.4 (b) |
| 3 | $Cl_2/CH_4/H_2/Ar$ = 8/10/15/10 sccm, ICP/Platen = 750/100 W, 5 mTorr, 80°C, Backside He = 0 Torr | 550 s | Figure. 3.3.4 (c) |
| 4 | $Cl_2/CH_4/H_2/Ar$ = 8/10/15/20 sccm, ICP/Platen = 750/100 W, 5 mTorr, 60°C, Backside He = 0 Torr | 550 s | Figure. 3.3.4 (d) |
| 5 | $Cl_2/CH_4/H_2/Ar$ = 8/10/15/20 sccm, ICP/Platen = 750/100 W, 5 mTorr, 60°C, Backside He = 0 Torr | 400 s | Figure. 3.3.4 (e) |
|  | $Cl_2/CH_4/H_2$ = 6/10/15 sccm, ICP/Platen = 750/100 W, 5 mTorr, 60°C, Backside He = 0 Torr | 100 s |  |
| 6 | $Cl_2/CH_4/H_2/Ar$ = 8/10/15/20 sccm, ICP/Platen = 750/100 W, 5 mTorr, 60°C, Backside He = 0 Torr | 400 s | Figure. 3.3.4 (f) |
|  | $Cl_2/CH_4/H_2$ = 5/10/15 sccm, ICP/Platen = 750/100 W, 5 mTorr, 60°C, Backside He = 0 Torr | 100 s |  |

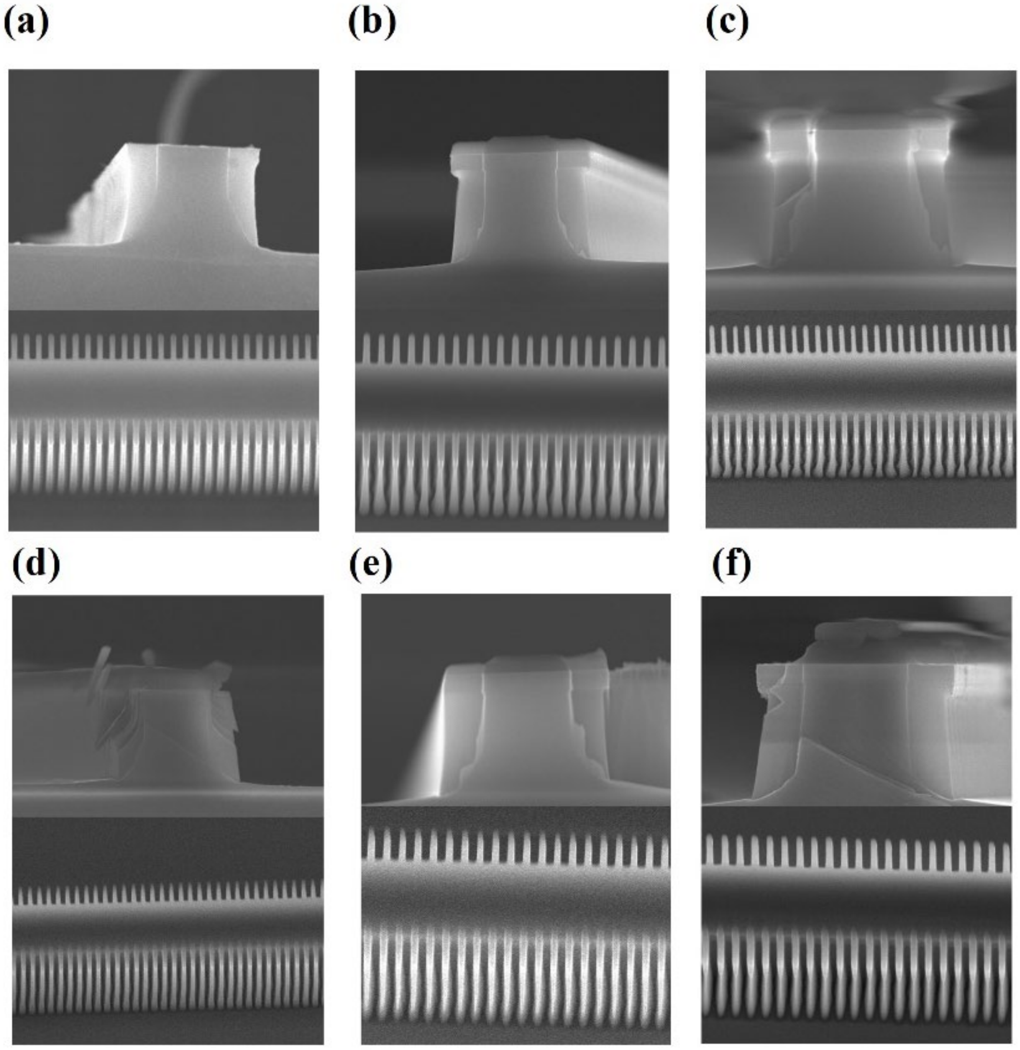

**Figure 3.3.4** Dry etch test results using the recipes from Table 3.3.1.

## 3.4 Planarization and open window

After the ridge waveguide etch, dielectric films were deposited on the sample, and contact windows were opened on the top of the ridge waveguides through the etching of the dielectric films to electrically isolate the ridge waveguides. The insulator used for the dielectric films was silicon dioxide ($SiO_2$), which was deposited through a Plasma-Enhanced Chemical Vapor Deposition (PECVD) process. This process is based on chemical reactions in a plasma of reacting gases and is known for producing high-quality thin dielectric films. The first layer is 200 nm $SiO_2$ deposited at 300 °C, followed by a layer of approximately 400 nm of HSQ. After spinning, the sample was baked in a 180°C oven for two hours to solidify the HSQ. A final layer of 100 nm of PECVD $SiO_2$ was deposited to ensure good insulation performance, resulting in a total $SiO_2$ thickness of approximately 700 nm. Due to the high-mesa structure of the ridge waveguide, the $SiO_2$ films on top of the ridge waveguides were thinner than 700 nm.

For the open window process, an Oxford Instrument RIE80+ was utilized to etch the $SiO_2$ films, with 2.4 µm PMMA (15% 2010) serving as the mask during this step. The electron beams only exposed the top of the ridge waveguides, and the PMMA was removed after development. The width of the window is 1.3 µm which is smaller than the ridge waveguide, ensuring that the electric currents were only injected into the top area of the ridge waveguides. The $SiO_2$ RIE dry etch was performed using Fluoroform ($CHF_3$) with a gas flow rate of 25 sccmPMC and argon (Ar) with a gas flow rate of 15 sccm. The chamber pressure was 30 mTorr. The RF power was set at 150 W, and the working temperature was maintained at 20°C. This etching recipe resulted in an etch rate of approximately 23 nm/min. The step of the open window is shown in Figure 3.4.2.

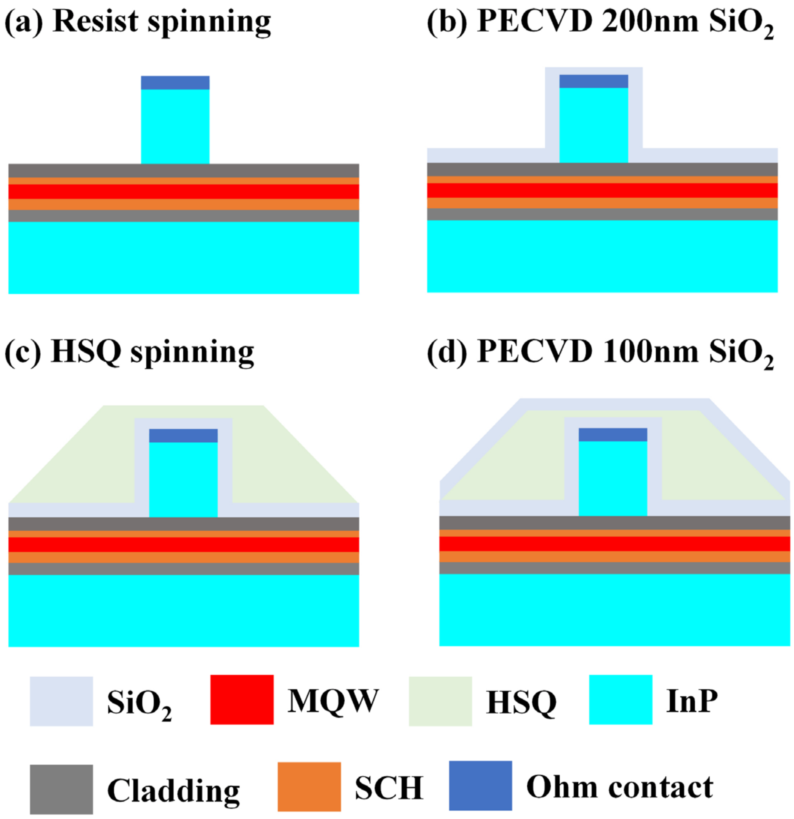

**Figure 3.4.1** The process flow of planarization using HSQ.

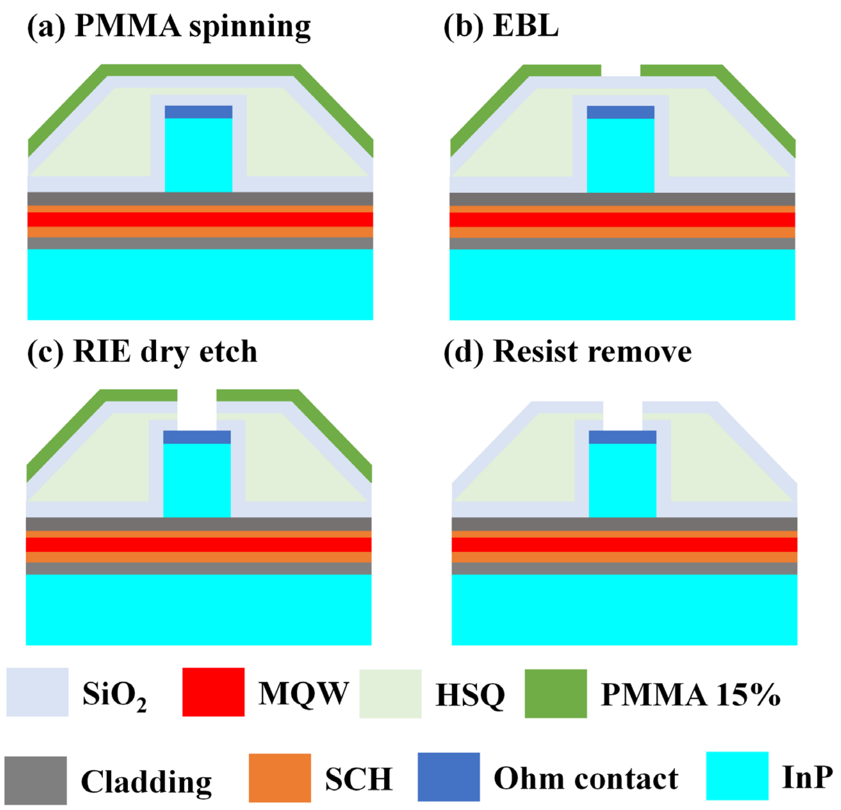

**Figure 3.4.2** The process flow for opening metal P-contact window.

# 3.5 Metallization for p-contact

Following the contact window, the p-contact electrodes were grown on top of the ridge waveguides by a metal deposition process as shown in Fig.3.5.1. This process utilized a 2.4 μm PMMA (15% of 2010) for lift-off. Before the metal deposition, the sample was cleaned in RF Barrel Asher by oxygen at 110 W for 2 minutes, this step is to clean the remaining resist inside the window. Then the sample was rinsed in 1:5 hydrochloric acid/water ($HCl/H_2O$) for 30 seconds to deoxidize and cleaned in RO water for 30 seconds. The p-contact metal layers, consisting of Titanium/Platinum/Gold (Ti/Pt/Au), were deposited at thicknesses of 33/33/240 nm, respectively. Titanium was employed as an adhesion layer due to its reactivity and ease of oxidation, while Platinum was used to prevent gold diffusion into the semiconductor layer. Given that the conductivity of Titanium is inferior to that of Gold, a final layer of 240 nm of Gold was deposited to ensure adequate electrical conductivity. After the metallization, the sample was dipped into Acetone (water bath at 50 °C) for about 15 minutes to remove the PMMA and the overlaying metal layer.

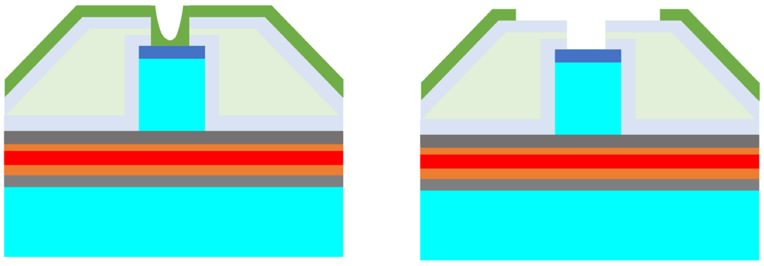
(a) PMMA spinning (b) EBL/O$_2$ clean/deoxidize

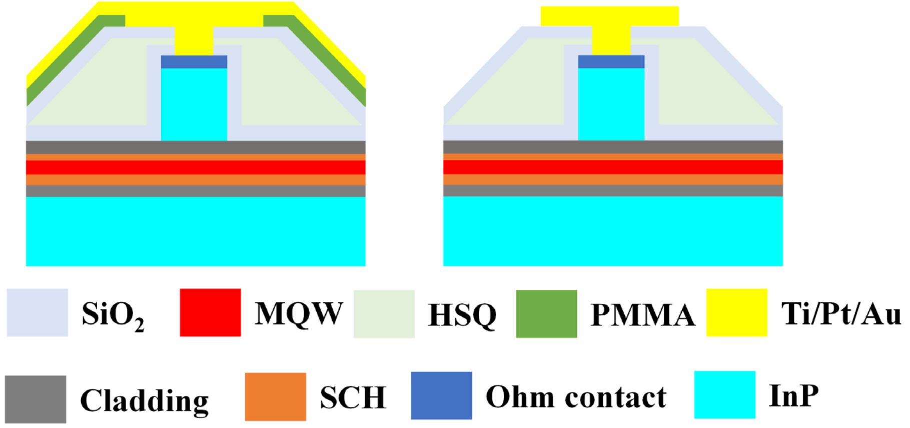
(c) Deposit Ti/Pt/Au (d) Lift off

**Figure 3.5.1** The process flow of p-contact metallization.

# 3.6 Thinning and n-contact metallization

In order to enhance cleaving and reduce resistance, the n-type substrate side of the sample was thinned to roughly 180 µm. This was achieved through a series of steps: initially, the glass cover-strip was spin coated with photoresist S1818 at a rate of 2000 rpm for 5 seconds. The p-side of the sample was placed face-down onto the glass cover-strip and subjected to an oven temperature of 90 ºC for 60 minutes, to ensure proper adhesion of the resist material with the glass cover-strip. Then the glass cover-strip was mounted to a metal chuck using wax and the sample was thinned to 180 µm thick with aluminum powder (9 µm/ 3 µm granules) with water mix. After unloading the glass cover-strip from the chuck, the sample and glass cover-strip were cleaned by RO water and IPA for metallization. The n-contact metal layers of Au/Ge/Au/Ni/Au of thicknesses 14/14/14/11/240 nm were evaporated at the back of the samples. Then all of them were rinsed in acetone to dissolve the S1818, and the sample separated from the glass cover-strip.

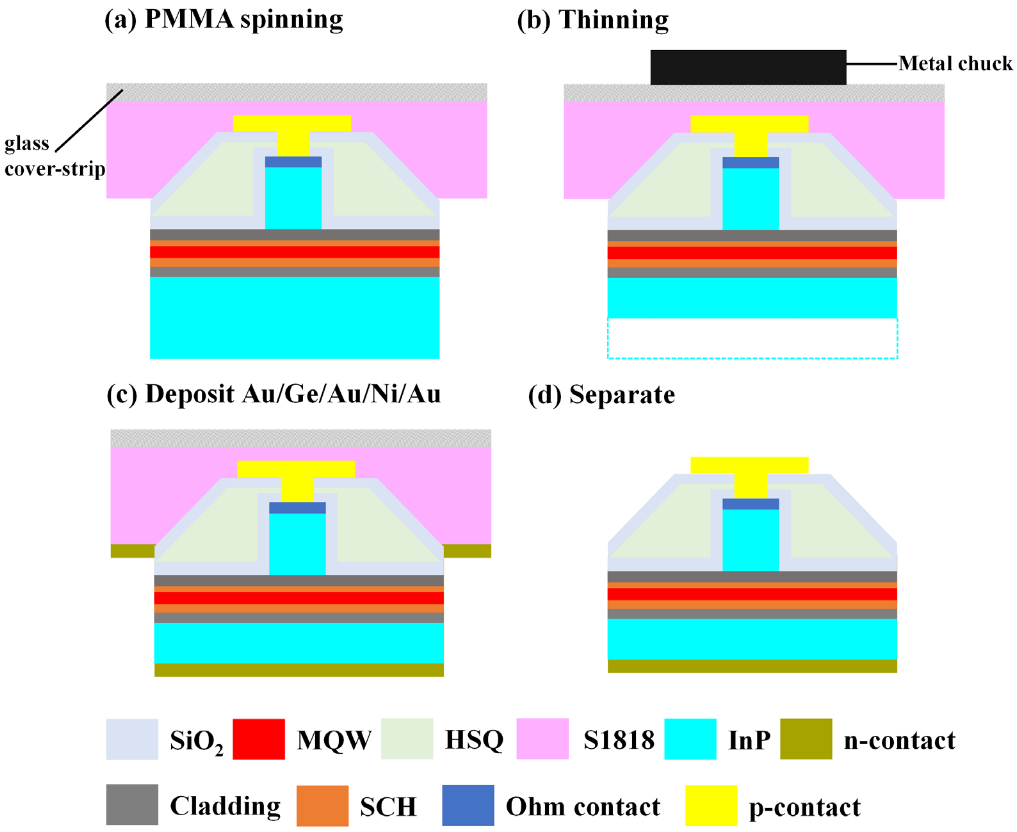

**Figure 3.6.1** The process flow of thinning and n-contact metallization.

# 3.7 Rapid thermal annealing

Within the semiconductor industry, rapid thermal annealing (RTA) represents a crucial process step utilized for the activation of dopants and the interfacial reaction of metal contacts. This involves the rapid heating of materials to high temperatures, followed by cooling for both p-contact and n-contact. The annealing condition was 380 °C for 60 seconds, as shown in Fig. 3.7.1. The measured annealing temperature was found to be close to the set points.

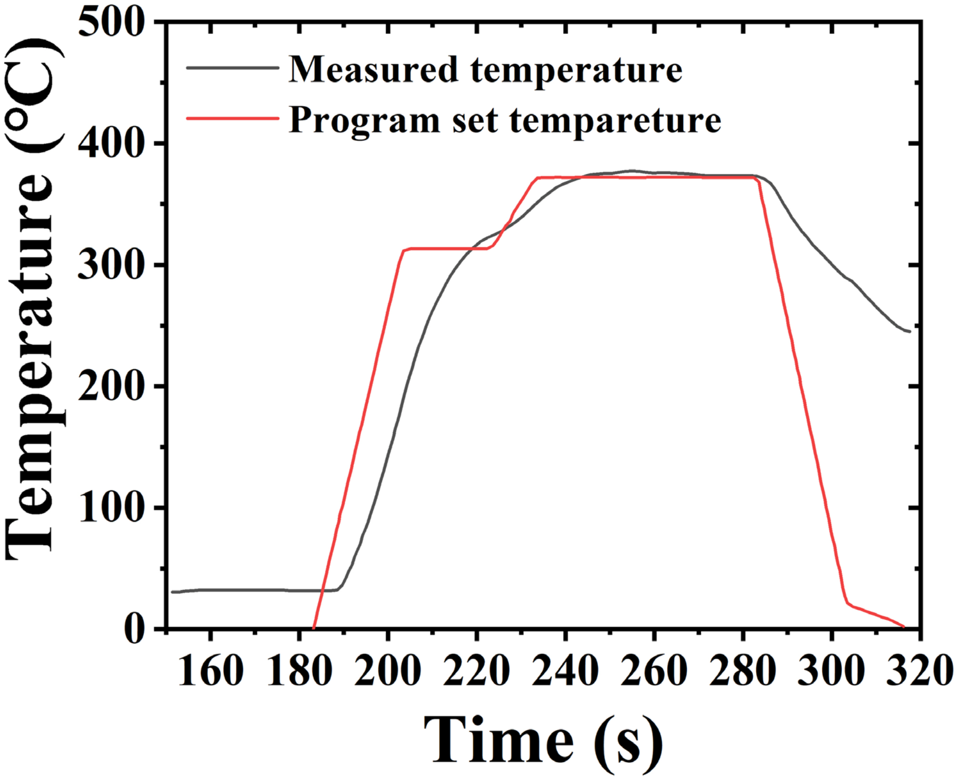

**Figure 3.7.1** Annealing temperature as a function of time.

# References of this chapter

[1] N. Furuhata, H. Miyamoto, A. Okamoto, and K. J. J. o. a. p. Ohata, "Chemical dry etching of GaAs and InP by Cl2 using a new ultrahigh-vacuum dry-etching molecular-beam-epitaxy system," vol. 65, no. 1, pp. 168-171, 1989.

[2] J. Lin *et al.*, "Smooth and vertical-sidewall InP etching using Cl 2/N 2 inductively coupled plasma," vol. 22, no. 2, pp. 510-512, 2004.

[3] M. Bösch, L. Coldren, and E. J. A. P. L. Good, "Reactive ion beam etching of InP with Cl2," vol. 38, no. 4, pp. 264-266, 1981.

[4] T. Hayes *et al.*, "Reactive ion etching of InP using CH4/H2 mixtures: Mechanisms of etching and anisotropy," vol. 7, no. 5, pp. 1130-1140, 1989.

# Chapter 4 Half-ridge PMCs

## 4.1 Design and optimization

The epitaxial layer profile of the PMC device is based on a purchased conventional 1.55 μm AlGaInAs/InP LD [1] grown on a sulphur-doped InP substrate via metal–organic vapor phase epitaxy (MOVPE) in a single step. The epitaxial structure includes various layers, as shown in Figure 4.1.1, starting with an 800 nm thick n-InP buffer, a 10 nm n-type graded composition AlGaInAs layer, a 60 nm n-AlGaInAs cladding layer, and a 60 nm thick bottom graded-index separate confinement heterostructure (GRINSCH) AlGaInAs layer with an Al composition that varies from 0.423 to 0.338. The MQW structure is composed of five 6 nm thick compressively strained (+1.2%) AlGaInAs QWs and six 10 nm thick tensile-strained (0.3%) AlGaInAs barriers. Above the active layers, there is a 60 nm thick top GRINSCH layer, a 60 nm thick p-AlGaInAs cladding layer, 50 nm of p-InP, a 20 nm thick $In_{0.85}Ga_{0.15}As_{0.33}P_{0.67}$ 1.1Q wet etch stop layer (i.e., with a photoluminescence wavelength of 1.1 μm at room temperature), a 1600 nm thick p-InP layer, a 50 nm thick $p$-$In_{0.71}GaAs_{0.62}P$ (1.3Q) layer, and a 200 nm thick p+ InGaAs contact layer.

The polarization state in the MQW laser is influenced by the strain present in the quantum well. Specifically, the compressive strain QW results in a larger conduction band discontinuity and a smaller valence band discontinuity. In the case of a MQW structure, the optical matrix element at the band edge can be expressed as [2]:

$$M = p_{cv} M_0 \qquad \textbf{(4.1.1)}$$

Where $M_0$ is the average matrix of the Bloch state, $p_{cv}$ is the polarization vector is parallel to the QW layers, and the polarization factors of the TE mode and TM mode are $p_{cv}^{TE}$ = 1.5 (HH), 0.5 (LH), $p_{cv}^{TM}$ = 0 (HH), 2 (LH) for the compressively strained

MQW. HH is the heavy hole band, and LH is the light hole band. For the compressive strain QW laser, the photon mostly excites from the HH band which means that there is only TE-polarized laser operation for the compressive strained AlGaInAs laser.

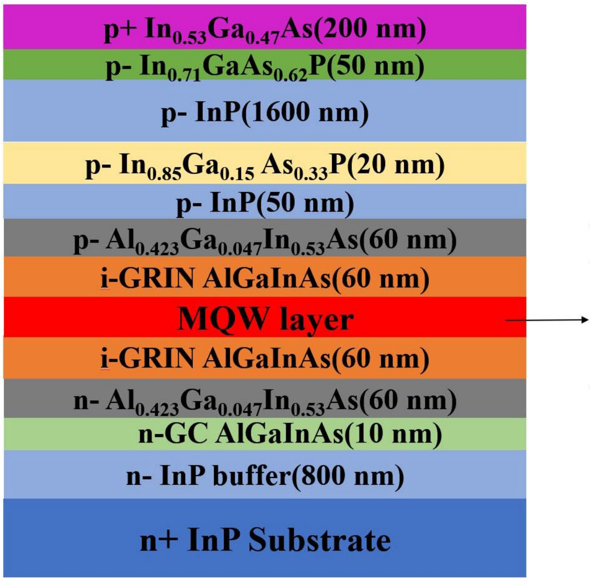

| MQW | Well | Barrier |
|---|---|---|
| Material | 5 ×AlGaInAs | 6 ×AlGaInAs |
| Thickness | 6 nm | 10 nm |
| Strain | +1.2% | -0.3% |

**Figure 4.1.1** The epitaxial layer structure for the half-ridge PMC.

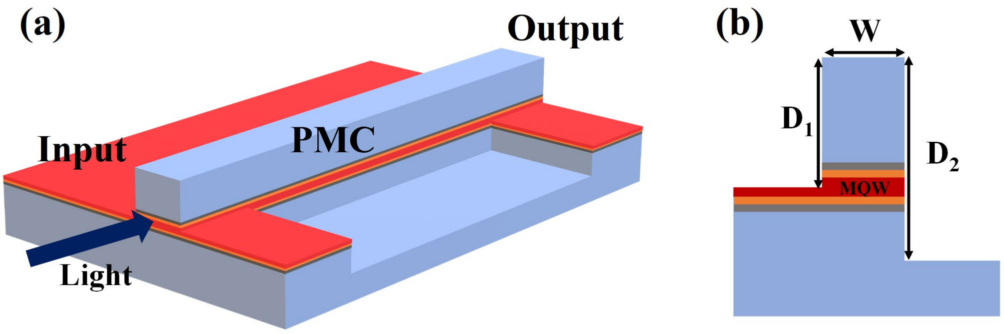

**Figure 4.1.2** Schematic of half-ridge PMCs with AlGaInAs MQW layer.

Figure 4.1.2 shows a schematic of the PMC, which is composed of an input section, a PMC section, and an output section. The input and output sections consist of symmetric, shallow-etched ridge waveguides. The PMC section is based on a half-ridge design, where a ridge waveguide is etched to different depths on each side. As TE-polarized light propagates into the asymmetric waveguide, it excites two eigenmodes that interfere constructively to convert the polarization state to TM-polarization after propagating through a half-beat length $L_\pi$, which is given as:

$$L_\pi = \frac{\pi}{\beta_1 - \beta_2} \tag{4.1.2}$$

where $\beta_1$ *and* $\beta_2$ are the propagation constants of the two fundamental modes, i.e., the TE$_0$ and TM$_0$ modes. The eigenmodes in the PMC waveguide are rotated by 45° with respect to the modes in the input waveguide. After propagating a distance $L_\pi$, the input TE mode rotated by 90° generating a pure TM-polarized output. The design requires optimizing the ridge waveguide shallow-etched depth ($D_1$) and width ($W$). the PCE is calculated as in [3]

$$PCE = \sin^2(2\varphi)\sin^2\left(\pi\frac{L_{PMC}}{2L_\pi}\right) \tag{4.1.3}$$

where $\varphi$ is the rotated angle of the eigenmodes in the PMC waveguide, and $L_{PMC}$ is the length of PMC. In this work $L_{PMC}$ is equal to the half-beat length $L_\pi$. It is noted that deep-etched depth ($D_2$) has almost no effect on the eigenmode profiles when its value is large enough (>3.55 μm).

To ensure that the PMC waveguide supports only the fundamental TE$_0$ and TM$_0$ modes, the effective modal index ($N_{eff}$) values for the first four modes (TE$_0$, TM$_0$, TE$_1$, TM$_1$) were calculated using the FEM solver, and are illustrated in Figure 4.1.3. a range of $W$ can be identified in which only the two fundamental modes (TE$_0$ and TM$_0$) can propagate in the PMC. This range of $W$ is between 1.45 μm and 3.10 μm.

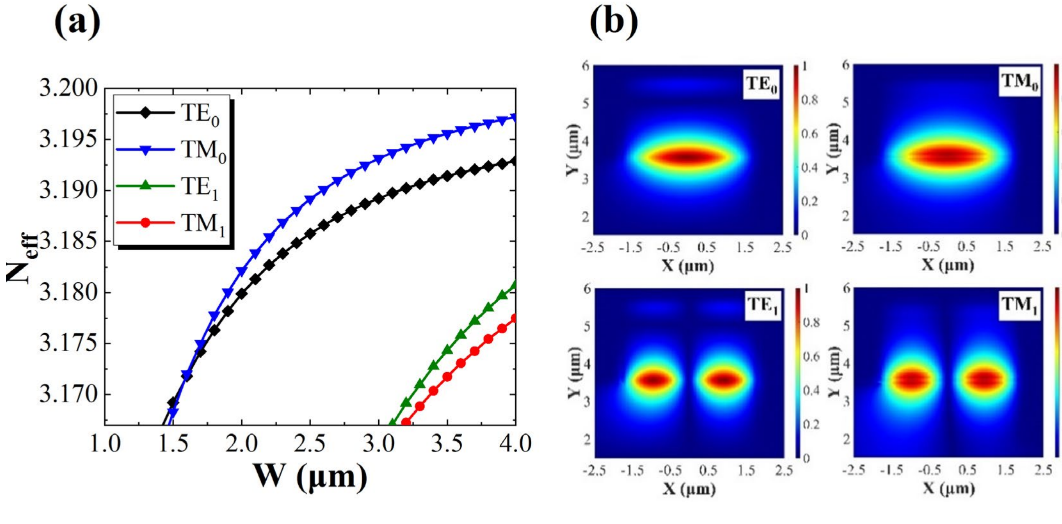

**Figure 4.1.3** (a) Simulated waveguide effective refractive index of TE$_0$, TM$_0$, TE$_1$, TM$_1$ modes as a function of the ridge waveguide width $W$ with $D_1$ = 2.16 μm and $D_2$ = 3.64 μm. (b) Electric field profiles of TE$_0$ and TM$_0$, TE$_1$ and TM$_1$ modes ($W$ = 3.50 μm).

## 4.2 Simulation and result

After identifying the range of waveguide widths (*W*) that support only the fundamental $TE_0$ and $TM_0$ modes, the optimization process using the EigenMode Expansion (EME) solver was performed by sweeping through a broad range of values. Specifically, waveguide widths (*W*) between 1.45 µm to 1.70 µm and shallow etched depths ($D_1$) ranging from 2.04 µm to 2.24 µm were explored. The optimization program obtained 1000 simulation data points by dividing the initial range of *W* into 50 grids and $D_1$ into 40 grids. From these points, we randomly selected 200 to calculate their maximum PCE. We assumed that the input source was 100% TE-polarized light. Figure 4.2.1 (a) shows the 2D plot of the maximum PCE as a function of *W* and $D_1$.

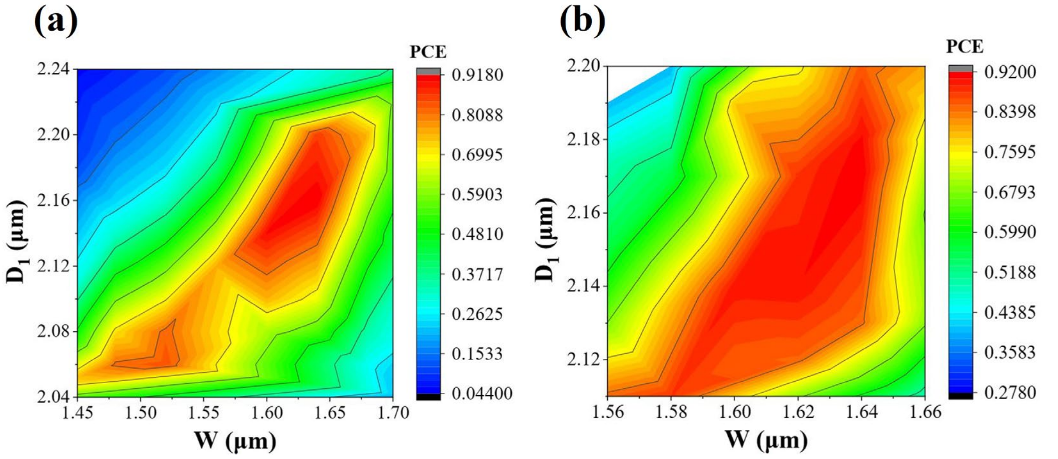

**Figure 4.2.1** Maximum TE–TM PCE as a function of waveguide width (*W*) and shallow etched depth ($D_1$) from (a) broad-range optimization and (b) narrow-range optimization.

Data points with a PCE exceeding 70% were found to cluster around certain value ranges, specifically, $D_1$ ranging from 2.10 µm to 2.20 µm, and *W* ranging from 1.56 µm to 1.66 µm. To obtain a more focused analysis, additional simulations were conducted on a narrower range of these variables, as shown in Figure 4.2.1 (b). Based on the calculations described above, three PMC profiles with a high PCE and relatively short $L_\pi$ were identified. Table 4.2.1 shows the waveguide parameters and the PCE. The maximum TE-TM PCE achieved was 94% for profile 3. As a waveguide with a longer $L_\pi$ would exhibit increased absorption and make the device footprint larger, profile 2 represents a good balance between PCE and $L_\pi$. Figure 4.2.2 displays the electric field profiles of the first two eigenmodes with $TE_0$ and $TM_0$ polarizations in a PMC designed with profile 2. These modes are confined by the AlGaInAs MQW core, and the fractions of TE and TM polarization are almost equal, confirming that the polarization of the modes in the PMC is tilted by approximately 45° with respect to the mode in the input section, which is fully polarized with TE polarization.

Figure 4.2.3 (a) displays the variation in the maximum PCE and the $L_\pi$ as $D_1$ is changed in 5 nm increments. When $W$ was set to 1.62 µm, the highest PCE of 92% was achieved at $D_1$ = 2.15 µm, with $L_\pi$ measuring approximately 1250 µm. Alternatively, with $W$ set to 1.66 µm, the maximum PCE improved to 94% for $D_1$ = 2.25 µm. However, this resulted in a longer $L_\pi$, exceeding 1800 µm as presented in Figure 4.2.3 (b).

**Table 4.2.1** Three profiles of waveguide parameters.

| **Profile** | $W$ | $D_1$ | $D_2$ | $L_\pi$ | **PCE** |
|---|---|---|---|---|---|
| 1 | 1.58 µm | 2.10 µm | 3.64 µm | 970 µm | 88.0 % |
| 2 | 1.62 µm | 2.16 µm | 3.64 µm | 1250 µm | 92.5% |
| 3 | 1.66 µm | 2.24 µm | 3.64 µm | 1870 µm | 94.0% |

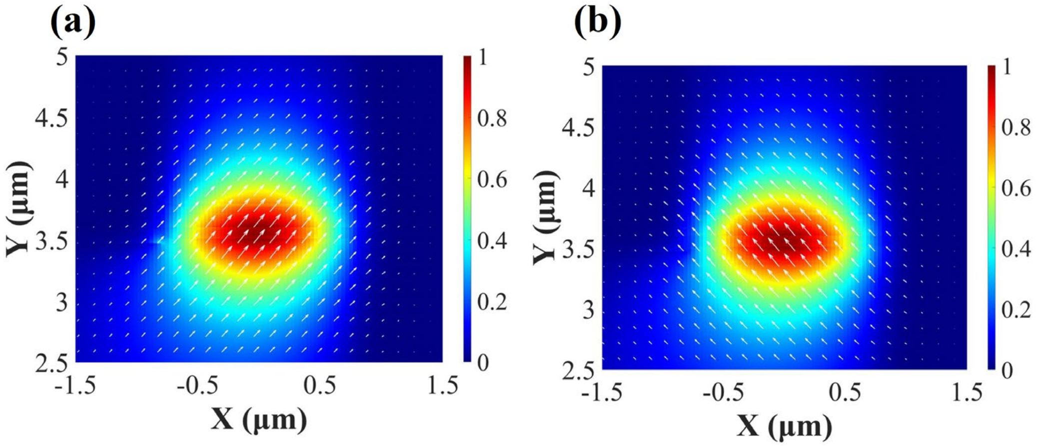

**Figure 4.2.2** Electric field profiles of (a) $TE_0$ and (b) $TM_0$ eigenmodes for $D_1$ = 2.16 µm, $D_2$ = 3.64 µm, $W$ = 1.62 µm.

Figure 4.2.4 presents the variation of maximum PCE and $L_\pi$ as a function of $W$ in 10 nm steps. With $D_1$ fixed at 2.16 µm, the maximum PCE was slightly above 90% in the range of 1.60 µm ≤ $W$ ≤ 1.64 µm. When $D_1$ was increased to 2.18 µm, the maximum PCE changed by less than 5% in the same range of $W$, but $L_\pi$ increased to approximately 1500 µm. However, for $D_1$ = 2.12 µm, $L_\pi$ was reduced to approximately 1000 µm, but the maximum PCE was less than 90% over the entire range of $W$. Therefore, to obtain a high PCE with a relatively short device length, the optimal values of $W$, $D_1$, and $L$

were determined to be 1.62 μm, 2.16 μm, and 1250 μm, respectively. Figure 4.2.5 illustrates the sensitivity of PCE to variations in *W* and $D_1$, with *L* fixed at 1250 μm. To achieve a PCE of at least 85%, which represents a deviation of <8% from the maximum value of 92%, the optimal ranges for *W* and $D_1$ were found to be between 1.60 μm and 1.65 μm, and between 2.13 μm and 2.18 μm, respectively.

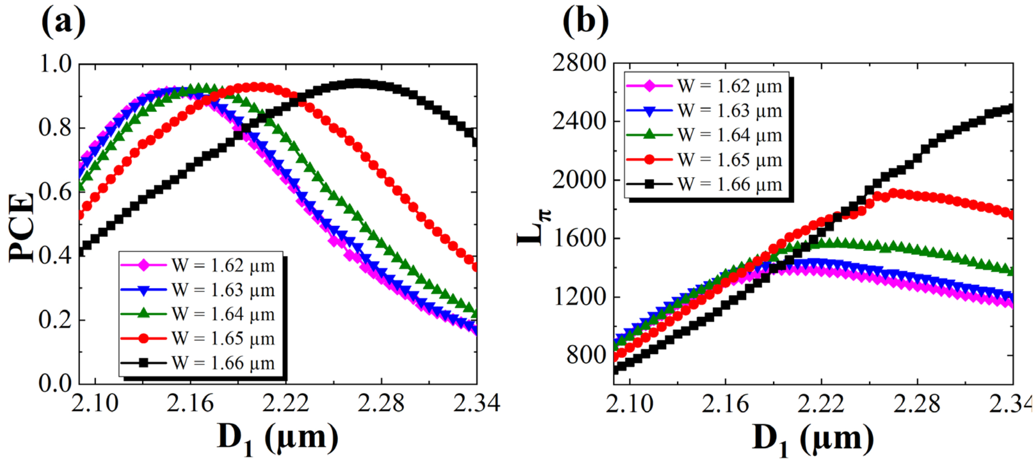

**Figure 4.2.3**(a)Maximum TE–TM PCE and(b) half-beat length $L_\pi$ as a function of waveguide width (*W*) and shallow etched depth ($D_1$).

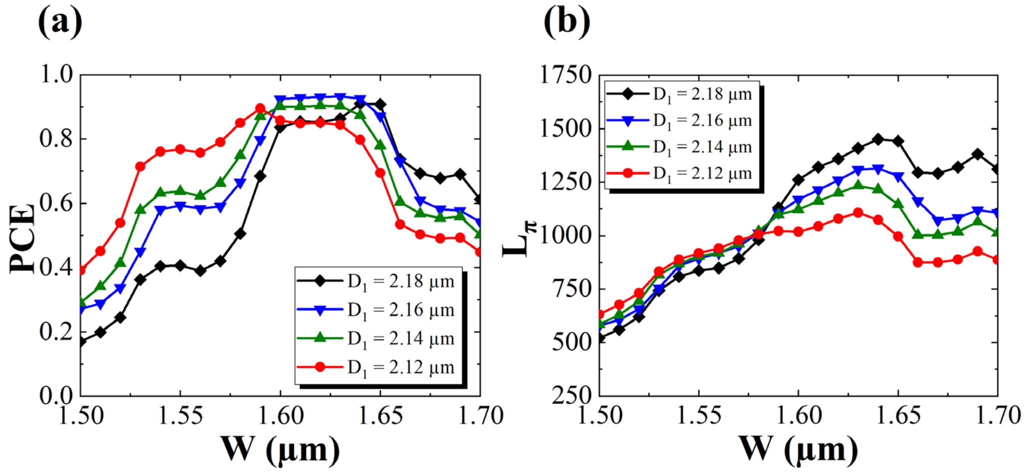

**Figure 4.2.4** (a) Maximum PCE and (b) half-beat length, $L_\pi$, as a function of the waveguide width *W*.

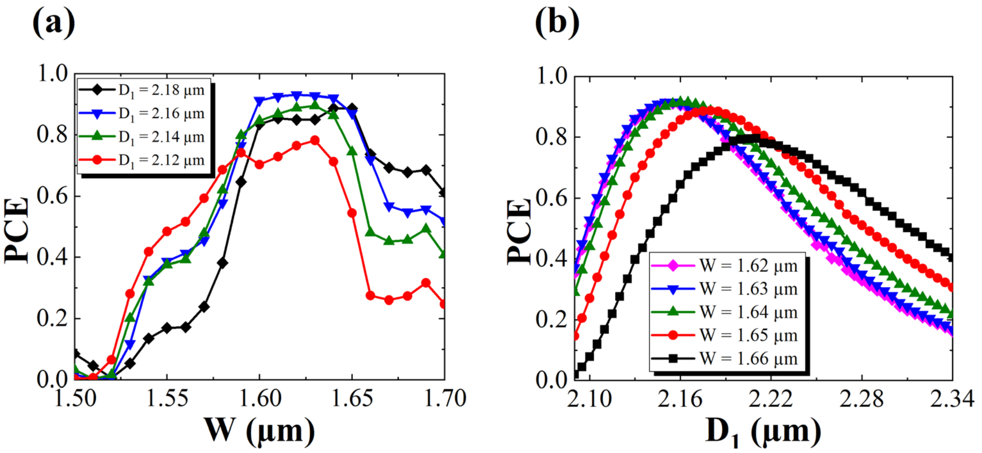

**Figure 4.2.5** Maximum PCE with respect to (a) the waveguide width *W* and (b) the shallow etched depth $D_1$ for a PMC length of 1250 μm.

The limited PCE and long length of the PMC discussed in this work are primarily because the epitaxial layer structure is optimized for the laser diode. In the half-ridge waveguide PMC, the two fundamental eigenmode profiles are largely determined by the structure and refractive index of the core layer, defined by *W* and $D_1$. PMC with a thicker core layer has a larger optimization range of *W* and $D_1$. T. Tanemura et al. achieved a 16.6 dB *ER* with a 500 nm thick core layer half-ridge waveguide PMC by using a waveguide width of 1 μm and a core layer shallow etched thickness of 200 nm. [4]. However, in our design, the thickness of the core MQW layer for the laser diode is only 90 nm, which results in three issues. Firstly, the value of *W* cannot be lower than 1.5 μm, otherwise the two fundamental eigenmodes cannot exist, as shown in Fig. 4.1.3. This reduces the optimization ranges of *W* and $D_1$ to adjust the maximum PCE. Secondly, the effective refractive indexes of the $TE_0$ and $TM_0$ modes are quite close, resulting in a relatively long $L_\pi$ for standard epitaxial structures used for lasers. The thin waveguide core and low optical confinement reduce the PCE and increase its sensitivity to wavelength variations and fabrication tolerances. To improve the PCE and $L_\pi$ values, the thickness of the waveguide core could be optimized to achieve a larger propagation constant difference between $TE_0$ and $TM_0$ to reduce $L_\pi$ and a higher optical confinement to reduce sensitivity to input wavelength and PMC dimensions. As a result, another step height ridge PMC, which reduces the $L_\pi$ fabrication tolerances and achieves larger PCE, is designed and discussed in the following chapter 6.

# References of this chapter

[1] L. Hou *et al.*, "Subpicosecond Pulse Generation at Quasi-40-GHz Using a Passively Mode-Locked AlGaInAs–InP 1.55-µm Strained Quantum-Well Laser," *IEEE Photonics Technology Letters,* vol. 21, no. 23, pp. 1731-1733, 2009.

[2] M. Sugawara, T. Fujii, S. Yamazaki, and K. Nakajima, "Theoretical and experimental study of the optical-absorption spectrum of exciton resonance in In 0.53 Ga 0.47 As/InP quantum wells," *Physical Review B,* vol. 42, no. 15, p. 9587, 1990.

[3] M. Zaitsu, T. Tanemura, and Y. Nakano, "Numerical study on fabrication tolerance of half-ridge InP polarization converters," *IEICE Transactions on Electronics,* vol. 97, no. 7, pp. 731-735, 2014.

[4] T. Tanemura, T. Amemiya, K. Takeda, A. Higo, and Y. Nakano, "Simple and compact InP polarization converter for polarization-multiplexed photonic integrated circuits," in *2009 IEEE LEOS Annual Meeting Conference Proceedings*, 2009, pp. 436-437: IEEE.

# Chapter 5 Stepped height PMC integrated DFB laser

## 5.1 Epitaxial layer structure design

The epitaxial layer structure of the stepped height ridge PMC closely resembles the half-ridge waveguide depicted in Figure 5.1.1. The primary distinction lies in the inclusion of a 300 nm thick InGaAsP passive waveguide layer with a PL wavelength of 1.25 µm(1.25Q), also referred to as a far-field reduction layer (FRL) [1]) is embedded below the MQW layer to increase the difference between the propagation constants of the two fundamental modes of the PMC so reducing the $L_\pi$ and significantly improving the PCE.

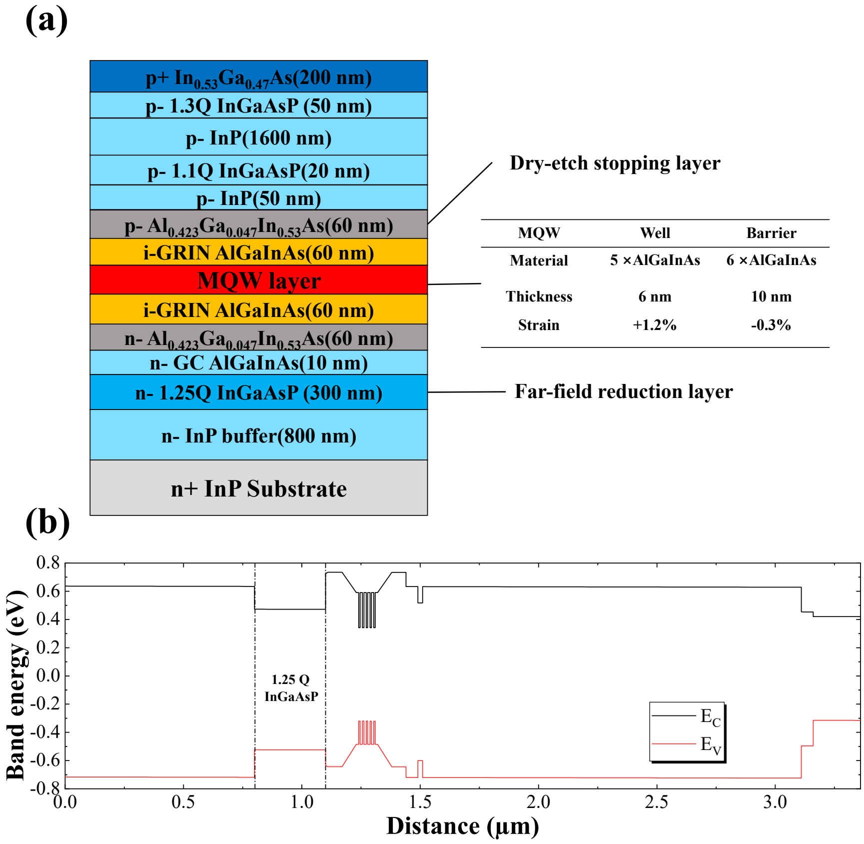

**Figure 5.1.1** (a) The epitaxial layer structure of the PMC; (b) band diagram of the LD-PMC device structure.

In order to reduce the absorption loss of the PMC, quantum well intermixing (QWI) is considered and compared with the as-grown MQW. To calculate the optical properties of the QWI-processed material, Fick's law of diffusion is utilized to model the QW profile [2] and its PL spectrum during intermixing. In the model, the degree of intermixing is represented by the diffusion length on the group III substance, $C$ (z, $L_D$), as shown in

$$C(z,L_D)=(C_1-C_2)\left[1-\frac{1}{2}erf\left(\frac{z-\frac{L_W}{2}}{2\sqrt{L_D}}\right)+\frac{1}{2}erf\left(\frac{z+\frac{L_W}{2}}{2\sqrt{L_D}}\right)\right] \tag{4.2.1}$$

where $C_1$ and $C_2$ are the initial atomic mole fractions for QW and QB materials respectively, z is the quantization direction along the growth axis (QW centered at z = 0), and "erf" denotes the error function, $L_W$ is the quantum well width, and $L_D$ is the diffusion length. By fitting the experimental and calculated bandgap shifts, an appropriate value of $L_D$ is chosen. Figure 5.1.2 presents the calculated refractive index and Al fraction profiles for the as-grown structure and the intermixed material, where the QW bandgap was blue-shifted by 100 nm, corresponding to an Al atom diffusion length of 1.53 nm. The refractive index curve at the interfaces between the intermixed wells and barriers has a smooth transition, rather than a stepped one. Notably, the refractive index profile of the intermixed quantum well exhibits two spikes, which is due to the effect of resonance absorption where the photon energy is equal to the bandgap of materials, and the partial elimination of birefringence associated with the MQW. The refractive index of each epitaxial layer is derived from the Adachi model [3, 4], which was developed for energies close to the bandgap. Table 5.1.1 presents the critical characteristics of the MQW before and after QWI. The detailed process of QWI can be referred to [14].

**Table 5.1.1** Critical as-grown MQW structural characteristics and after 100 nm QWI bandgap widening.

| | PL wavelength | Al fraction | Refractive Index | Diffusion Length |
|---|---|---|---|---|
| As grown | 1530 nm | 0.070 (QW)<br>0.224 (QB) | 3.579 (QW)<br>3.356 (QB) | |
| After QWI | 1430 nm | 0.166(average) | 3.4162(average) | 1.53 nm |

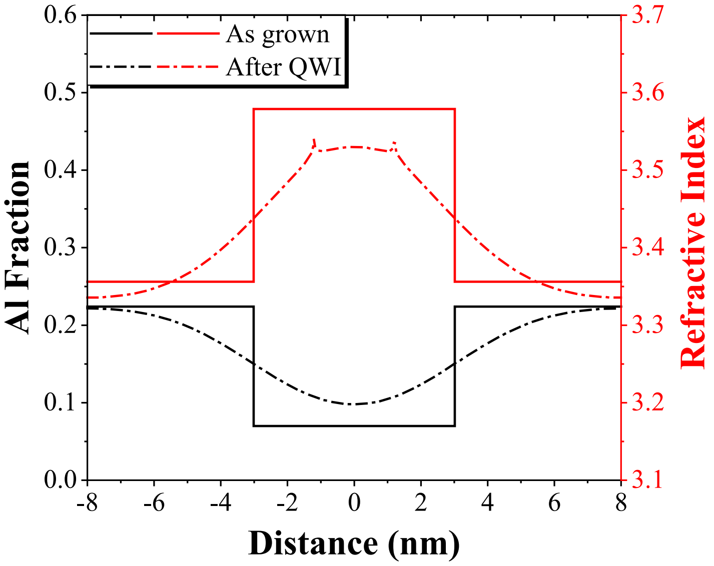

**Figure 5.1.2** Al fraction and reflective index distribution at 1550 nm wavelength through one MQW period for as-growth and after QWI by 100 nm blueshift.

This wafer can also serve as the foundation for a side wall grating laser, with a grating period of 238 nm designed for a 1550 nm Bragg wavelength. Figure 5.1.3 shows the dependence of coupling coefficient *κ* on the grating recess depth *d* for a ridge waveguide height at 1.92 μm, with laser ridge waveguide widths $W_L$ = 2.5, 2.0 and 1.5 μm. The result shows that for $d$ = 0.6 μm and $W_L$ =2.5 μm, the coupling coefficient κ can reach 90/cm. This value is 10/cm higher than that obtained without the 300-nm 1.25Q InGaAsP layer, which is enough for the 600 μm long sidewall grating DFB laser [5].

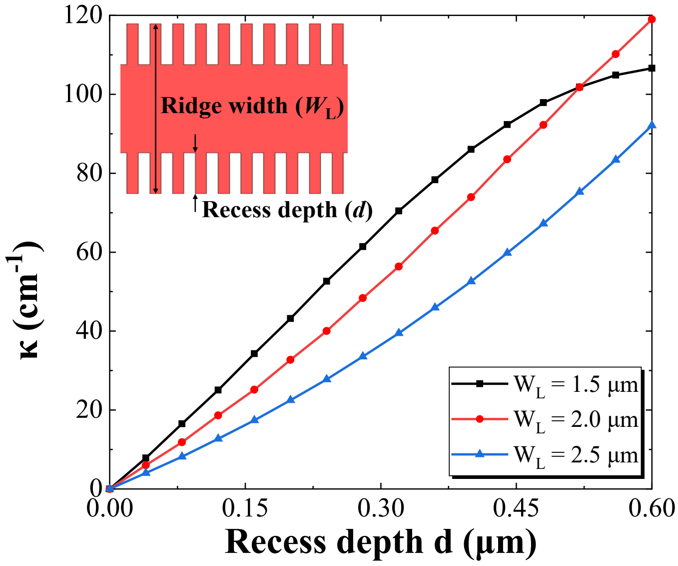

**Figure 5.1.3** Sidewall grating coupling coefficient κ as the grating recess depth d, for ridge waveguide widths $W_L$ = 2.5, 2.0 and 1.5 μm.

# 5.2 DFB-PMC device

The monolithic LD-PMC device, as illustrated in Figure 5.2.1 (a), comprises a 2.5-µm-wide ridge waveguide AlGaInAs DFB laser that operates at 1550 nm, a 50-µm-long taper interconnection, and two symmetric input and output ridge waveguides separated by the stepped height ridge waveguide PMC. Cross-sectional views of the input/output waveguide and the PMC are presented in Figure 5.2.1 (b). Here $W_0$ and $W$ are the widths of the ridge waveguide and dry-etch corner, and $D_0$ and $D$ are their dry-etched depths respectively. The etched depth $D$ can be precisely controlled because the top 60 nm thick AlGaInAs waveguide layer acts as a dry etch stop layer when using $CH_4/H_2/O_2$ RIE recipe.

The value of $D$ is set at 1.92 µm, and $D_0$ was set at 3.3 µm. Modelling results indicate that for $D_0 \geq 3.3$ µm, the etch depth $D_0$ does not influence the eigenmode profiles. The ridge waveguide width, $W_0$, can be defined using the high resolution of the EBL. Hence, the PCE is only sensitive to the width $W$ of the dry-etch corner. The light from the laser is TE-polarized, resulting in 100% $TE_0$ and 0% $TM_0$ power fractions at the input of the PMC, as shown in Fig. 5.2.1 (c). According to [6], to achieve the highest TE-TM conversion efficiency, the axes of the $TE_0$ and $TM_0$ eigenmodes in the asymmetric PMC waveguide should be rotated by 45° with respect to the input straight waveguide (see Fig. 5.2.1 (b)), which means the TE-polarized power fraction in both $TE_0$ and $TM_0$ profiles presented in Fig. 5.2.1(d) is 50%. After propagating a half-beat length $L_\pi$ the polarization is rotated 90°, and the output becomes TM-polarized. Hence, this design primarily requires optimizing the widths $W_0$ and $W$ to achieve a 45° rotation of $TE_0$ and $TM_0$. Similar to the half-ridge waveguide, the step-height PMC waveguide must support only the fundamental $TE_0$ and $TM_0$ modes, The effective modal index ($N_{eff}$) values for the first four modes ($TE_0$, $TM_0$, $TE_1$, $TM_1$) were calculated using the FEM Solver and are presented in Figure 5.2.2. These results indicate that for 1.0 µm $\leq W_0 \leq$ 2.0 µm, only the $TE_0$ and $TM_0$ modes are supported. Figure 5.2.3 shows a contour plot of the calculated PCE and $L_\pi$ as a function of $W_0$ and $W$. The final optimum widths of the PMC waveguide chosen here are $W_0 = 1.42$ µm and $W = 0.415$ µm, which provide a high PCE (96%) and short $L_\pi$ (537 μm).

Fig. 5.2.4 (a) shows the $N_{\mathrm{eff}}$ and effective modal indexes difference $\Delta N_{eff}$ of the $\mathrm{TE_0}$, $\mathrm{TM_0}$ modes ($\Delta N_{eff} = N_{eff}(\mathrm{TE_0}) - N_{eff}(\mathrm{TM_0})$) as the function of the FRL thickness ($T$). These results indicate for $T \geq 0.1$ μm, both the $\mathrm{TE_0}$ and $\mathrm{TM_0}$ modes are maintained and the minimum $\Delta N_{eff}$ of 0.00128 is achieved at T = 0.375 μm. Fig. 5.2.4 (b) presents the PCE and $L_\pi$ as the function of $T$ for the optimum PMC dimensions of $W_0 = 1.42$ μm, $W = 0.415$ μm and $L_{PMC} = 490$ μm from the aforementioned narrow-range optimization results. It is indicated that the highest PCE (96%) is achieved when the FRL thickness is set at 0.3 μm, with a relatively short short $L_\pi$ (537 μm). Therefore, a 300 nm thick FRL represents a good balance between PCE and $L_\pi$.

The fabrication tolerances were also investigated. the length of the PMC ($L_{PMC}$) was fixed at 537 μm and waveguide deep-etch depth ($D_0$) at 3.3 μm. Figure 5.2.5(a) shows presents the PCE variation as a function of the dry-etch corner width (W) for three different ridge waveguide widths ($W_0$). It is shown that for the optimum value of waveguide width, $W_0 = 1.42$ μm, the PCE decreases by 6.25% over the range of corner width, $W = 0.415 \pm 0.05$ μm. It also can be seen that a deviation of ± 0.02 μm in $W_0$ causes a 3.9% reduction of PCE for the optimum waveguide width $W = 0.415$ μm. Figure 5.2.5 (b) presents the results of sweeping $W_0$ are where $W_0$ varying over the range 1.42 ± 0.03 μm results in the PCE decreasing by up to 6.8%. Furthermore, Figure 5.2.5 (c) presents the conversion efficiency as a function of dry-etch corner depth ($D$) for $W_0 = 1.42$ μm and $W = 0.415$ μm. A deviation of ±0.05 μm from the optimum $D$ of 1.92 μm results in a 16% decrease in PCE. Figure 5.2.5 (d) shows the power conversion efficiency (PCE) as a function of the operating wavelength for the optimized dimensions of the photonic crystal (PMC), $W_0 = 1.42$ μm, $W = 0.415$ μm and $L_{PMC} = 537$ μm. The PCE exceeds 90% over the entire C-band (1530-1565 nm). We also investigated the PMC structure without QWI shown in Figure 5.2.6, The optimum widths of the PMC waveguide chosen here are $W_0 = 1.38$ μm and $W = 0.4$ μm, which provide a high PCE (97%) and short $L_\pi$ (490 μm).

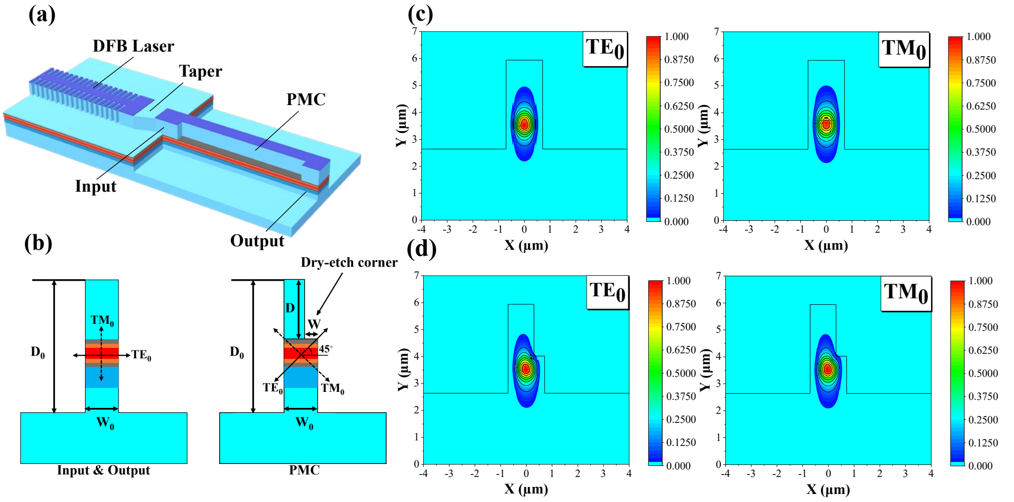

**Figure 5.2.1** (a) Monolithic LD-PMC device. (b) Cross-section of the input/output waveguides (left) and PMC waveguide (right). (c) The two fundamental eigenmodes $TE_0$ and $TM_0$ profile in the input section ($W_0$ = 1.42 μm, $D_0$ = 3.3μm). (d) $TE_0$ and $TM_0$ profiles in the PMC ($W_0$ = 1.42 μm, $W$ = 0.415 μm, $D_0$ = 3.3μm).

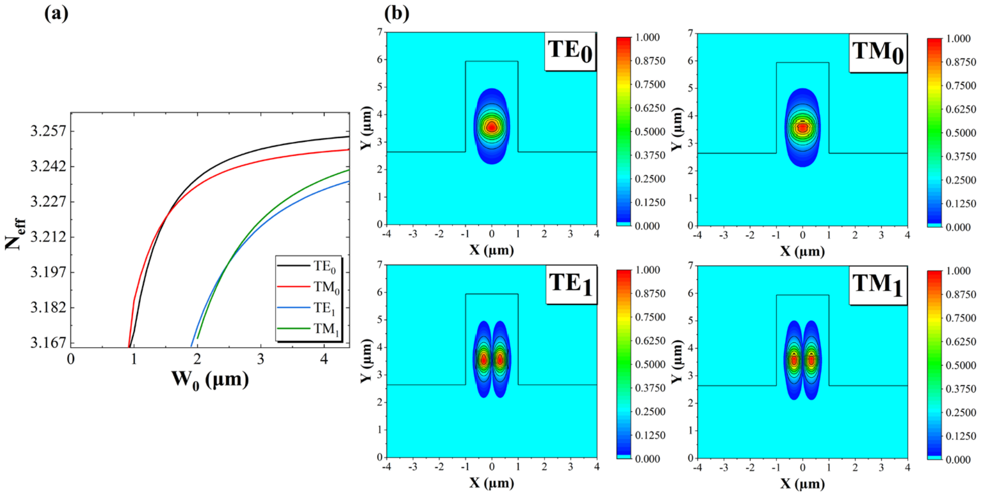

**Figure 5.2.2** (a) Calculated waveguide $N_{eff}$ of the $TE_0$, $TM_0$, $TE_1$, $TM_1$ modes as a function of the ridge waveguide width $W_0$. (b) Simulated $TE_0$ and $TM_0$, $TE_1$ and $TM_1$ mode profiles for a ridge waveguide width ($W_0$) of 2.1 μm and height ($D_0$) of 3.3 μm.

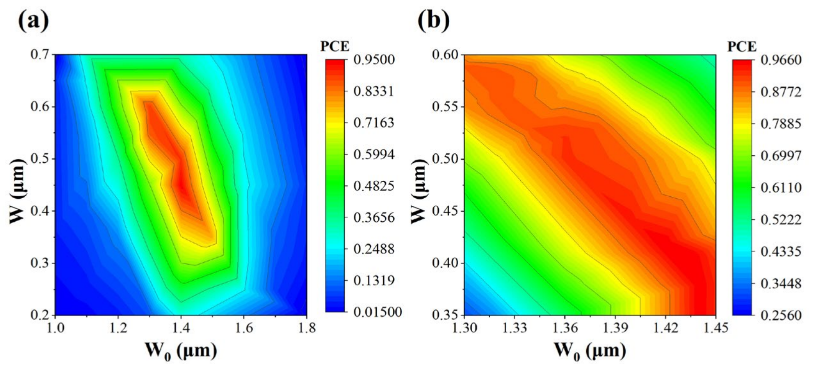

**Figure 5.2.3** (a) Broad-range optimization of PCE as a function of waveguide width ($W_0$) and corner width ($W$), (b) narrow-range optimization.

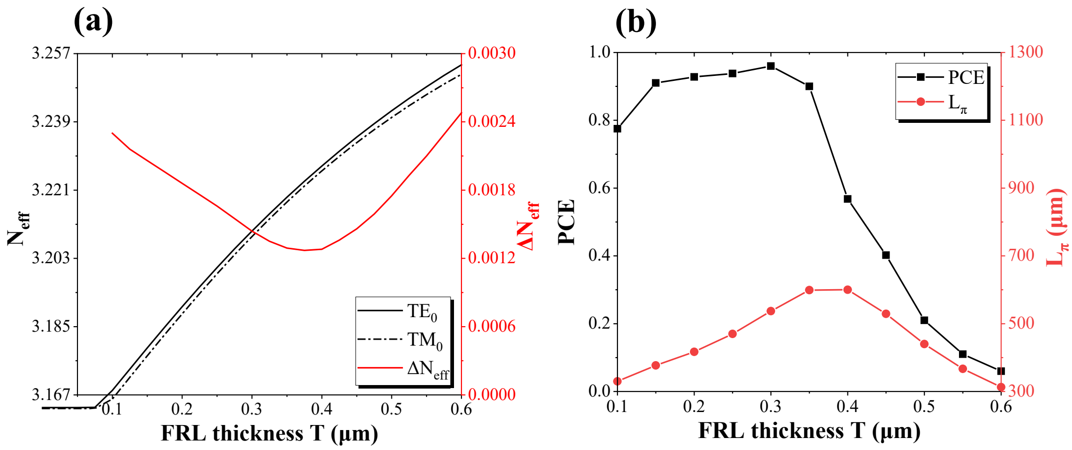

**Figure 5.2.4** (a) Calculated waveguide $N_{eff}$ and refractive index difference $\Delta N_{eff}$ of the TE$_0$, TM$_0$ modes as a function of the FRL thickness $T$. (b) Variation of PCE and $L_\pi$ as a function of FRL thickness $T$ ($W$ = 1.42 µm, $W_0$ = 0.415 µm and $L_{PMC}$ = 537 µm, $D_0$ = 3.3µm).

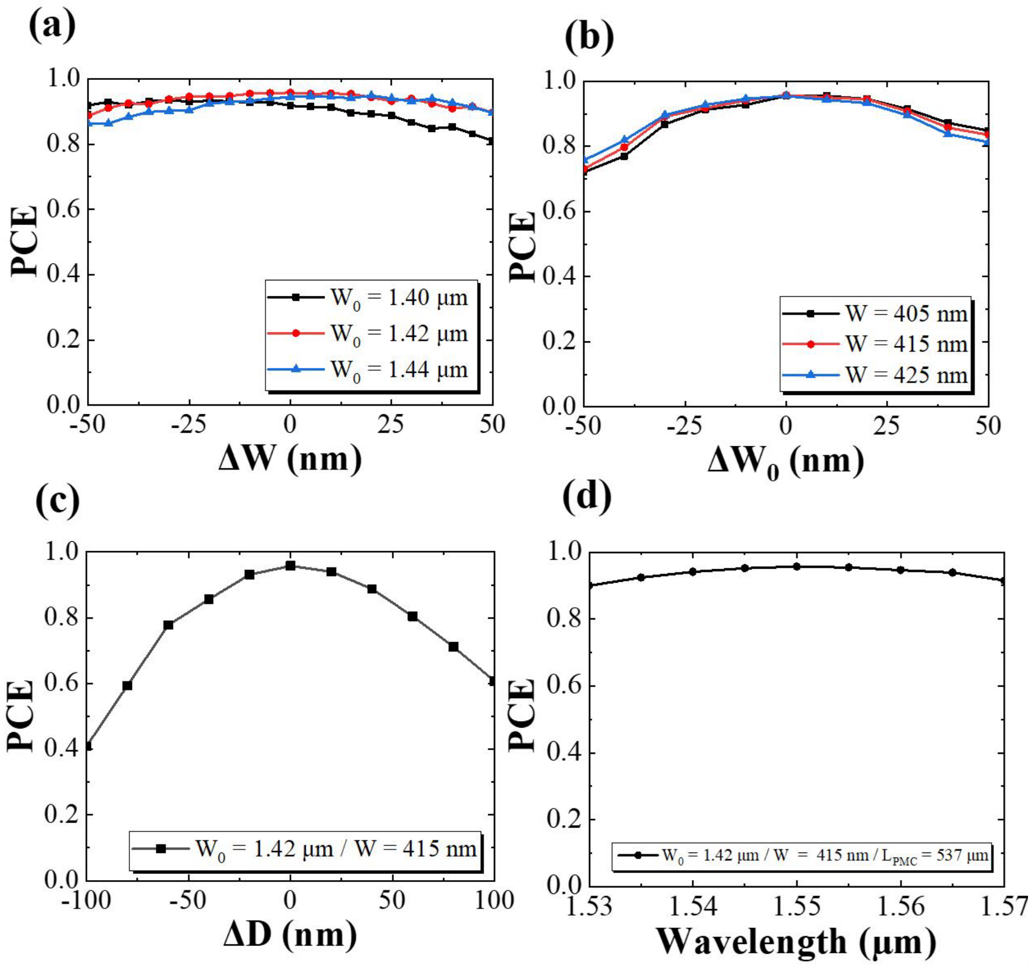

**Figure 5.2.5** (a) Variation of PCE as a function of dry-etch corner width $W$ (optimal $W$ = 0.415 µm for $W_0$ = 1.40 µm, 1.42 µm and 1.44 µm, $L_{PMC}$ = 537 µm). (b) PCE with respect to waveguide width $W_0$ (optimal $W_0$ = 1.42 µm for $W$ = 0.405 µm, 0.415 µm and 0.425 µm, $L_{PMC}$ = 537 µm). (c) PCE with respect to dry-etch corner depth $D$ ($W_0$ = 1.42 µm, $W$ = 0.415 µm and $L_{PMC}$ = 537 µm). (d) Wavelength dependence of PCE ($W$ = 1.42 µm, $W_0$ = 0.415 µm and $L_{PMC}$ = 537).

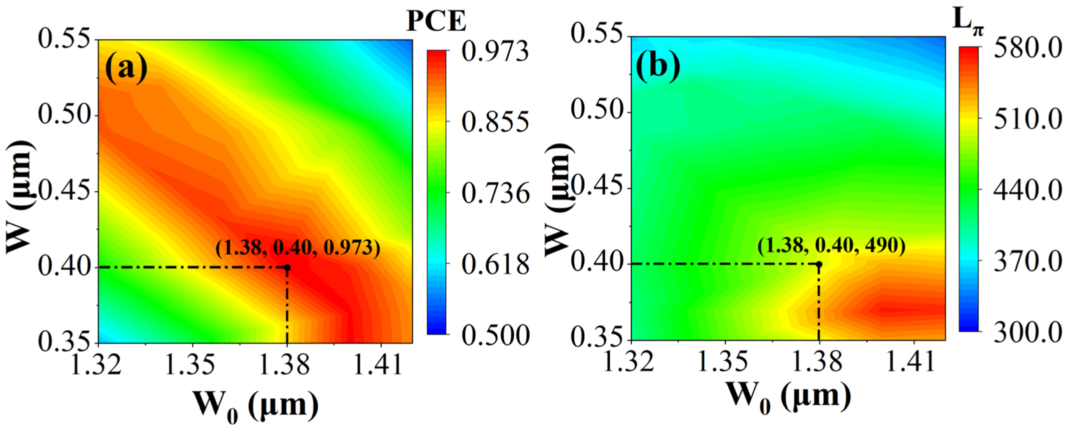

**Figure 5.2.6** (a) -(b) Calculated maximum PCE without QWI process (a), and corresponding $L_\pi$ (b) as a function of waveguide width ($W_0$) and corner width ($W$).

## 5.3 DFB-PMC device fabrication

The DFB-PMC device fabrication processes are presented in Fig. 5.3.1. The wafer was grown on an InP substrate by MOVPE (Fig.5.3.1(a)). The DFB grating and the first step waveguide pattern for the PMC were defined using electron-beam lithography (EBL), with negative tone Hydrogen Silsesquioxane (HSQ) used as the EBL resist and hard mask for inductively coupled plasma (ICP) dry etching (Fig.5.3.1(b)). Figure 5.3.1(c) shows the shallow etched ridge, which took place in two stages. First, the ridge was etched to a depth of 1.89 μm using a $Cl_2/CH_4/H_2/Ar$ gas mixture in an ICP cobra, the average etch rate for InP and InGaAsP being about 183 nm/min. Then the gas recipe was changed to $CH_4/H_2/O_2$, to etch the ridge to a final depth of 1.92 μm. This could be stopped on the AlGaInAs layer, as the average etch rate of InP/ InGaAsP was about 78 nm/min, and AlGaInAs was 3 nm/s, achieving 26-fold selectivity. After the shallow etch, both the DFB section and the top and one side of the PMC were protected by HSQ defined by EBL as shown in Fig.5.3.1(d). Subsequently, a second stage of $Cl_2/CH_4/H_2/Ar$ ICP etching was used to etch one side of the PMC waveguide to a depth of 3.3 μm (Fig.5.3.1(e)). Finally, all HSQ was removed by Hydrofluoric (HF) acid as shown in Fig.5.3.1(f). The fabrication process required only a single step of MOVPE and two steps of III-V material dry etching for the entire integrated device, as shown in Fig.5.3.1(g). Scanning electron microscope (SEM) images of the PMC waveguide after the first shallow etch, second step EBL and deep etch are shown in Fig.5.3.1(h), (i), and (j) respectively. The subsequent deposition of $SiO_2$ and HSQ passivation layers, $SiO_2$ window opening, P-contact deposition, substrate thinning, and N-contact deposition were the same as for conventional LD fabrication [5], which have been explained in detail at chapter 3. SEM images of the DFB grating, output facet of PMC, and DFB-PMC device are presented in Fig. 5.3.2(a)-(c). An optical microscope picture of the completed DFB-PMC device is depicted in Fig.5.3.2(d). We note the fabricated PMC length should be kept as close as possible to the designed value by precise control of the cleaving. Here a LOOMIS LSD-100 cleaving tool was used with a cleaving accuracy of ±1 μm. The resulting variation in the PCE is less than 0.1%, confirming the tool meets the required cleaving tolerance.

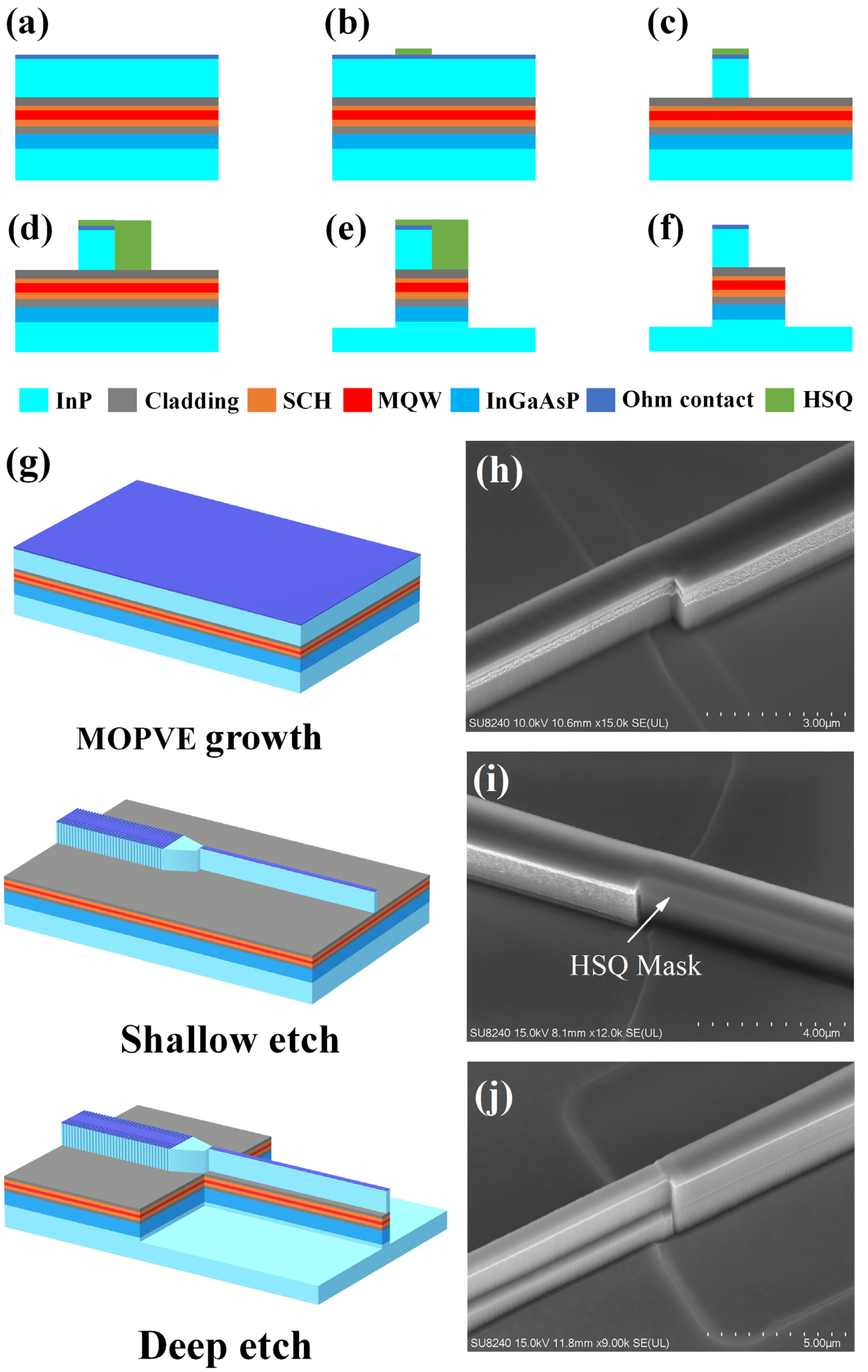

**Figure 5.3.1** (a)-(f) Fabrication procedures: (a) MOVPE epilayer growth, (b) EBL to define the laser and PMC first step waveguide, (c) ICP shallow etching, (d) EBL to define the second step waveguide of PMC, (e) ICP deep etching, (f) HSQ elimination, (g) workflow of monolithic DFB-PMC device fabrication, (h)-(j) SEM images of (h) after the first shallow etch, (i) second step EBL using HSQ photoresist, (j) PMC deep etch and HSQ elimination.

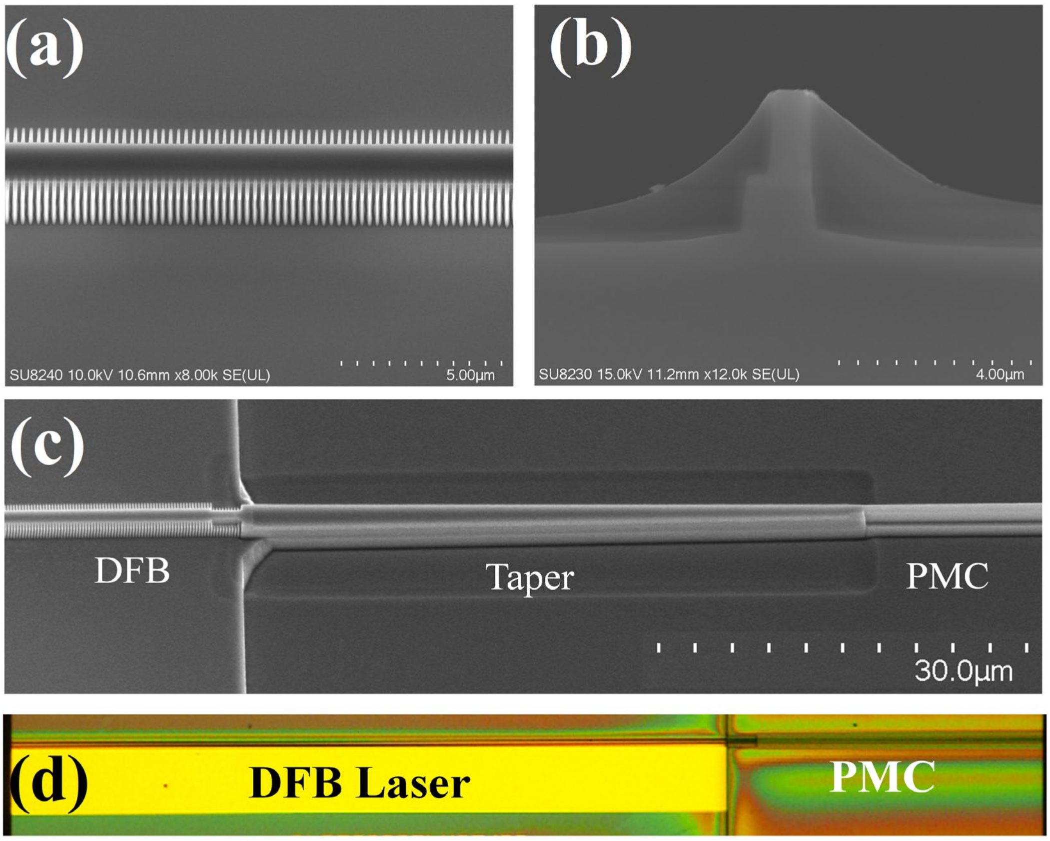

**Figure 5.3.2** (a) SEM image of DFB SWGs, (b) output facet of PMC, (c) SEM images of DFB-PMC device, (d) microscope picture of the DFB -PMC device.

# 5.4 Device measurement

## 5.4.1. Optical spectrum measurement

As described above, for the DFB-PMC device, DFBs were fabricated with three Bragg wavelengths, i.e., 1540 nm, 1550 nm, and 1565 nm. Figure 5.4.1 shows their optical spectra at specific injection DFB currents ($I_{DFB}$) and 2-D optical spectra as a function of $I_{DFB}$ from the DFB rear side and PMC side respectively. All spectra were measured with a resolution bandwidth (RBW) of 0.06 nm. The measurement results of wavelength, single mode suppression ratios (SMSRs), and average current-induced wavelength redshift coefficient (ACWRC) are listed in Table 5.4.1. The measured wavelengths of the DFB lasers designed to operate at 1540 nm, 1550 nm, and 1565 nm are 1543.6 nm, 1555.8 nm, and 1568.2 nm, with $I_{DFB}$ set at 150 mA, 170 mA, and 170 mA respectively. Compared to the designed Bragg wavelengths, the measured wavelengths are slightly redshifted due to the heating effect. The corresponding SMSRs measured from the DFB rear facet are 27 dB, 29 dB, and 38 dB respectively. At the PMC output facet, the SMSRs were reduced to 8 dB, 12 dB, and 20 dB. This is due to the significant inter-band and exciton absorption inside the PMC waveguide when the propagating light wavelength is close to the PL wavelength (1530 nm) of the MQW core. The measured ACWRCs from the DFB and PMC sides are 0.025 nm/mA, 0.0207 nm/mA, and 0.0271 nm/mA for Bragg grating wavelengths at 1540 nm, 1550 nm and 1565 nm respectively, all exhibiting stable SLM operation.

**Table 5.4.1.** Measured parameters of the three DFB-PMC devices with different designed Bragg wavelengths.

| **Designed Brag grating wavelength (nm)** | **SMSR (dB) DFB facet** | **SMSR (dB) PMC facet** | **Measured current (mA) and wavelength ranges (nm)** | **ACWRC (nm/mA)** |
|---|---|---|---|---|
| 1540 | 27 | 8 | **Current**: 118 - 170<br>**Wavelength:** 1542.9-1544.2 | 0.0250 |
| 1550 | 29 | 12 | **Current**: 104 - 220<br>**Wavelength:** 1554.2-1556.6 | 0.0207 |
| 1565 | 38 | 20 | **Current**: 97 - 211<br>**Wavelength:** 1566.3-1569.4 | 0.0271 |

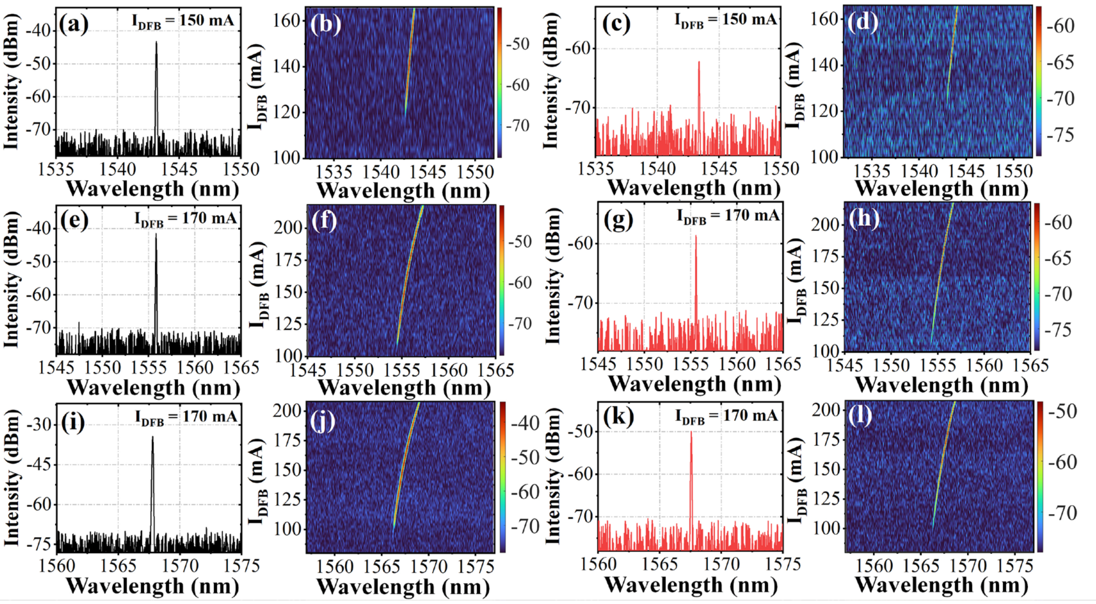

**Figure 5.4.1** (a)-(d) Measured optical spectra for 1543 nm DFB-PMC device measured from DFB (a),(b) and PMC (c) (d) facets. (e)-(h) Optical spectra for 1555 nm DFB-PMC device from DFB (e),(f) and PMC (g),(h) facets. (i)-(l) Optical spectra for 1567 nm DFB-PMC device from DFB (i),(j) and PMC (k),(l) facets.

To estimate the internal loss in the PMC waveguide, an 800 μm length FP laser was fabricated in the same wafer and fabrication run, and the internal loss in the waveguide was 9±1 $\text{cm}^{-1}$ measured by the Haki-Paoli method (shown in Fig. 5.4.2 (a)). To estimate the $\kappa$ value of the DFB lasers, an 800-μm-long DFB laser with a Bragg wavelength of 1565 nm and a π-phase shift section inserted at the center of the cavity was also fabricated. Fig. 5.4.2 (b) shows the optical spectrum at the threshold current (68 mA). The measured central wavelength is 1566.5 nm, and the stop bandwidth ($\Delta\lambda_s$) is 1.14 nm. The grating coupling coefficient κ can be estimated using [7]:

$$\kappa = n_{eff} \frac{\Delta\lambda_s}{\lambda_B{}^2} \tag{5.3.1}$$

where $n_{eff}$ is the effective index (3.26); $\lambda_B$ is the lasing wavelength of the DFB laser. The $\kappa$ of the fabricated grating is estimated to be ~15 $\text{cm}^{-1}$, and $\kappa L = 1.8$ for the 1200 μm length DFB laser, which ensures stable SLM operation.

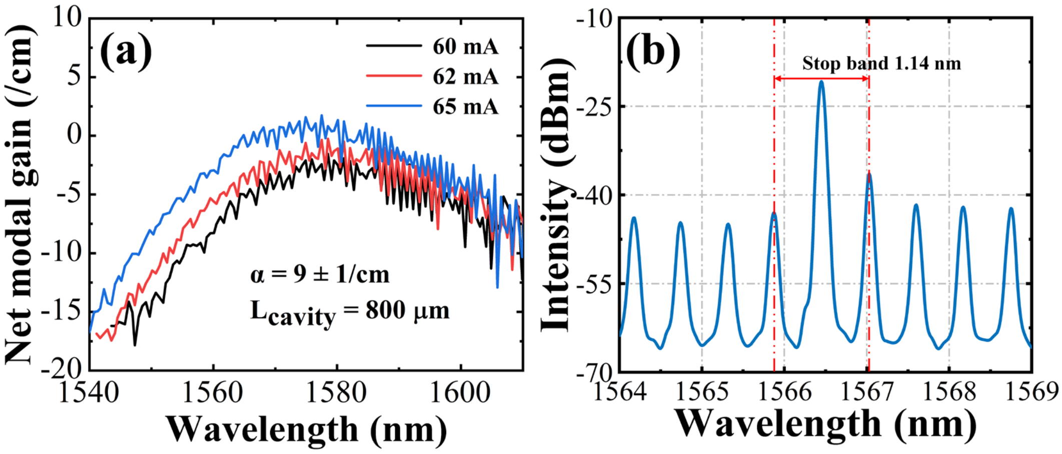

**Figure 5.4.2** (a) Measured net modal gain as a function of the wavelength using the Haki-Paoli method, (b) optical spectrum at threshold current (68 mA) of an 800 μm length DFB LD with a π-phase shift section inserted at the center of the DFB LD cavity.

## 5.4.2. State of polarization measurement

The setup for the SOP measurement is shown in Fig. 5.4.3. Devices were mounted on a thermoelectric cooler (TEC) and temperature controlled at 20 °C as stated previously. The output light from the PMC was coupled into a lensed polarization- maintaining fiber and transmitted to a polarimeter to measure the SOP. Both the current driver and the polarimeter were controlled by a computer through the general-purpose interface bus (GPIB) interface by LabVIEW software. We first measured the SOP at the DFB laser rear facet at $I_{DFB}$ from 104 mA to 210 mA, and the $SV$ was constant at (0.998,0.05,0.04). Fig. 5.4.4(a)-(c) presents the $SV$ at the PMC facets of DFB-PMC devices with different Bragg wavelengths. The PCE was calculated from Eq. (2) and the values are listed in Table 5.4.2. For the DFB-PMC device with a designed Bragg wavelength at 1550 nm, the average $S_1$ parameter was –0.968 representing a PCE of 98.4% for 140 mA < $I_{DFB}$ < 190 mA (corresponding wavelength range 1554.9 – 1555.9 nm). The maximum PCE was 99.1% measured at $I_{DFB}$ =180 mA. The deviation of the measured PCE is due to the measurement errors caused by the noise of the DC source driving the DFB laser, and environmental influences such as temperature fluctuations and mechanical vibration.

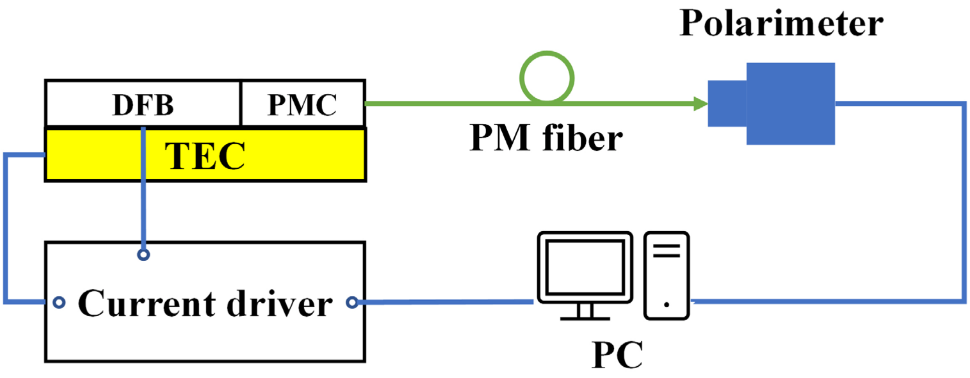

**Figure 5.4.3** Experimental setup for the SOP measurement for DFB-PMC devices.

**Table 5.4.2.** Measured PCE from the PMC side of the DFB-PMC devices.

| Designed DFB laser Wavelengths (nm) | Measured DFB laser wavelengths (nm) | Current range (mA) | Average PCE | MAX PCE |
|---|---|---|---|---|
| 1540 | 1543.6-1544.2 | 150-170 | 93.0 % | 94.3 % |
| 1550 | 1554.9-1555.9 | 140-190 | 98.4 % | 99.1 % |
| 1565 | 1567.4-1568.7 | 140-190 | 89.8 % | 90.5 % |

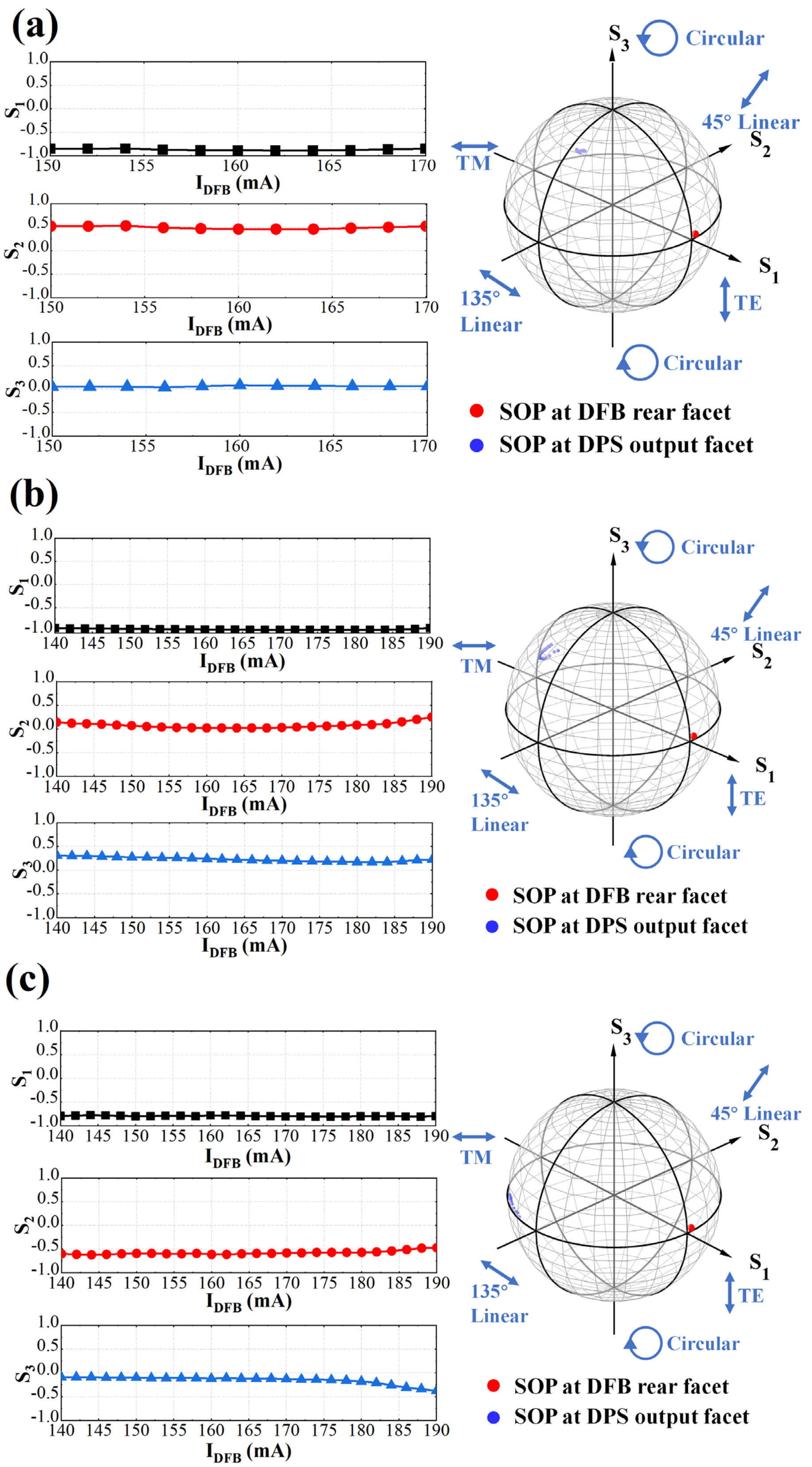

**Figure 5.4.4** Measured SV at PMC side for (a) 1543 nm, (b) 1555 nm, (c) 1568 nm wavelength DFB-PMC devices.

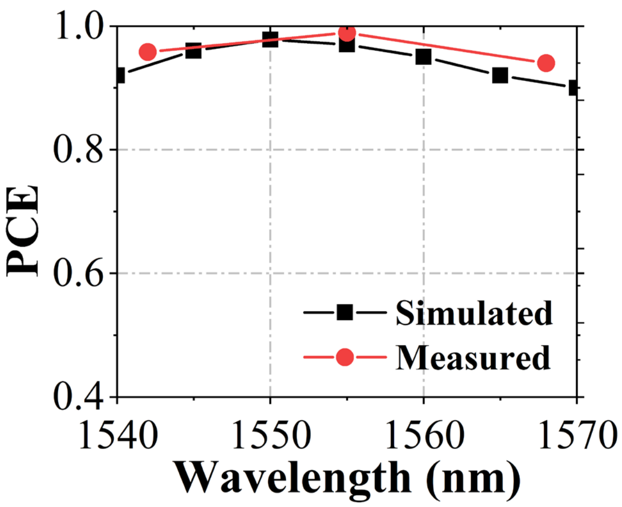

**Figure 5.4.5** Simulated and measured PCE versus DFB lasing wavelength.

For the DFB-PMC device with a designed Bragg wavelength at 1540 nm, the average PCE over the wavelength range from 1543.6 nm to 1544.2 nm was found to be 93% for 150 mA < $I_{DFB}$ < 170 mA and the maximum PCE was found to be 94.3% at $I_{DFB}$ =162 mA. For the DFB-PMC device with a designed Bragg wavelength at 1565 nm, the average PCE was 89.8% over the range 140 mA < $I_{DFB}$ < 190 mA and wavelength from 1567.4 to 1568.7 nm. The maximum PCE was 90.5% (at $I_{DFB}$ =174 mA). Fig. 5.4.5 presents a comparison between the calculated PCE from the Full-Wave simulation and the measured average PCE as a function of wavelength. There is very good agreement between the simulated and measured results.

# 5.5 Conclusion

For the first time, we proposed and fabricated an SWG DFB laser monolithically integrated with a PMC on the identical epitaxial layer PIC scheme. For the 490-µm-long PMC devices, a TE/TM conversion efficiency of 98.4 % was obtained over a broad range of $I_{DFB}$ from 140 mA to 190 mA at a 1555 nm operating wavelength. The wavelength dependence was also calculated and measured. The devices have a PCE >90% over the wavelength range of 1543 nm to 1568 nm.

# References of this chapter

[1] B. Qiu, O. Kowalski, S. McDougall, B. Schmidt, and J. H. Marsh, "High-performance red lasers with low beam divergence," *IEEE Photonics Journal,* vol. 1, no. 3, pp. 172-177, 2009.

[2] J. Crank, *The mathematics of diffusion*. Oxford university press, 1979.

[3] S. Adachi, *Physical properties of III-V semiconductor compounds*. John Wiley & Sons, 1992.

[4] M. Guden and J. Piprek, "Material parameters of quaternary III-V semiconductors for multilayer mirrors at wavelength," *Modelling and Simulation in Materials Science and Engineering,* vol. 4, no. 4, p. 349, 1996.

[5] L. Hou, M. Tan, M. Haji, I. Eddie, and J. H. Marsh, "EML based on side-wall grating and identical epitaxial layer scheme," *IEEE Photonics Technology Letters,* vol. 25, no. 12, pp. 1169-1172, 2013.

[6] H. Deng, D. O. Yevick, C. Brooks, and P. E. Jessop, "Design Rules for Slanted-Angle Polarization Rotators," *Journal of Lightwave Technology,* vol. 23, no. 1, pp. 432-445, 2005.

[7] M. Razeghi *et al.*, "Low-threshold distributed feedback lasers fabricated on material grown completely by LP-MOCVD," *IEEE journal of quantum electronics,* vol. 21, no. 6, pp. 507-511, 1985.

# Chapter 6 DFB-PMC-DPS device

## 6.1 Theory and design

A new type of polarization controller, known as DFB-PMC-DPS, has also been proposed and compared to the DFB-PMC device which has already been discussed in chapter 5, as shown in Fig. 6.1.1 (a). In the DFB-PMC-DPS, the length of the PMCs is half that of the DFB-PMC device, and the length of the DPS is set at 100 μm. Fig. 6.1.1 (b) illustrates the *SV* rotation inside these two devices. In the DFB-PMC device, the SV rotates around the $S_2$ axis and arrives on the $S_1$-$S_2$ plane, where the output mode is TM-polarized. In contrast, in the DFB-PMC-DPS device, after passing through the PMC, the *SV* rotates around the $S_2$ axis (red line) and reaches close to the north pole, corresponding to counterclockwise circular polarization. The *SV* is then rotated around the $S_1$ axis within the $S_2$-$S_3$ plane by using the reverse-biased DPS section (green line). Assuming a TE polarized input ($S = (1,0,0)$), the variation of $S = (S_1, S_2, S_3)^{tr}$ and the PCE inside the PMC waveguide can be found from [1, 2]:

$$S = \begin{pmatrix} S_1 \\ S_2 \\ S_3 \end{pmatrix} = \begin{pmatrix} 1 - 2\sin^2(2\varphi)\sin^2\left(\pi \dfrac{L_{PMC}}{2L_\pi}\right) \\ \sin(4\varphi)\sin\left(\pi \dfrac{L_{PMC}}{2L_\pi}\right) \\ \sin(2\varphi)\sin\left(\pi \dfrac{L_{PMC}}{L_\pi}\right) \end{pmatrix} \quad \textbf{(6.1.1)}$$

$$PCE = \sin^2(2\varphi)\sin^2\left(\pi \frac{L_{PMC}}{2L_\pi}\right) = \frac{1 - S_1}{2} \times 100\% \quad \textbf{(6.1.2)}$$

The DPS waveguide utilizes the band-filling effect (under forward bias) or the QCSE (under reverse bias) to achieve a phase shift between the $TE_0$ and $TM_0$ modes. As the phase modulation efficiency generally differs for these modes, the SV rotation angle $\Delta\theta$

in the DPS can be tuned via the applied bias voltage [1].

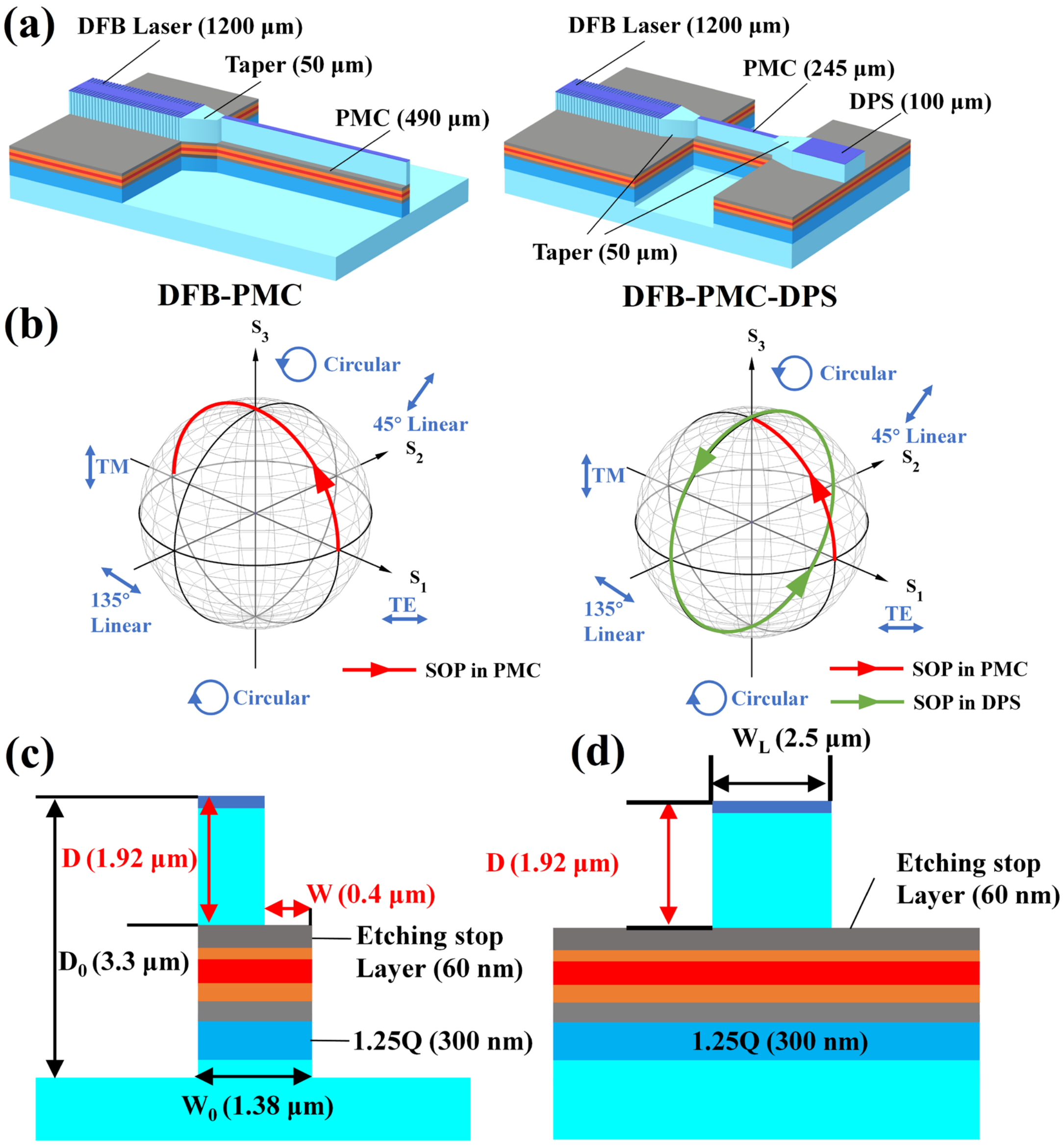

**Figure 6.1.1** (a) Schematic of the monolithic DFB-PMC device (left), and DFB-PMC-DPS device (right), (b) *SV* propagates inside DFB-PMC (left), and DFB-PMC-DPS device (right), (c) cross-section structure of the PMC, (d) cross-section structure of the DPS.

The QCSE-based DPSs have faster picosecond switching speeds compared to band-filling effect-based DPSs which have nanosecond switching speeds[3], although the measurement of switching speeds is not within the scope of this paper. Hence, the reverse bias operation of the DPS is preferred to change the rotation angle $\Delta\theta$, which can be calculated using the following equation:

$$\Delta\theta = (\Delta\beta_{TE} - \Delta\beta_{TM}) \times L_{DPS} = \frac{2\pi L_{DPS}}{\lambda}(\Delta n_{TE} - \Delta n_{TM}) \qquad \textbf{(6.1.3)}$$

where $\Delta n_{TE}$ and $\Delta n_{TM}$ are the changes of the refractive index of the $TE_0$ and $TM_0$ modes respectively, and are determined from the change in absorption coefficient ($\Delta\alpha$) using the Kramers−Krönig relationship in which the calculation has been discussed in section 2.1.6.

Fig. 6.1.2(a) displays the TE and TM absorption coefficients as a function of wavelength for the $V_{DPS}$ bias voltages of 0 V and -3 V. At 0 V bias voltage, the TE mode's modal absorption coefficient at 1.55 μm wavelength is approximately 9.76 $cm^{-1}$ which fits very well with our measured result of 9±1 $cm^{-1}$ and the TM mode absorption coefficient is 2.6 $cm^{-1}$. The TE modal absorption coefficient of 9.76 $cm^{-1}$. At -3 V bias voltage, the absorption coefficient is high (500 $cm^{-1}$), indicating that the DPS cannot be too long. Therefore, a 100 μm long DPS was utilized, which produced a 22 dB absorption loss at -3 V bias voltage, consistent with the measured value. Fig. 6.1.2(b) presents the difference of the effective refractive index changes between the TE and TM modes ($\Delta n_{TE} - \Delta n_{TM}$) for different $V_{DPS}$. The calculated $\Delta\theta$ as a function of $V_{DPS}$ at 1.557 μm wavelength is presented in Fig. 6.1.2 (c), with a predicted 71° phase shift at $V_{DPS} = -3.0$ V. For the DFB-PMC-DPS device, the fabrication process is the same as that of the DFB-PMC devices and will not be discussed in further detail.

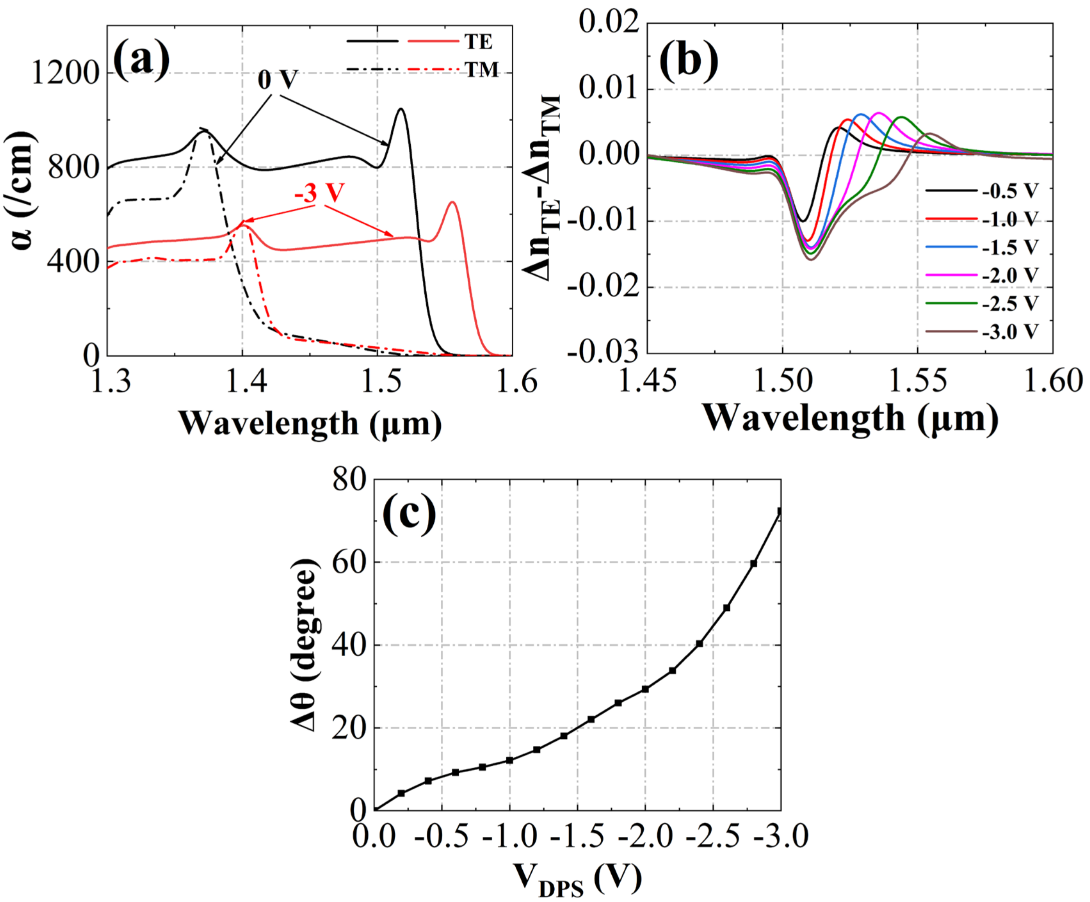

**Figure 6.1.2** (a) Calculated TE and TM absorption coefficient in the DPS. (b) The difference of the effective refractive index changes between TE and TM modes at different $V_{DPS}$. (c) Phase shifted angle as a function of $V_{DPS}$ at 1.557 μm operation wavelength.

# 6.2 Device measurement

## 6.2.1. Optical spectrum measurement

In light of the performance of the DFB-PMC devices, the DFB-PMC-DPS devices were fabricated with a Bragg grating wavelength at 1550 nm. Fig. 6.2.1 shows the optical spectra measured from the rear side of the DFB section and from the DPS output section with $V_{DPS}$ = 0 V. The peak lasing wavelength is at 1557.2 nm with an SMSR of 35 dB at the DFB facet for $I_{DFB}$ =170 mA, and the ACWRC is 0.023 nm/mA.

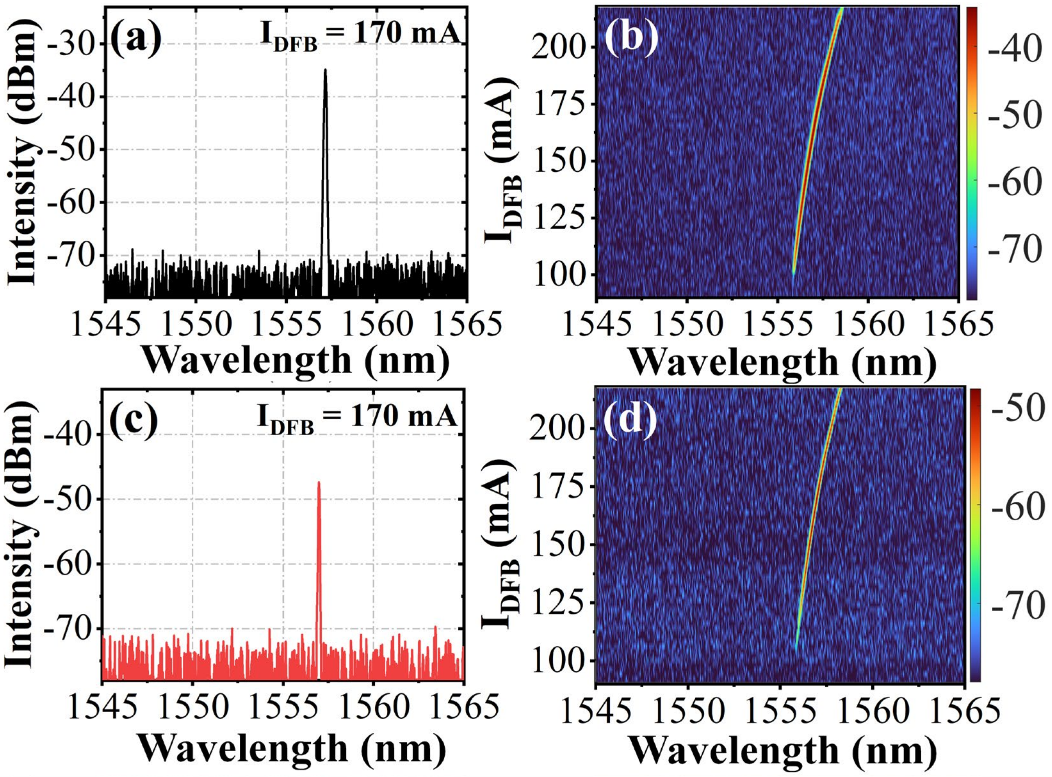

**Figure 6.2.1** (a)-(b) Measured optical spectrum from DFB LD rear facet, and (c)-(d) DPS section output facet.

### 6.2.2. State of polarization measurement

The setup for the SOP measurement is shown in Fig. 6.2.2, which is similar to the DFB-PMC setup and the DPS section is controlled by a voltage driver. For the DFB-PMC-DPS device, we first measured the *SV* at the DPS output facet with $V_{DPS} = 0$ V, as shown in Fig. 6.2.3 (a). The *SV* lies near (0.05, 0.5, 0.865) for the range of $I_{DFB}$ from 160 mA to 175 mA. There is a small deviation from a pure counterclockwise circular polarization state and is due to the birefringence of the taper and DPS waveguide. Then $I_{DFB}$ was fixed at 170 mA and $V_{DPS}$ was gradually changed from 0 V to −3 V. The *SV* measured at the DPS output facet is depicted in Fig. 6.2.3 (b). It is found that the *SV* rotates along the $S_2$-$S_3$ plane, and the measured rotation angle $\Delta\theta$ as a function of $V_{DPS}$ is presented in Fig. 6.2.4 along with the calculated result from Fig. 6.1.2 (c). A phase shift of nearly 60° is seen as $V_{DPS}$ is changed from 0.0 V to –3.0 V in steps of –0.2 V. When $V_{DPS}$ is changed from 0 V to −2.2 V, the measured and simulated values fit very well. When $|V_{DPS}| > 2.2$ V, the deviations between them increase, which may be due to measurement errors because the output power from the DPS is low, and the measurement accuracy is reduced.

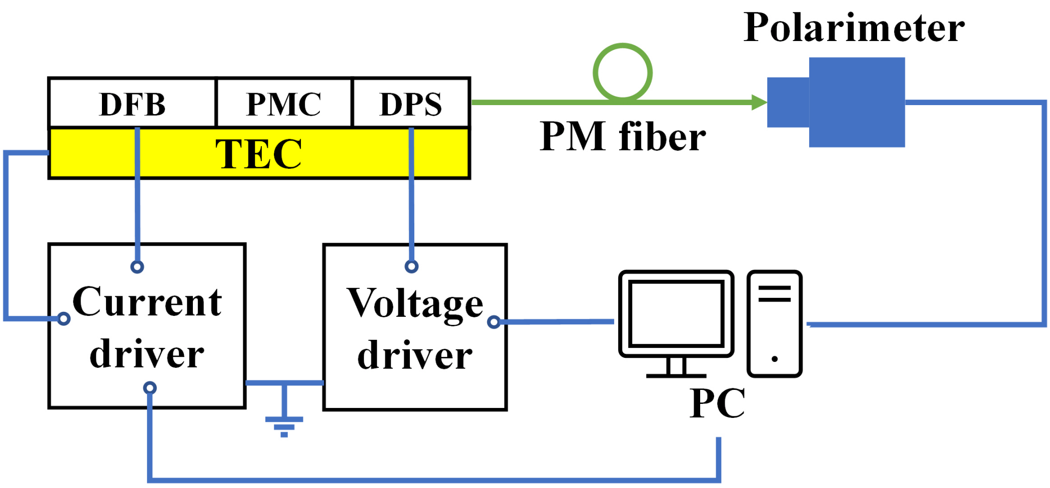

**Figure 6.2.2** Experimental setup for the SOP measurement for DFB-PMC-DPS devices.

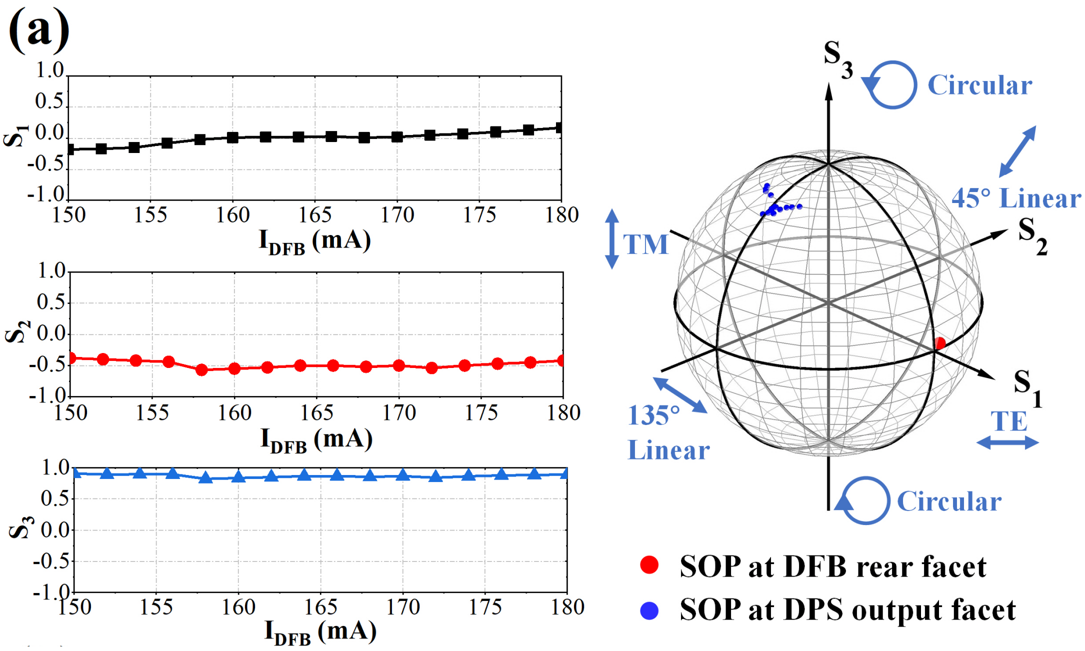

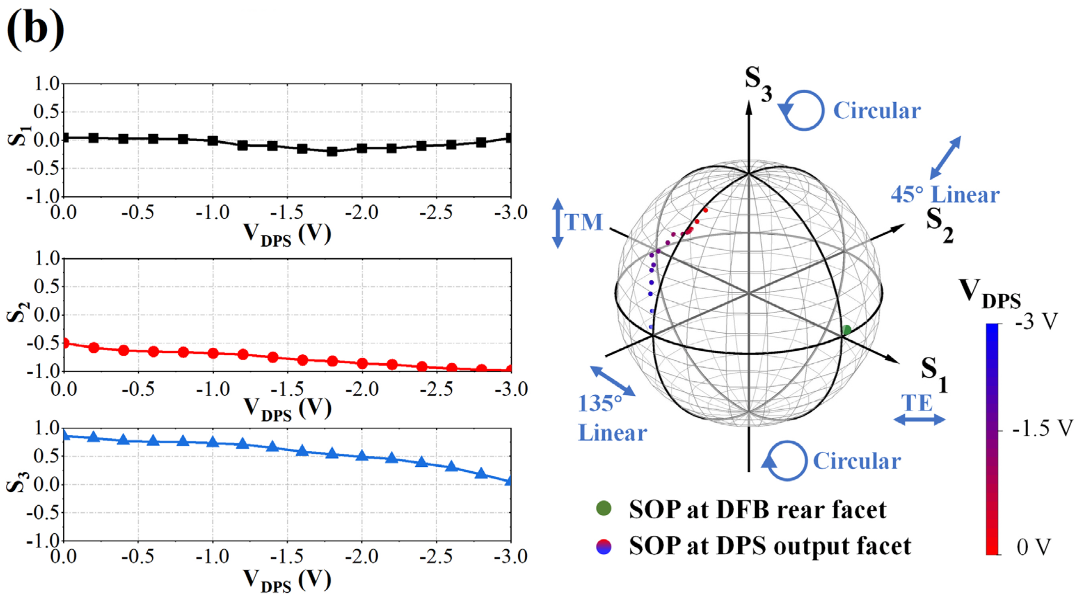

**Figure 6.2.3** (a) Measurement of *SV* at the DPS side as a function of $I_{DFB}$ with $V_{DPS}$ = 0 V, (b) rotation of *SV* at the DPS output facet as a function of $V_{DPS}$ for DFB-PMC-DPS devices with $I_{DFB}$ = 170 mA.

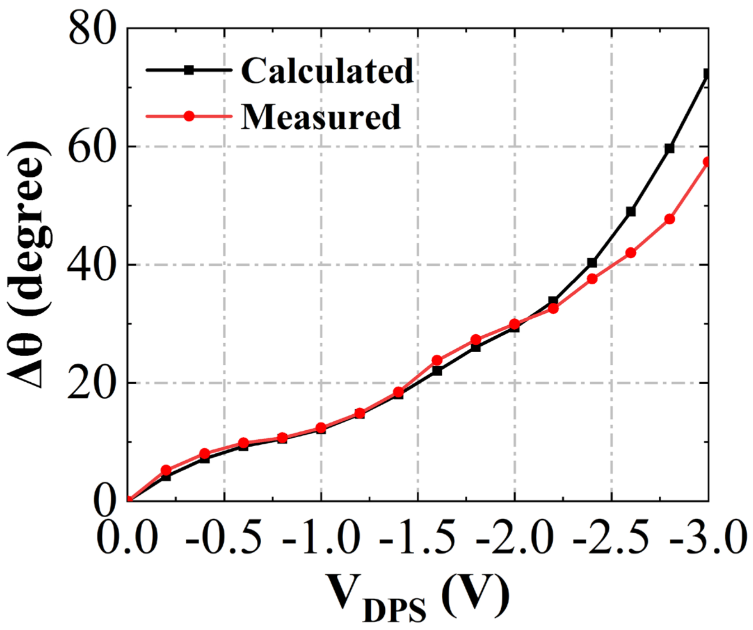

**Figure 6.2.4** Comparison between the measured and simulated phase shift angles as a function of $V_{DPS}$.

# 6.4. Discussion of quantum well intermixing (QWI) DPS

Here the reported rotation angle in the DPS is limited because the DPS is only 100 μm long. To increase the output power from the PMC or DPS side of the devices and improve the *SV* rotation performance in the DPS, quantum well intermixing (QWI) could be used to blueshift the bandgap in the PMC and DPS sections and reduce their absorption loss. In [13], we have proposed a PMC device with a 100 nm blue-shift by QWI, the degree of intermixing $N(z, L_D)$ is represented by the diffusion length ($L_D$) on the group III substance as

$$N(z,L_{\mathrm{D}})=(N_W-N_B)\left[1-\frac{1}{2}\mathrm{erf}\left(\frac{z-\frac{L_{\mathrm{W}}}{2}}{2L_{\mathrm{D}}}\right)+\frac{1}{2}\mathrm{erf}\left(\frac{z+\frac{L_{\mathrm{W}}}{2}}{2L_{\mathrm{D}}}\right)\right] \quad \textbf{(6.4.1)}$$

where $N_W$ and $N_B$ are the initial atomic mole fractions for QW and QB materials respectively, $z$ is the quantization direction along the growth axis (QW centered at $z = 0$), “erf” denotes the error function, and $L_W$ is the QW width. For the 100 nm blue-shift, $L_D$ is calculated to be 1.53 nm. As reported in [7], the TE and TM absorption coefficients in the DPS with a 100 nm blue-shift by QWI can also be calculated and are presented in Fig. 6.4.1(a). The modal absorption losses at 1.55 μm are about 4.75 $\mathrm{cm}^{-1}$ and 2.3 $\mathrm{cm}^{-1}$ for the TE and TM modes respectively for $V_{DPS}$ at both 0 V and −3 V, which are close to the measured results, i.e., 4.5 ± 0.5 $\mathrm{cm}^{-1}$ for TE and 2.0 ± 0.3 $\mathrm{cm}^{-1}$ for TM [8]. Therefore, after QWI, the applying a high $V_{DPS}$ will not result in excessively high absorption in the DPS section and the absorption losses in the PMC waveguide will also be reduced. Fig. 6.4.1(b) depicts the value of ($\Delta n_{TE}$ - $\Delta n_{TM}$) of the DPS as a function of wavelength with different bias voltages after a 100 nm blueshift by the QWI technique. The change in ($\Delta n_{TE}$ - $\Delta n_{TM}$) at 1.55 μm is negative, which means the rotation angle has an opposite direction compared to the as-grown QW. Although the absolute value of ($\Delta n_{TE}$ - $\Delta n_{TM}$) is lower than for the as-grown QW at 1.55 μm, due to the low absorption the length of DPS can be extended to increase $\Delta\theta$ in the DPS. For example, the DPS length could be set to 900 μm when its absorption loss is calculated to be only 0.21 dB. The phase shift angle $\Delta\theta$ as a function of $V_{DPS}$ is shown in Fig. 6.4.2 A full 360° rotation of the $SV$ can then be achieved when $V_{DPS} = -3.0$ V. This result shows that QWI can enhance the performance of DFB-PMC-DPS devices.

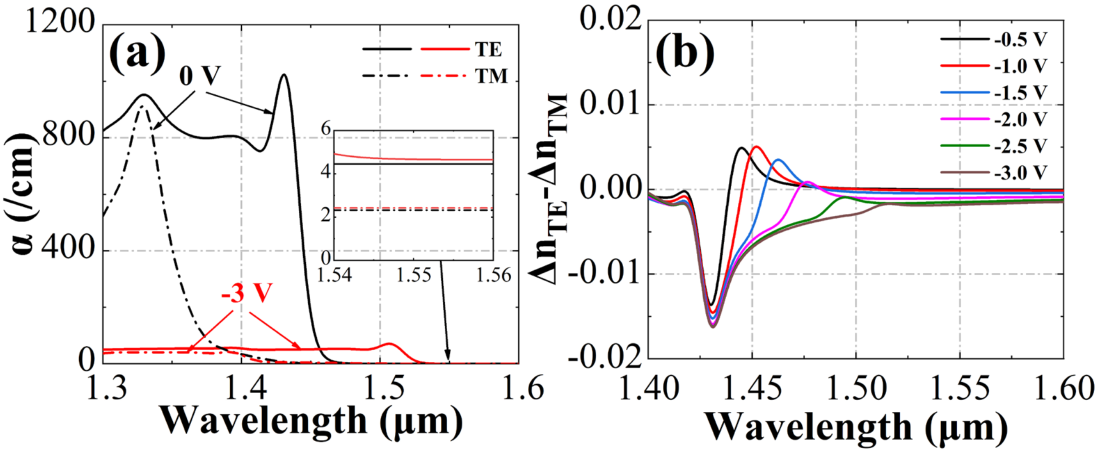

**Figure 6.4.1** (a) Calculated TE and TM absorption coefficient at $V_{DPS}$ =0 V and −3 V respectively, and (b) value of ($\Delta n_{TE}$ -$\Delta n_{TM}$) as a function of wavelength at different bias voltages for a DPS with a 100 nm blue-shift using QWI.

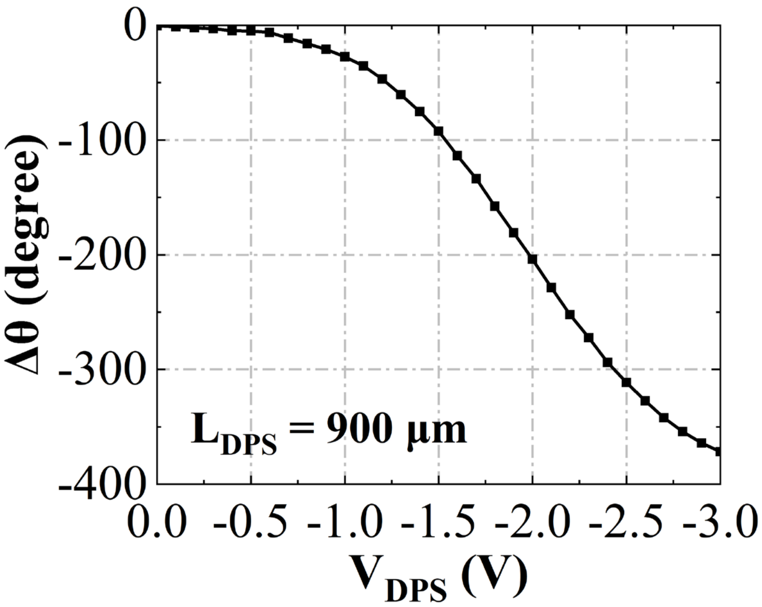

**Figure 6.4.2** Calculated phase shift angle $\Delta\theta$ for a 900 μm long DPS with a 100 nm blueshift by QWI at an operating wavelength of 1.55 μm.

# 6.5 Conclusion

we proposed and fabricated an SWG DFB laser monolithically integrated with PMC and DPS based on the identical epitaxial layer PIC scheme. For DFB-PMC-DPS devices, a rotation of nearly 60° in the *SV* on the surface of the Poincaré sphere was obtained over a range of bias voltage from 0 V to –3 V at $I_{DFB}$ =170 mA. A major advantage of the design is that only a single MOVPE step and two dry-etch steps are required to fabricate the device, significantly reducing complexity and cost. The demonstrated devices should be useful in realizing various types of polarization-multiplexed coherent transceivers.

# References of this chapter

[1] T. Tanemura and Y. Nakano, "Compact InP Stokes-vector modulator and receiver circuits for short-reach direct-detection optical links," *IEICE Transactions on Electronics,* vol. 101, no. 7, pp. 594-601, 2018.

[2] H. Deng, D. O. Yevick, C. Brooks, and P. E. Jessop, "Design Rules for Slanted-Angle Polarization Rotators," *Journal of Lightwave Technology,* vol. 23, no. 1, pp. 432-445, 2005.

[3] M. Renaud, M. Bachmann, and M. Erman, "Semiconductor optical space switches," *IEEE Journal of Selected Topics in Quantum Electronics,* vol. 2, no. 2, pp. 277-288, 1996.

[4] B. L. Weiss, Y. Chan, W. C. Shiu, and E. H. Li, "The electro-optic properties of interdiffused InGaAs/InP quantum well structures," *Journal of Applied Physics,* vol. 88, no. 6, pp. 3418-3425, 2000.

[5] M. Sugawara, T. Fujii, S. Yamazaki, and K. Nakajima, "Theoretical and experimental study of the optical-absorption spectrum of exciton resonance in In 0.53 Ga 0.47 As/InP quantum wells," *Physical Review B,* vol. 42, no. 15, p. 9587, 1990.

[6] J. Minch, S. Park, T. Keating, and S. Chuang, "Theory and experiment of In Ga As P and In Ga Al As long-wavelength strained quantum-well lasers," *IEEE J. Quantum Electron,* vol. 35, no. 5, pp. 771-782, 1999.

[7] X. Sun *et al.*, "Simulation of an AlGaInAs/InP Electro-Absorption Modulator Monolithically Integrated with Sidewall Grating Distributed Feedback Laser by Quantum Well Intermixing," *Photonics,* vol. 9, no. 8, p. 564, 2022.

[8] L. Hou, M. Haji, J. Akbar, J. H. Marsh, and A. C. Bryce, "AlGaInAs/InP monolithically integrated DFB laser array," *IEEE Journal of Quantum Electronics,* vol. 48, no. 2, pp. 137-143, 2011.

# Chapter 7 Eight-channel EML array as DWDM Source

## 7.1 Introduction

With the growth of the Internet, there is a continuous increase in demand for data capacity. One approach to enhancing data capacity in optical communication systems is to employ Wavelength Division Multiplexing (WDM), whereby multiple channels with distinct wavelengths are incorporated into a single fibre. WDM technology has been widely utilized in both short-reach interconnects [1], and long-haul optical communication systems [2]. A typical WDM link for telecoms is illustrated in Figure 7.1.1 [3]. In this setup, the optical transmitter generates multiple independent wavelengths using semiconductor lasers. Each wavelength is subsequently modulated by an electrical signal, and all wavelengths are combined using a wavelength multiplexer before being launched into a single-mode fiber. After transmission through the fiber, the wavelengths are demultiplexed via a wavelength demultiplexer and subsequently directed to individual receivers. WDM systems began with significant commercial deployments featuring 10 channels at 2.5 Gb/s [4]. In high-capacity dense wavelength division multiplexing (DWDM) systems, Total 60 channels at up to 400 Gb/s are supported in commercial DWDM systems, enabling a 1910-km point-to-point field trial system connecting of approximately 24 Tb/s [5]. In short-reach applications, the DWDM systems can support up to 400 Gb/s per channel, reaching a total capacity of approximately 63.2 Tb/s [6].

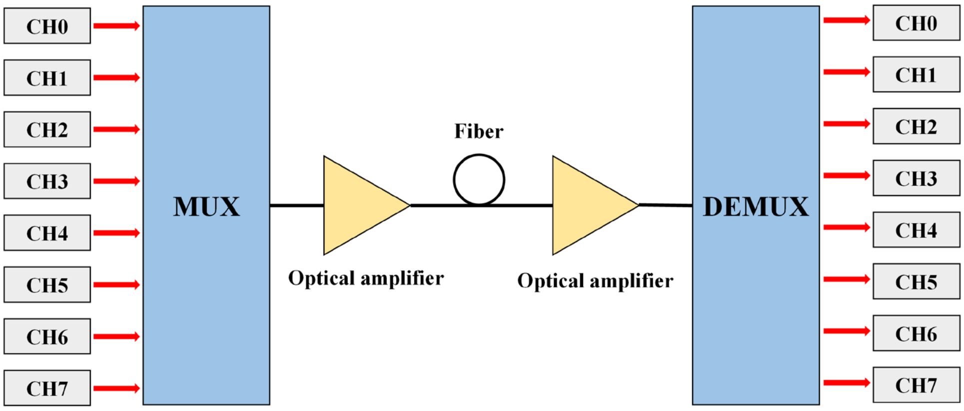

**Figure 7.1.1** An eight-channel WDM structure.

In addition, interest in multi-wavelength electroabsorption modulated light sources is increasing. A potential option for an optical transmitter is the electroabsorption-modulated laser (EML). An EML typically comprises of two primary components: a DFB laser section and an electro-absorption modulator (EAM). A schematic representation of this arrangement can be observed in Figure 7.1.2. The EML arrays have primarily found use in datacom-centric applications focused on digital transmission at high line rates through intensity modulation and direct detection (IM/DD), The impressive bandwidth of >90 GHz achieved by travelling-wave EAMs has allowed EMLs to offer high data rates exceeding 100 Gb/s over a single wavelength using simple modulation formats [7, 8]. Multi-level pulse amplitude modulation (PAM) represents an alternative approach that can reduce the demands on electro-optic bandwidth while simultaneously simplifying opto-electronic packaging requirements. It has been possible to attain data rates above 200 Gb/s/λ by leveraging signal equalization in the digital domain [9, 10]or through probabilistic shaping in conjunction with 8-level PAM [11]. Most of the reported electroabsorption modulated DFB laser (EML) arrays [12, 13] have been based on buried gratings, which lead to complex fabrication processes and high costs. Besides, the EML array channel spacings were 1.8 nm [12] or 2.5 nm [13], which cannot meet the DWDM standard spacing of 0.8 nm. Therefore, it is desirable to design monolithically integrated multi-wavelength EML arrays with a precise channel spacing at 0.8 nm and using simple fabrication processes. Reconstruction equivalent-chirp (REC) technology has made a significant contribution to precision wavelength control in laser arrays [14]. By dividing one sampling period into *m* equal sections (*m*≥2) with each adjacent grating period subjected to a 2π/m-phase shift, DFB diode lasers with a narrow lasing wavelength spacing (≤0.8 nm) can be realized with high precision control by changing only the sampling period.

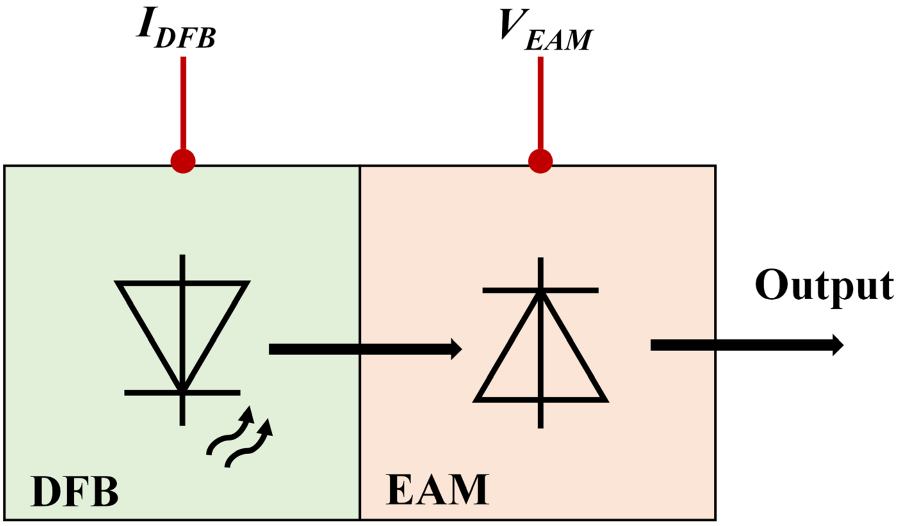

**Figure 7.1.2** An schematic of the EML.

In this work, a C-band eight-channel EML array with a channel spacing of 0.8 nm is presented based on a conventional 1550 nm AlGaInAs/InP multiple quantum well (MQW) laser diode (LD) epilayer structure using a four phase-shifted sampled Bragg grating (4PS-SBG) in the ridge sidewalls. The 4PS-SBG structure has a grating coupling coefficient, κ, 0.9× that of a uniform grating and so the DFB laser cavity length can be reduced to 400 μm. Sidewall grating DFB lasers need only one metalorganic vapor-phase epitaxy (MOVPE) step and one III-V material etch, simplifying the whole EML device fabrication process. The DFB lasers exhibit side mode suppression ratios (SMSRs) > 42 dB, and the integrated EAM achieves a 20 dB extinction ratio (ER).

# 7.2 Eight-channel EML array design and fabrication

## 7.2.1 Design of the EMLs array

The epitaxial layer is the same as the half-ridge PMC mentioned in Fig.7.2.1. The structure of a single EML is shown in Fig. 4.1.1 with an 800-µm-long 4PS-SBG DFB laser and a 100-µm-long EAM. The width of the ridge waveguide is set at 2.5 µm and there is a 30 µm electrical isolation gap between the DFB laser and EAM. The heights of the DFB laser and EAM ridge waveguides are 1.92 µm and 3.3 µm respectively. Fig. 7.2.1(b) shows an SEM picture of the 4PS-SBG sidewall gratings with a recess depth (*d*) of 0.6 µm on each side of the ridge. Each adjacent section has a π/2-phase-shift and there is a π-phase shift in the middle of the cavity to ensure single longitudinal mode (SLM) operation. The seed grading period is set at 257 nm corresponding to the 0th wavelength at 1630 nm. The sampling grating periods for CH1 to CH8 vary from 4.418 µm to 4.759 µm in steps of 48.7 nm to give a channel spacing of 0.8 nm around a lasing wavelength of 1550 nm. An optical microscope picture of the eight-channel monolithic EML array is shown in Fig. 7.2.1(c).

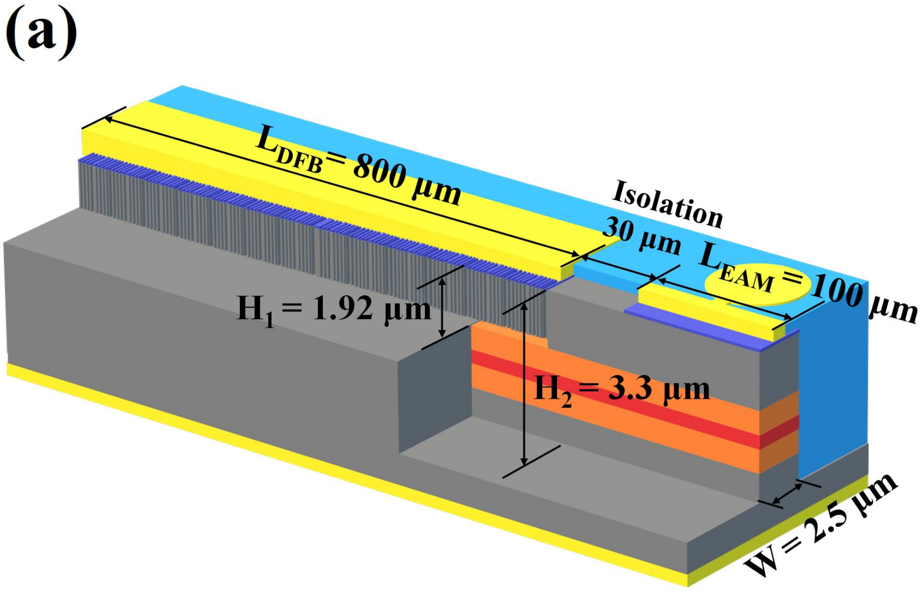

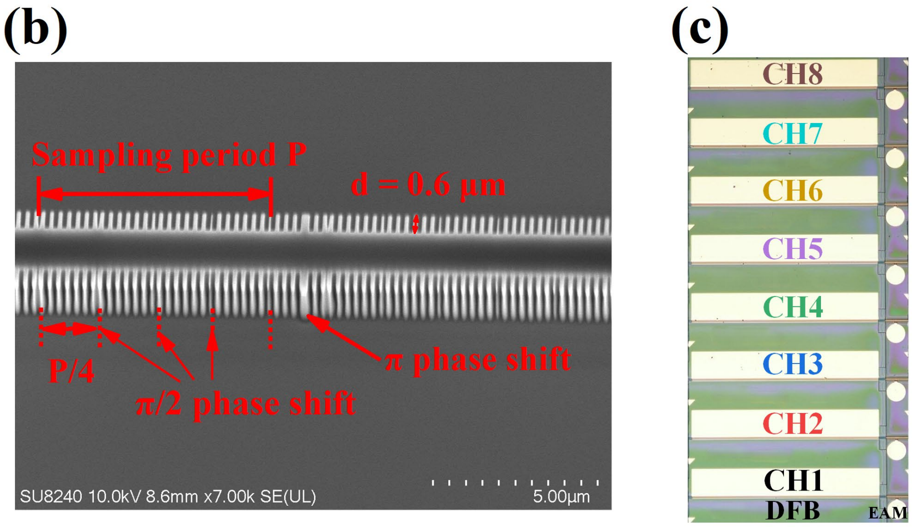

**Figure 7.2.1** (a) The schematic structure of a single EML, (b) SEM picture of the 4PS-SBG sidewall gratings, (c) optical microscope picture of the fabricated eight-channel EML array device.

## 7.2.2 Equivalent circuit model of EAM

To simulate the frequency response of the EAM with QWI, an equivalent circuit [15], shown in Fig. 7.2.2(a), was developed using ADS software. $L_o$ is the inductance of the connecting terminal microstrip, $R_o$ is the load resistance, $C_0$ is the capacitance of submount, and $R_s$ is the contact resistance which can be measured from the forward current-voltage curve. $R_j$ is the leakage resistance and $C_j$ is the junction capacitance. $C_p$ is the parasitic capacitance of the *p*-contact which can be reduced by passivation with hydrogen silsesquioxane (HSQ) [16]. The values of these parameters were measured from the vector network analyzer for as-grown EAM and are: $C_0 = 0.09$ pF, $R_j = 10$ kΩ, $C_j = 0.17$ pF, $R_s = 24$ Ω, $C_p = 0.14$ pF, $L_o = 0.4$ nH, and $R_o = 50$ Ω at $V_b = -1.6$ V. Although the measured result is for a non-QWI structure, the frequency response of a QWI device would be very similar because intermixing has little effect on the dielectric constant and the cut off frequency is not very dependent on the precise value of $R_j$. Figure 7.2.2(b) shows the value of $C_j$ and the −3-dB bandwidth as a function of $V_b$. It is found that with increasing bias voltage, $C_j$ is reduced because the space charge region easily penetrates the undoped layer due to the high doping (~$1\times10^{18}$ $\text{cm}^{-3}$) in the *P*- and *N*-cladding layers and the relatively thin undoped layer (210 nm), and $C_p$ is kept constant at 0.14 pF. So the total capacitance is decreased and the −3-dB bandwidth is increased. Figure 7.2.2(c) presents the simulated −3-dB bandwidth and maximum ER as a function of EAM length ($L_{EAM}$), with $V_b$ at –2.4 V and waveguide width ($W_{EAM}$) at 2.5 µm. It is obvious that when the EAM length is reduced, the –3-dB E/O response bandwidth will increase at the expense of maximum ER for relatively low reverse EAM voltages. Figure 7.2.2(d) presents the simulated electrical to optical (E/O) frequency response for the 150-µm-long EAM with $L_D$ = 0.45 nm and shows a −3-dB bandwidth of 22 GHz at $V_b$ = –1.6 V. This result is close to the measured −3-dB bandwidth of 19 GHz reported for an as-grown EAM [17]. It is also found that if the length of EAM is reduced to 70 µm and the ridge waveguide width is reduced from 2.5 µm to 2.0 µm, the –3-dB bandwidth will increase to 41 GHz due to the reduced junction capacitance. Of course, the DFB laser ridge waveguide width has to be reduced to 2 µm as well and the grating recess depth needs to be optimized to increase the grating coupling coefficient while maintaining stable transverse mode.

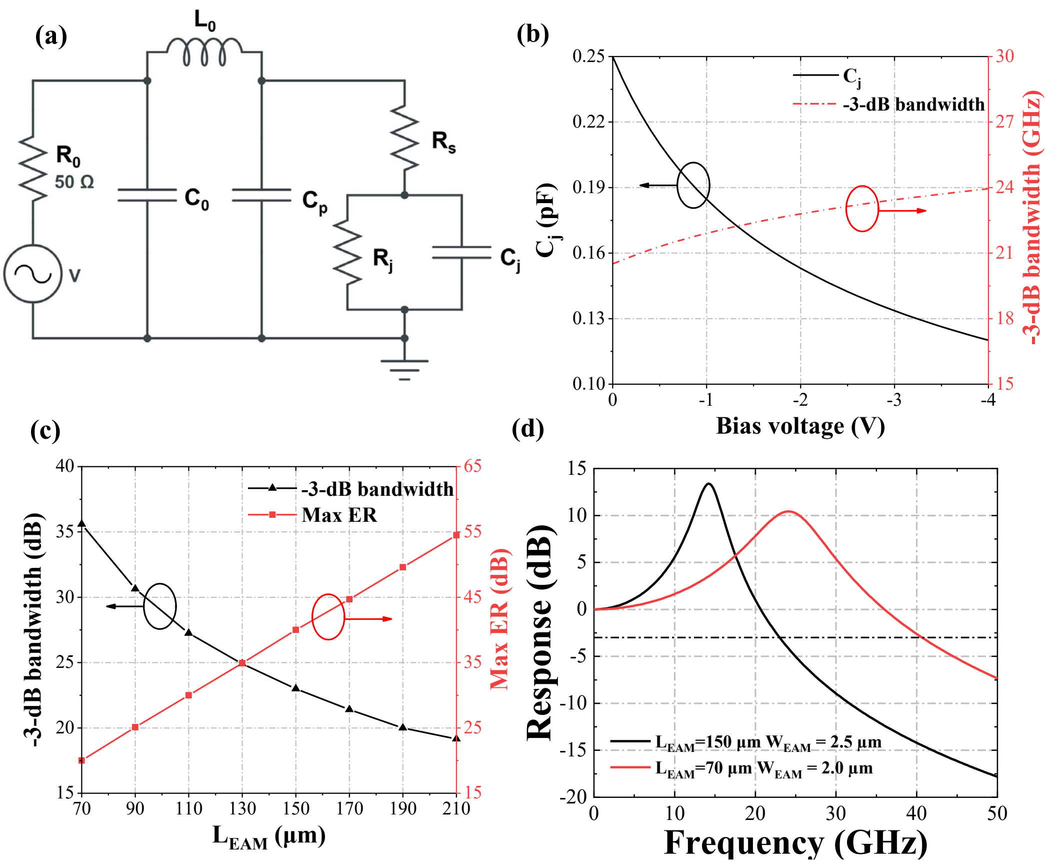

**Figure 7.2.2** (a) Equivalent circuit of the EAM; (b) $C_j$ and −3-dB bandwidth as a function of bias voltage ($V_b$) ; (c) −3-dB bandwidth and maximum ER as a function of EAM length ($L_{EAM}$) with $V_b$ = –2.4 V and $W_{EAM}$ = 2.5 µm; (d) simulated frequency response of 70 µm(red curve) and 150-µm-long(black curve) EAMs.

## 7.3 Eight-channel EML array measurement

Figure 7.3.1(a) shows the typical output power and voltage as a function of DFB current ($I_{DFB}$) for CH1. The bias voltage on the EAM ($V_{EAM}$) is set at 0 V. The threshold current of the DFB laser is 22 mA and the output power reaches 22 mW at $I_{DFB}$ = 220 mA. Fig. 7.3.1(b) shows the measured optical spectrum of the EML at threshold current; the stopband width is 1.06 nm, and $\kappa$ is calculated to be 14.2 /cm. A two-dimensional (2D) optical spectrum versus $I_{DFB}$ (0-180 mA) with $V_{EAM}$ = 0 V for CH1 is presented in Fig. 7.3.1(c), there is stable SLM operation from 36 mA to 180 mA. The average current-induced wavelength redshift coefficient is around 0.015 nm/mA.

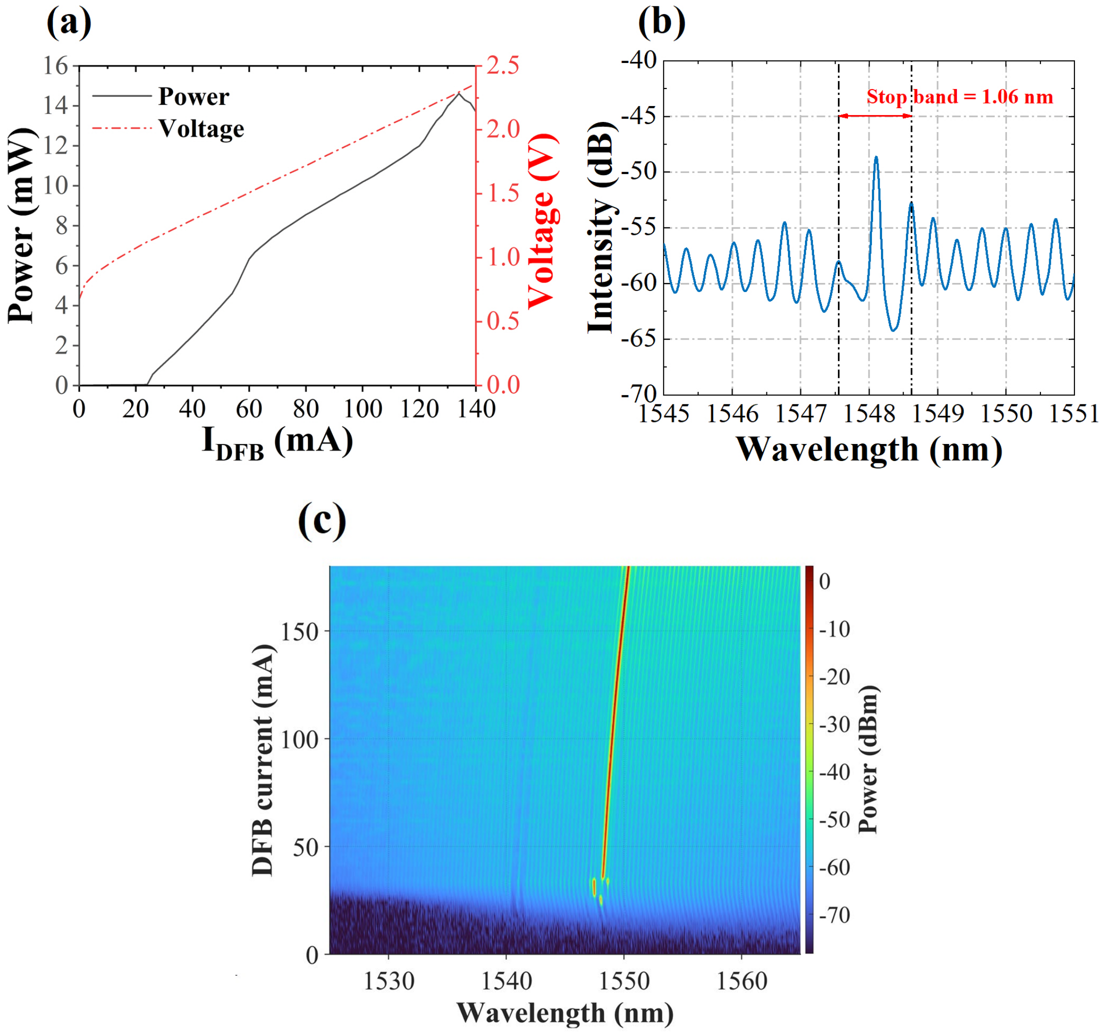

**Figure 7.3.1** (a) Typical $P$-$I_{DFB}$ curves under $V_{EAM}$ = 0 V, (b) Optical spectrum at threshold current of DFB laser, (c) 2D optical spectra vs $I_{DFB}$ of CH1.

Fig. 7.3.2(a) shows optical spectra for the eight channels with $I_{DFB}$ = 180 mA and

$V_{EAM} = 0$ V. The spectra were measured using an optical spectrum analyzer (OSA) with a resolution bandwidth of 0.06 nm. The emission wavelengths of the DFB lasers from CH1 to CH8 are 1548.32 nm, 1549.13 nm, 1549.93 nm, 1550.77 nm, 1551.42 nm, 1552.22 nm, 1553.02 nm, 1553.92 nm, and the SMSR >42 dB. Fig. 7.3.2(b) shows the corresponding linear fit to the lasing wavelengths of the eight channels, and the slope of the line is 0.787 nm with an error of 0.013 nm compared with the designed wavelength spacing of 0.8 nm. The value of this error is less than the resolution of the OSA, which demonstrates the excellent wavelength precision that can be achieved by the 4PS-SBG structure. The ERs as a function of the $V_{EAM}$ are shown in Fig. 7.3.2(c). The ER for each laser channel is around 20 dB with $V_{EAM} = -3.6$ V. The electrical-to-optical (E/O) response and dynamic performance are to be demonstrated in the near future. The simulated 3-dB modulation bandwidth of the deep etched 100-μm-long EAM is more than 30 GHz. Fig. 7.3.2(d) shows the optical linewidth of DFB lasers array using the delayed self-heterodyne method with a 4.4-km single-mode fibre and an 80-MHz acoustic-optic modulator. The smallest line can reach 50 kHz. Fig. 7.3.3 shows electrical-to-optical (E/O) response with $V_{EAM} = -2$ V. It is found that the 3-dB modulation bandwidth is about 17.4 GHz.

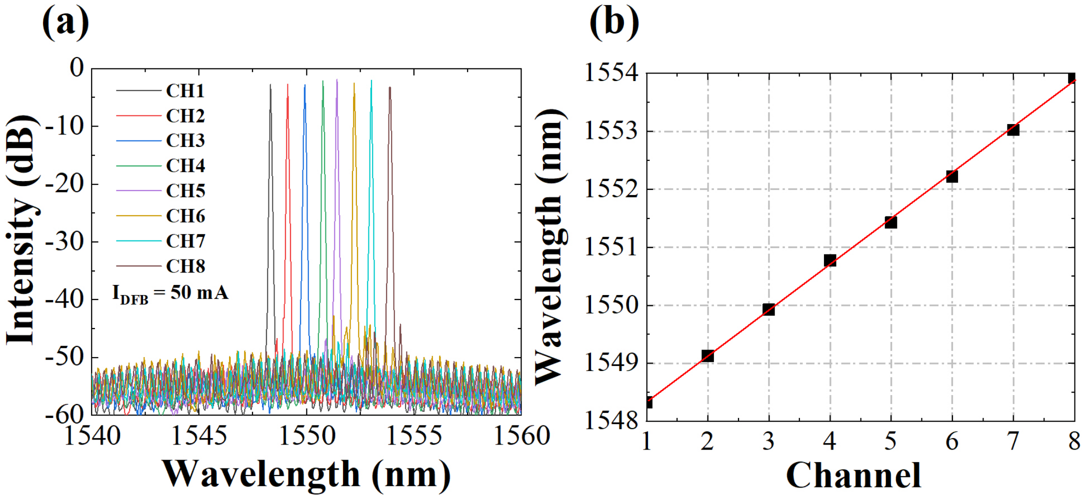

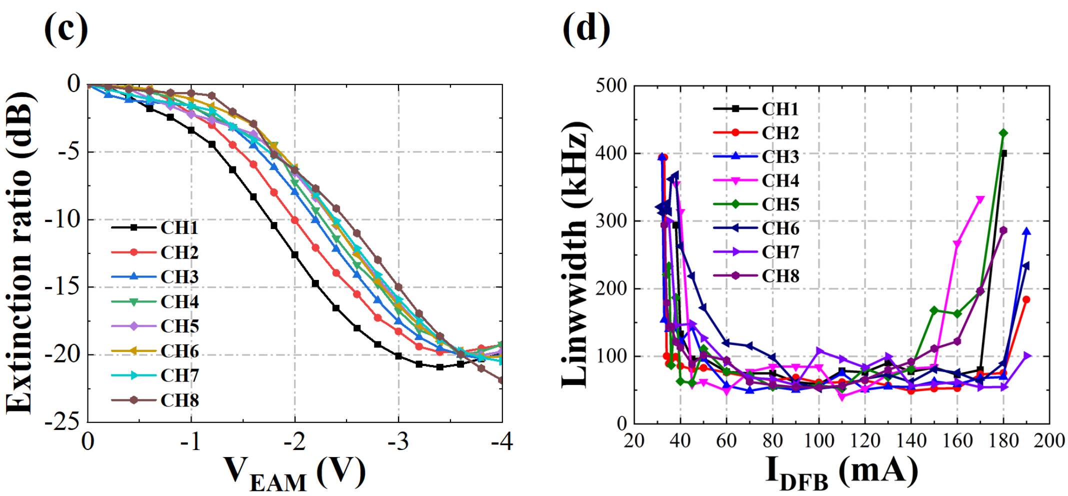

**Figure 7.3.2** (a) Measured optical spectrum of the 8-channel EML array when $I_{DFB}$ = 50 mA, $V_{EAM}$ = 0 V. (b) Lasing wavelengths and linear fitting of the eight EML devices. (c) Measured extinction ratios of the eight EMLs. (d) Measured optical linewidth of the 8-channel EML array.

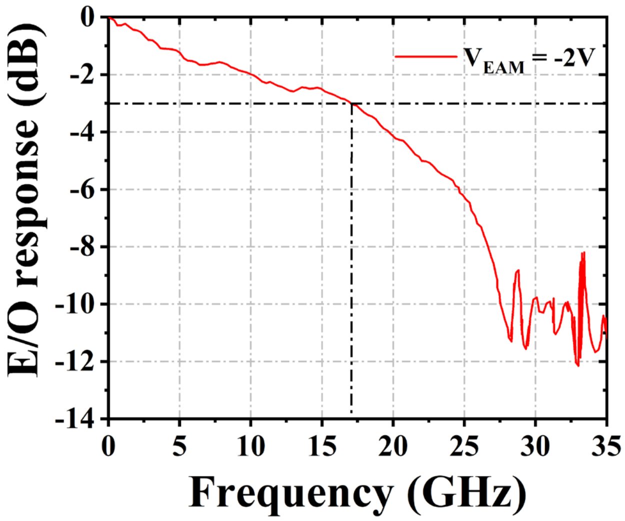

**Figure 7.3.3** Measured E/O response with $V_{EAM}$ = –2 V.

# 7.4 Conclusion

In conclusion, based on the 4PS-SBG structure, an eight-channel EML array with a 0.8 nm channel spacing is demonstrated experimentally. A maximum output power of 22 mW was obtained with stable SLM operation for $I_{DFB}$ from 36 mA to 180 mA. The average channel spacing is 0.787 nm and the SMSR of each laser is >42 dB. The *ER* of the EAM was found to be ~20 dB with $V_{EAM}$ = –3.6 V. The E/O response, i.e., the EML's 3-dB modulation bandwidth is measured at 17.4 GHz at $V_{EAM}$ = –2 V. This EML array is desirable for DWDM sources.

# References of this chapter

[1] G. L. Wojcik *et al.*, "A single comb laser source for short reach WDM interconnects," in *Novel In-Plane Semiconductor Lasers VIII*, 2009, vol. 7230, pp. 89-100: SPIE.

[2] A. J. Lowery, L. Du, and J. Armstrong, "Orthogonal frequency division multiplexing for adaptive dispersion compensation in long haul WDM systems," in *2006 Optical Fiber Communication Conference and the National Fiber Optic Engineers Conference*, 2006, pp. 1-3: IEEE.

[3] G. E. J. O. F. T. Keiser, "A review of WDM technology and applications," vol. 5, no. 1, pp. 3-39, 1999.

[4] K.-I. Suzuki, H. Masuda, S. Kawai, K. Aida, and K. J. E. L. Nakagawa, "Bidirectional 10-channel 2.5 Gbit/s WDM transmission over 250 km using 76 nm (1531–1607 nm) gain-band bidirectional erbium-doped fibre amplifiers," vol. 33, no. 23, pp. 1967-1968, 1997.

[5] A. Zhang *et al.*, "Field trial of 24-Tb/s (60× 400Gb/s) DWDM transmission over a 1910-km G. 654. E fiber link with 6-THz-bandwidth C-band EDFAs," vol. 29, no. 26, pp. 43811-43818, 2021.

[6] D. Le Gac *et al.*, "63.2 Tb/s Real-time transmission through discrete extended C-and L-band amplification in a 440km SMF Link," in *2021 European Conference on Optical Communication (ECOC)*, 2021, pp. 1-4: IEEE.

[7] O. Ozolins *et al.*, "100 GHz externally modulated laser for optical interconnects," vol. 35, no. 6, pp. 1174-1179, 2017.

[8] R. Lewén, S. Irmscher, U. Westergren, L. Thylén, and U. J. J. o. L. T. Eriksson, "Segmented transmission-line electroabsorption modulators," vol. 22, no. 1, p. 172, 2004.

[9] S. Kanazawa *et al.*, "214-Gb/s 4-PAM operation of flip-chip interconnection EADFB laser module," vol. 35, no. 3, pp. 418-422, 2017.

[10] X. Pang *et al.*, "200 Gbps/Lane IM/DD technologies for short reach optical interconnects," vol. 38, no. 2, pp. 492-503, 2020.

[11] J. Zhang *et al.*, "Demonstration of 260-Gb/s single-lane EML-based PS-PAM-8 IM/DD for datacenter interconnects," in *Optical Fiber Communication Conference*, 2019, p. W4I. 4: Optica Publishing Group.

[12] J. Xu, S. Liang, Z. Zhang, J. An, H. Zhu, and W. Wang, "EML Array fabricated by SAG technique monolithically integrated with a buried ridge AWG

multiplexer," *Optics & Laser Technology,* vol. 91, pp. 46-50, 2017.

[13] M. Theurer *et al.*, "4× 56 Gb/s high output power electroabsorption modulated laser array with up to 7 km fiber transmission in L-band," *Journal of Lightwave Technology,* vol. 36, no. 2, pp. 181-186, 2018.

[14] J. Li *et al.*, "A multiexposure technology for sampled Bragg gratings and its applications in dual-wavelength lasing generation and OCDMA en/decoding," *IEEE Photonics Technology Letters,* vol. 21, no. 21, pp. 1639-1641, 2009.

[15] H. Wang *et al.*, "Modeling and Experiment Verification of Lateral Current Spreading Effect in Ridge Waveguide Electroabsorption Modulators," *IEEE Transactions on Electron Devices,* vol. 62, no. 11, pp. 3756-3759, 2015.

[16] X. Sun, S. Ye, J. Seddon, C. C. Renaud, L. Hou, and J. H. Marsh, "Modeling and Measurement of a HSQ Passivated UTC-PD with a 68.9 GHz Bandwidth," in *2021 IEEE Photonics Conference (IPC)*, 2021, pp. 1-2: IEEE.

[17] A. Al-Moathin *et al.*, "EML Based on Identical Epitaxial Layer, Side-Wall Grating and HSQ Planarization," vol. 34, no. 6, pp. 317-320, 2022.

# Chapter 8 Conclusion and Future work

## 8.1 Conclusion

An SWG DFB laser monolithically integrated with a PMC, and an SWG DFB laser monolithically integrated with PMC and DPS based on the IEL PIC scheme have been successfully demonstrated. For the DFB-PMC devices, a TE/TM conversion efficiency of 98.4 % was obtained over a broad range of $I_{DFB}$ from 140 mA to 190 mA at a 1555 nm operating wavelength. The wavelength dependence was also calculated and measured; the devices have a PCE >90% over the wavelength range of 1543 nm to 1568 nm. For DFB-PMC-DPS devices, a rotation of nearly 60° in the SV on the surface of the Poincaré sphere was obtained over a range of bias voltage from 0 V to –3 V at $I_{DFB}$ =170 mA. A major advantage of the design is that only a single MOVPE step and two dry-etch steps are required to fabricate the device, significantly reducing complexity and cost. The demonstrated devices should be useful in realizing various types of polarization-multiplexed coherent transceivers. High-speed(>1GHz) polarization imaging is also desirable for material characterization(especially for biomedical studies and clinical applications) and dynamic observation of living cells and biological processes.

An eight-channel Electroabsorption Modulated Lasers (EML) array with a 0.8 nm channel spacing is theoretically optimized, fabricated and characterized. The integrated DFB section was realized based on the 4PS-SBG structure, and the electro-absorption modulator (EAM) section was based on IEL PIC techniques. The experiment resulted in a maximum output power of 22 mW, showcasing consistent Single-Longitudinal-Mode (SLM) operation for the Integrated Distributed Feedback (DFB) laser over a current range spanning from 36 mA to 180 mA. The average channel spacing measured

0.787 nm, with each laser achieving a Side Mode Suppression Ratio (SMSR) exceeding 42 dB. The Electro-Absorption Modulator (EAM) demonstrated an Extinction Ratio (ER) of approximately 20 dB at a voltage of $V_{EAM} = -3.6$ V. Furthermore, the Electro-Optical (E/O) response, as determined by the 3-dB modulation bandwidth of the Electroabsorption Modulated Laser (EML), reached 17.4 GHz under a voltage of $V_{\mathrm{EAM}} = -2$ V. This array of EML is exceptionally well-suited for Dense Wavelength Division Multiplexing (DWDM) transmitter sources.

# 8.2 Future work

In addition to the monolithic PMC and Electroabsorption Modulated Laser (EML) arrays introduced in this thesis, several other innovative InP-based devices have been proposed and are under investigation for potential future fabrication.

## 8.2.1 1D topological photonics crystal laser

Topological physics has been a focal point of fundamental research since the groundbreaking discovery of the quantum Hall effect. This pivotal revelation demonstrated that physical properties in the real world can remain stable even in the face of continuous changes in system parameters. While these remarkably robust phenomena have the potential to greatly improve the stability and performance of practical devices, their concrete applications have remained somewhat elusive.

A simple one-dimensional (1D) photonics crystal can be designed as an inherently encompass “grating like” elements. Figure 8.2.1 (a) shows a design of a 1D photonics crystal laser cavity. This is based on the line defect photonics crystal but there is a dislocation of the photonics crystal along the light propagating direction. Λ is the grating period and the photonics crystal period (distance between each hole) is Λ/2 and the dislocation length of the neighbor photonics crystal bar is Λ/4. $R$ is the radium of the crystal hole. Figure 8.2.1 (b) shows a fundamental mode for a 100 μm length grating structure in which $\Lambda = 240$ nm and $R = 72$ nm (0.3 Λ). It was found that there is one fundamental mode coupled at the center point of the stop band shown in Figure 8.2.1

(c). This is due to the reverse of the Zak phase at the center of the cavity. Figure 8.2.1 (d) presents the calculated Q factor of the fundamental mode, for 100 µm length grating structure Q factor is 3800 and by increasing the number of gating periods and using a finer simulation grid, a higher Q factor can be further obtained.

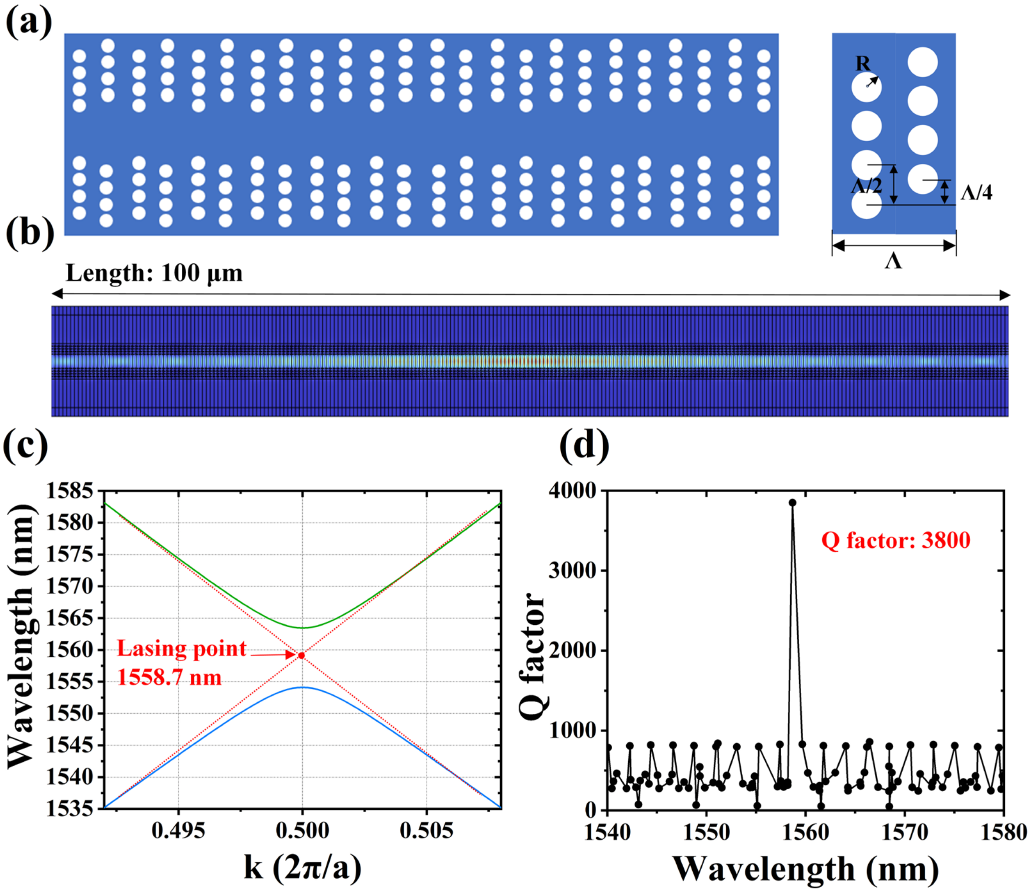

**Figure 8.2.1** (a) Design of the 1D topological photonics crystal laser cavity. (b) fundamental mode transmission for a 100 µm length grating. (c) band diagram of the 1D topological photonics crystal. (d) calculated Q factor of the 1D topological photonics crystal cavity.

Although this is a novel design, there is a challenge of the fabrication of the small feature photonic crystal on InP substrate with low cavity loss. Numerous dry etch tests have been conducted, as depicted in Figure 8.2.2. However, further optimization of the ICP dry etch recipe is required for future refinement.

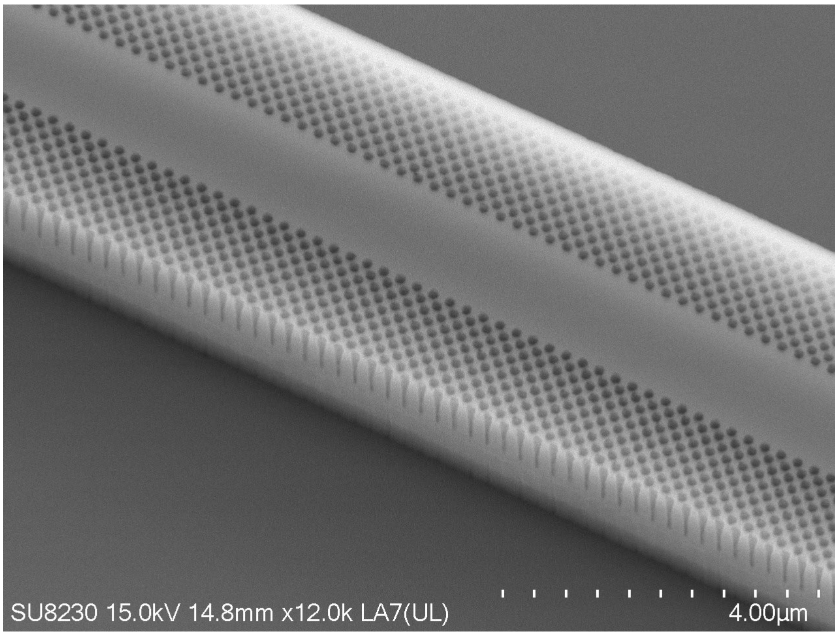

**Figure 8.2.2** ICP Dry etch test of the 1D topological photonics crystal laser cavity.

## 8.2.2 2D topological photonics crystal laser

The 2D topological photonic crystal represents a substantial advancement from its 1D counterpart, incorporating a second order grating to facilitate vertical emission. In Fig. 8.2.3(a), we present a schematic of our 2D topological photonic crystal laser. This configuration involves the placement of a 1.3Q photonic-crystal layer (320 nm) above a MQW layer (225 nm) on an InP substrate to form the topological cavity. The selection of the photonic crystal layer, characterized by a Dirac-vortex pattern, is deliberate, ensuring sufficient modal overlap (coupling strength) to obviate the need for etching the MQWs. This approach preserves the optimal material quality of the active region.

The Dirac-vortex pattern features a honeycomb air-hole lattice with a generalized Kekulé modulation within each supercell. This modulation encompasses parameters such as the radial distance '$R$', the correlated phase '$\varphi$', the distance between sub-lattices (three triangles denoted as '$d$'), and the side length of the triangle '$S_0$'. These intricately correlated variables are illustrated in Fig. 8.2.3(b) and 8.2.3(d). To create a 2π vortex bandgap, the supercell undergoes a continuous phase variation from 0 to 2π, arranged angularly around the center of the cavity. Fig. 8.2.3(c) shows the band diagram of the topological photonics crystal. There is a double degeneracy at the Dirac point. Fig.

8.2.3(d) shows the fundamental mode of a typical 2D topological photonic crystal laser with a = 561 nm, and the Q factor can reach to nearly 50000 shown in Fig. 8.2.3(d).

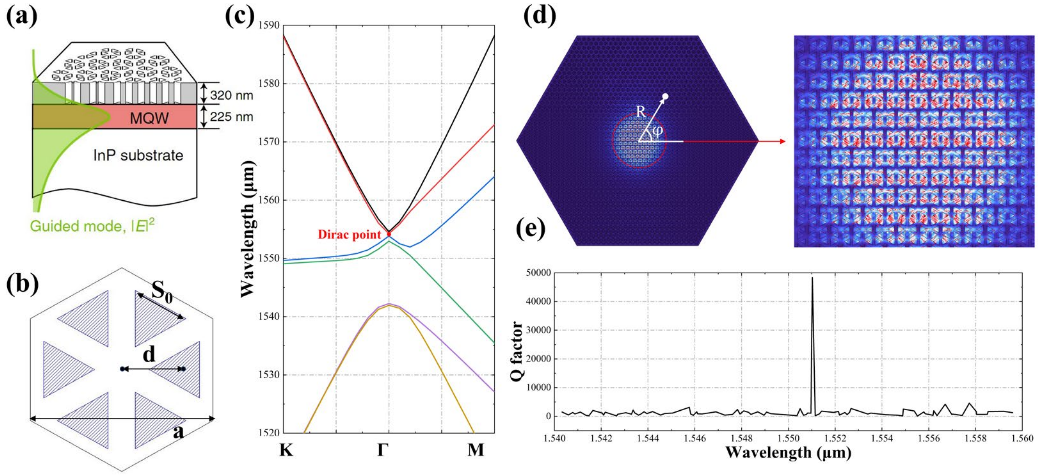

**Figure 8.2.3** (a) Design of the 2D topological photonics crystal laser cavity. (b) honeycomb air-hole lattice. (c) band diagram of the 2D topological photonics crystal. (d) fundamental mode of a typical 2D topological photonic crystal laser. (e) calculated Q factor of the 2D topological photonics crystal cavity.

While this design shows potential for application in creating a novel photonic crystal surface laser, it encounters similar fabrication challenges as the 1D topological photonic crystal laser. Figure 8.2.4 presents some results of the ICP dry etching process applied to the 2D topological photonic crystal, yet further refinement of the ICP dry etching recipe is necessary.

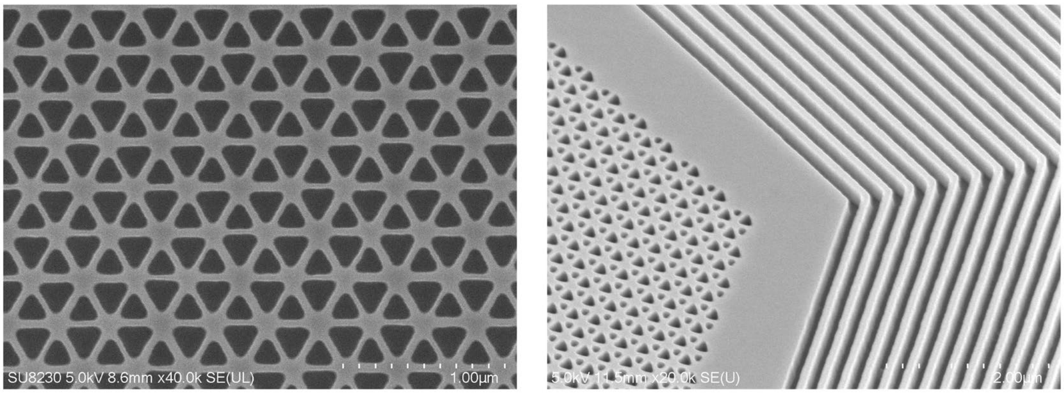

**Figure 8.2.4** ICP Dry etch test of the 2D topological photonics crystal laser cavity.